nature chemistry

Article

https://doi.org/10.1038/s41557-025-01916-7

Electrostatic atlas of non-covalent interactions built into metal–organic frameworks

Received: 3 October 2024

Accepted: 16 July 2025

Published online: 27 August 2025

Check for updates

Zhe Ji[1,5,7] ✉, Srijit Mukherjee[1,7], Jacopo Andreo[2], Anna Sinelshchikova[2], Francesca Peccati[3,4], Gonzalo Jiménez-Osés[3,4], Stefan Wuttke[2,6] ✉ & Steven G. Boxer[1] ✉

Non-covalent interactions are central to the organization of matter and molecular recognition processes, yet they are difficult to characterize. Here we devise a platform strategy to systematically build non-covalent interactions with selective chemical groups into precisely designed configurations by using metal–organic frameworks (MOFs) as the molecular scaffold. Using the vibrational Stark effect benchmarked against computer models, we find the electric field provides a unifying metric for quantifying diverse non-covalent interactions in MOFs and solvation environments. We synthesize and analyse spectroscopically a collection of non-covalent interactions using a nitrile probe within the MOF structure, and identify stabilizing fields as strong as −123 MV cm^{-1} produced additively by multiple hydrogen bonds, an unusual destabilizing field of +6 MV cm^{-1} between antiparallel dipoles, anomalous hydrogen-bond blueshifts as large as 34 cm^{-1} and unique solvation under nanoconfinement. This method for making and testing non-covalent interactions opens new avenues for exploring non-covalent interactions.

Non-covalent interactions are fundamental, ubiquitous forces that shape the properties and behaviours of molecules and their assemblies. These interactions can occur between any chemical groups that happen to get close enough, so there exists an enormous diversity of non-covalent interactions. While interactions such as hydrogen bonds (H bonds) are relatively strong and have well-defined and well-characterized properties, it is challenging to define most interactions, which are nonspecific and weak, even though their combination is often energetically substantial. Two primary experimental challenges must be overcome to assess individual non-covalent interactions: (1) how to systemically build individual non-covalent interactions between specific groups at precisely defined geometries without any direct covalent connection and (2) how to experimentally quantify these interactions from a physical perspective. We develop a general platform for placing selective chemical groups at defined positions and orientations using a metal–organic framework (MOF)[1–3], inspired by the molecular vise approach developed by Deng and co-workers[4–6]. In light of the fact that chemical groups that participate in non-covalent interactions can be mostly represented as charges and dipoles interacting with each other through their produced electric fields and the fact that electric fields oriented along reacting bond dipoles can reduce activation barriers and thereby promote chemical reactivity—an effect exemplified in enzyme electrostatic catalysis—we then measure the electric fields associated with our precisely designed non-covalent

[1]Department of Chemistry, Stanford University, Stanford, CA, USA. [2]Basque Center for Materials, Applications and Nanostructures (BCMaterials), Leioa, Spain. [3]Center for Cooperative Research in Biosciences (CIC bioGUNE), Basque Research and Technology Alliance (BRTA), Derio, Spain. [4]Ikerbasque, Basque Foundation for Science, Bilbao, Spain. [5]Present address: College of Chemistry and Molecular Engineering, Peking University, Beijing, China. [6]Present address: Academic Centre for Materials and Nanotechnology, AGH University of Krakow, Krakow, Poland. [7]These authors contributed equally: Zhe Ji, Srijit Mukherjee. ✉e-mail: jizhe@pku.edu.cn; swuttke@agh.edu.pl; sboxer@stanford.edu

https://doi.org/10.1038/s41557-025-01916-7

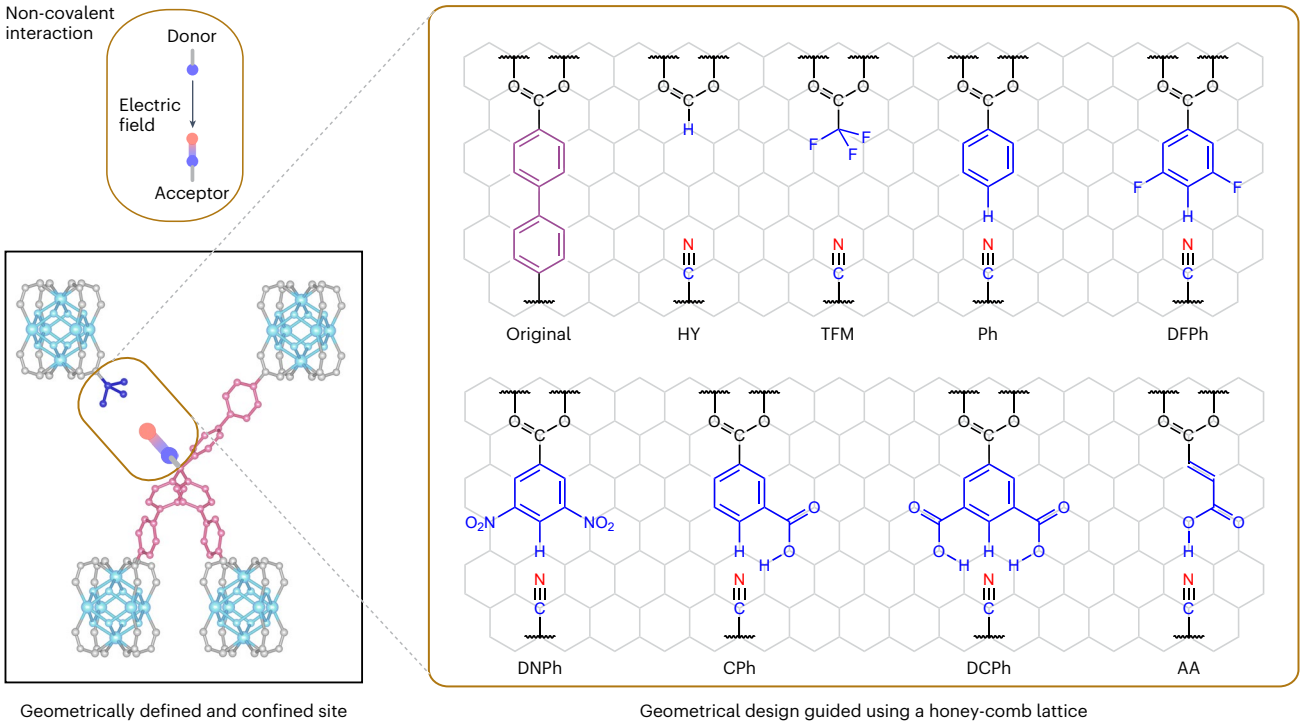

Fig. 1 | Electrostatic picture of non-covalent interactions and the molecular platform developed in this work. To study the electric fields produced by non-covalent interactions, we anchored a nitrile probe (field acceptor) against a series of field donors in a geometrically defined and confined site in a MOF. The field donor can be systematically varied by geometrical design, guided and visualized using a honey-comb lattice, resulting in an array of non-covalent interactions to be probed.

interactions using the vibrational Stark effect (VSE)[7–11] and characterize the electrostatic contribution to these interactions. Here, we refer to the chemical group that produces the electric field of interest as the electric field donor and the group that experiences the field as the acceptor, a nomenclature inspired by the commonly used H-bond donor/acceptor and here applied to non-covalent interactions in general.

Previous studies used vibrational probes to report the electric fields associated with diverse chemical environments including proteins[10–23], lipid membranes[24,25], solvation shells[11,26,27] and electrode-electrolyte interfaces[28,29]. Although these results have provided insights into specific interactions, especially those related to a substantial contribution of electrostatic pre-organization to the proficiency of enzymes, the chemical scope is limited because in solution and at interfaces the positioning of donor and acceptor typically cannot be controlled, and in biomolecules the range of electric field donors is largely constrained by bio-specificity evolved from nature. We overcome these limitations by using a rigid scaffold onto which an electric field probe (nitrile) is anchored in apposition to a series of field donors (Fig. 1). Specifically, a MOF is used to act as the structural backbone to hold the electric field donors and a nitrile acceptor as a probe in place. The permanent porosity of the MOF allows for the removal of solvent and isolation of the interrogated non-covalent interaction. Re-addition of solvent within this framework also provides a unique opportunity to examine solvation under nanoconfinement.

We chose a nitrile as the field probe because its vibrational frequencies lie in a part of the vibrational spectrum that is distinctly separate from background absorption and nitriles have been extensively studied for probing electric fields[12–17]. Using a calibration based on vibrational solvatochromism, perturbations to the nitrile vibrational frequency within the MOF scaffold in response to different apposing functionalities can be used to extract the electrostatic contribution to the interactions. The experimental results are then compared with computer simulations to interrogate and benchmark non-covalent interactions involving H bonds and the solvation effect under MOF nanoconfinement.

Results and discussion

Design and synthesis of MOFs holding field donor–acceptor pairs

We chose PCN-521 (ref. 30) as the MOF scaffold for positioning field donor–acceptor pairs (Fig. 2), the same MOF that Deng and co-workers developed for the molecular vise approach[4–6] owing to the ease of functionalization and the right size of the functionalization site. Single octahedral PCN-521 crystals (Supplementary Fig. 1) were synthesized by connecting $Zr_6O_4(OH)_4$ clusters (Fig. 2a, blue) with a tetrahedral organic linker, 4′,4″,4‴,4⁗-methanetetrayltetrabiphenyl-4-carboxylic acid (H_4L; Fig. 2a, green), into an extended network in a fluorite topology (Fig. 2b). The solvent inside the MOF pore was exchanged and removed by evacuation without structural collapse. The crystallinity and the composition were confirmed by powder X-ray diffraction (PXRD) (Supplementary Fig. 2) and digestion NMR spectroscopy (Supplementary Fig. 3), respectively.

To install a vibrational probe into the structure of PCN-521, we designed and synthesized a trigonal pyramidal organic linker, tris(4-carboxylbiphenyl)acetonitrile (H_3LCN; Fig. 2a, magenta, and Supplementary Figs. 4–11), which maintains three of the carboxylate groups in H_4L and bears a nitrile probe in the fourth position, facing into the pore. The incorporation of H_3LCN does not compromise the overall crystallinity of PCN-521, as evidenced by the unchanged PXRD pattern (Supplementary Fig. 12). We found that a 2:1 molar ratio of H_4L to H_3LCN in the reaction mixture led to a 4:1 molar ratio of H_4L to H_3LCN in the obtained PCN-521 crystals, as measured by digestion NMR spectroscopy (Supplementary Fig. 13 and Supplementary Table 1). The structural consequence of the linker substitution is that a fraction of the tetrahedral sites now has one biphenylene ligand replaced by a defined defect (Fig. 2b). On the opposite side, appended from the

https://doi.org/10.1038/s41557-025-01916-7

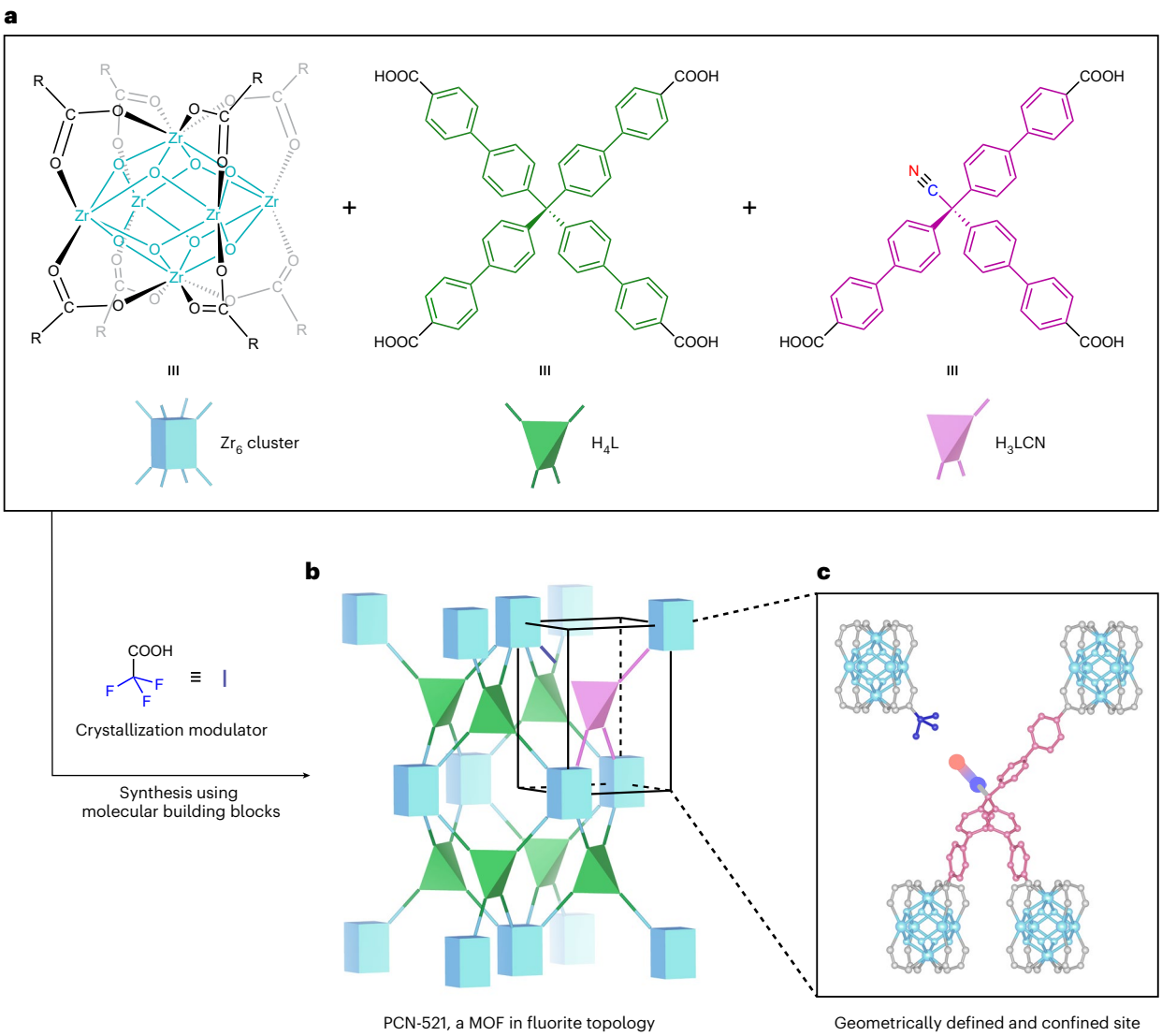

Fig. 2 | PCN-521, a MOF, acts as a molecular scaffold onto which field donors and acceptors are installed in fixed configurations. a, Molecular building blocks of the MOF. **b**, Connection of the metal cuboid (Zr_6 cluster) and the organic tetrahedron (H_4L) into a network in fluorite topology. **c**, Incorporation of the trigonal organic linker (H_3LCN) builds into the MOF crystals defective sites comprising a field donor ($-CF_3$) oriented towards a field acceptor (nitrile probe).

underconnected Zr cluster is the trifluoracetic acid modulator added in the reaction mixture, so the PCN-521 structure has abundant defect sites that comprise the $-CF_3$ group aligned towards the nitrile (Fig. 2c). After washing and evacuation, the intentionally created defect sites are free of solvent, hosting a specific non-covalent interaction between $-CF_3$ and the nitrile in isolation.

The molecular and modular nature of the MOF structure allows us to systematically replace the trifluoroacetic acid with a range of other carboxylate ligands (Fig. 1). The MOF crystals were soaked in methanol solutions of different carboxylic acids. The new carboxylic acid spontaneously substituted trifluoracetic acid, yielding a series of MOF variants we refer to as HY (a structure containing a hydrogen atom as the field donor), TFM (as synthesized, a trifluoromethyl donor), Ph (a phenyl donor), DFPh (a difluorophenyl donor), DNPh (a dinitrophenyl donor), CPh (a carboxylate phenyl donor), DCPh (a dicarboxylate phenyl donor) and AA (an acrylic acid donor), each bearing a unique field donor as shown in Fig. 1. The field donors were found to occupy 60–80% of the total open coordination sites as quantified by digestion NMR spectra (Supplementary Figs. 14–20 and Supplementary Table 1). Crystallinity of these MOF variants were confirmed by PXRD (Supplementary Fig. 12).

Electrostatic characterization of aprotic interactions via the vibrational Stark effect

Previous work has established that nitrile vibrational probes exhibit a linear vibrational Stark effect, vibrational frequency shifts in proportion to the magnitude of electric field, in aprotic environments[7–15] (Supplementary Texts 1–3). This does not extend to nitrile frequencies in protic (H-bonding) environments due to well-known anomalous blueshifts in frequency (Supplementary Text 4). Infrared absorption transition dipole moments of nitriles have been shown to exhibit linearity with the field in all environments[16]; however, this requires precise information on the absolute concentration of the nitrile, which is not applicable to the MOF powder samples studied here (Supplementary Text 4). Therefore, in this work we focus on using Raman scattering of bulk MOF samples to measure the vibrational frequency of nitrile to infer the magnitude of electric fields (note that intensity quantification under polarization is precluded by the strong birefringence exhibited by PCN-521 crystals; Supplementary Figs. 21 and 22 and Supplementary Text 5). The same measurement can be performed on any single-crystalline or polycrystalline sample that harbours specific interactions.

To calibrate the sensitivity of the nitrile's frequency shifts to electric fields (the Stark tuning rate, $\Delta\vec{\mu}$), we used triphenylacetonitrile

https://doi.org/10.1038/s41557-025-01916-7

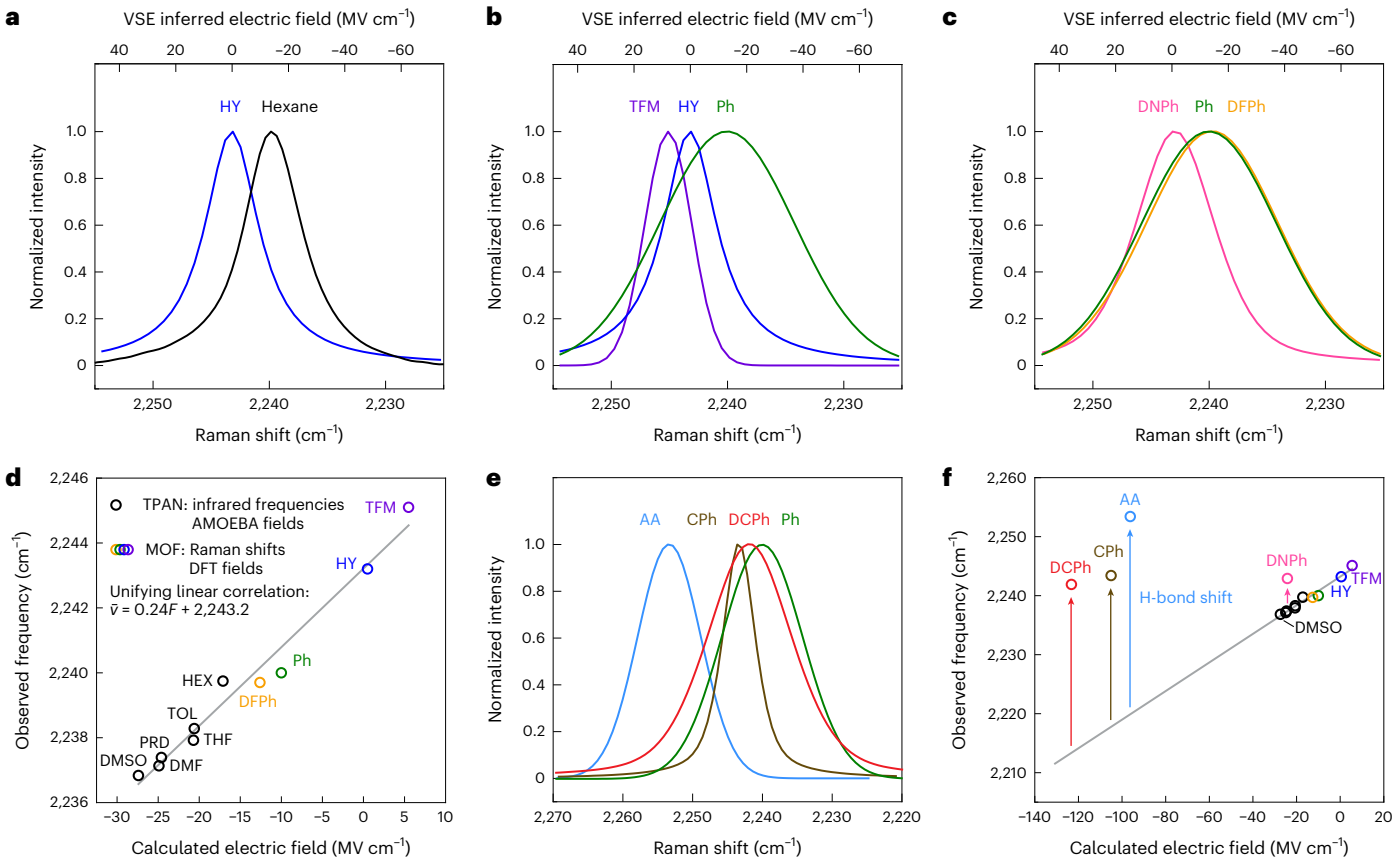

Fig. 3 | Raman spectroscopy and electric field calculation for the MOF structures. a, Fitted Raman spectrum for HY overlaid with the infrared spectrum of the TPAN model compound in hexanes (raw spectra shown in Supplementary Fig. 30 and fitting results listed in Supplementary Table 7). The top axis of the VSE inferred electric field derives from the linear correlation shown in **d**. **b**, Fitted Raman spectra for the HY, TFM and Ph variants. **c**, Fitted Raman spectra for the Ph, DFPh and DNPh variants. **d**, Field-frequency correlation plotted using (1) MOF variant data (coloured circles) with experimentally measured Raman shifts and DFT-calculated electric fields and (2) TPAN solvatochromic data (black circles) with experimentally measured infrared frequencies and AMOEBA-derived electric fields. DMF, *N*,*N*′-dimethylformamide; DMSO, dimethylsulfoxide; HEX, hexanes; PRD, pyridine; THF, tetrahydrofuran; TOL, toluene. The linear fitting combining the MOF variant data and the TPAN solvatochromic data gives $\bar{\nu} = 0.24F + 2243.2$, with $r^2 = 0.97$, where $\bar{\nu}$ is the wavenumber (cm^{-1}) of the C≡N vibration and F is the magnitude of electric fields (MV cm^{-1}) projected on the C≡N bond axis. The same equation is used to generate the inferred electric field axes on top of the graphics in **a**–**c**. **e**, Fitted Raman spectra for the Ph, CPh, DCPh and AA variants. **f**, Addition of observed Raman shifts and DFT-calculated fields for CPh, DCPh and AA onto the linear VSE plot from aprotic solvents and non-H-bond donors shown in **d** (note the expanded horizontal axis). The vertical deviations from the VSE line are attributed to the H-bond blueshifts.

(TPAN) rather than the less soluble H_3LCN as the model compound for measuring vibrational solvatochromism in aprotic solvents of varying polarity (Supplementary Text 6). The frequency shifts of TPAN in response to solvent polarity were plotted against the solvent electric field magnitudes calculated by molecular dynamics simulations using fixed-charge (GAFF) and polarizable (AMOEBA) force fields (Supplementary Figs. 23–27 and Supplementary Tables 2–4). Compared with fixed-charge force fields, AMOEBA polarizable force fields, which incorporate molecular polarizability, consistently led to solvent electric fields with larger magnitudes, providing a $|\Delta\vec{\mu}|$ of 0.28 cm^{-1}/(MV cm^{-1}). This value is in close agreement with density functional theory (DFT)-based in silico Stark calculations (Supplementary Figs. 28and 29) where a uniform field was applied along the direction of the nitrile in TPAN. These results, together with recent study on nitrile-probed electric fields in photoactive yellow proteins (PYP)[16,17,31], reinforce that polarizability is an indispensable parameter for field estimations of nitriles.

To confirm that TPAN is a valid model compound whose nitrile has similar Stark behaviour as the nitrile probe installed in the MOF using H_3LCN, we applied the geometrical constraints to TPAN that the MOF backbone exerts on the H_4L linker according to the PCN-521 crystal structure (CCDC: DITJOH)[30] (Supplementary Fig. 28) and performed DFT calculations. We found from the in silico Stark calculations that the constraints only slightly change $|\Delta\vec{\mu}|$ (Supplementary Fig. 29). The consistent $|\Delta\vec{\mu}|$ between TPAN and H_3LCN observed from solvatochromism (Supplementary Fig. 23 and Supplementary Tables 5 and 6) corroborates the validity of using TPAN as the model compound. These results confirm the transferability of using the calibration curve obtained from TPAN solutions to infer the magnitude of electric fields inside the MOF (the value of $|\Delta\vec{\mu}|$ was updated later, merging the MOF data with TPAN data into a unifying calibration; Fig. 3).

After calibrating the nitrile probe, we measured the Raman spectra of the MOF variants and found diverse vibrational frequencies for the nitrile (Fig. 3, Supplementary Fig. 30 and Supplementary Table 7). HY, the variant with the simplest and most distant field donor, presents a nitrile frequency of 2,243.2 cm^{-1} (Fig. 3a), essentially the gas-phase frequency, corresponding to an electric field close to zero (0.5 MV cm^{-1}) in the evacuated porous structure. In comparison, hexane, a very non-polar solvent, produces an electric field of −17.1 MV cm^{-1} (polarizable force fields) for the TPAN nitrile (2,239.7 cm^{-1}) (Fig. 3a). To understand the origin of the close-to-zero field in HY, we applied harsh evacuation conditions to induce structural collapse and loss of crystallinity and observed that the nitrile peak broadens and red shifts by 3.4 cm^{-1} (Supplementary Fig. 31), confirming that the MOF porosity is essential

for creating the gas-phase condition for the nitrile. This observation was also noted for the isostructural, Hf-substituted MOF PCN-523 (Supplementary Figs. 32–34). The TFM variant, where the $-CF_3$ group aligns its dipole antiparallel to that of the nitrile, displays a bluer nitrile vibration observed at 2,245.1 cm^{-1}, the first observation of a nitrile in a destabilizing environment (Fig. 3b). The Ph variant—where the stabilizing –Ph field donor is located close to the nitrile—displayed a redshift to 2,240.0 cm^{-1}. With two –F groups added to the –Ph group, the DFPh variant displayed vibrational frequency of 2,239.7 cm^{-1} (Fig. 3c), a small redshift manifesting a weak inductive effect of the –F substituents and a slightly more stabilizing environment for the nitrile.

To understand the observed vibrational shifts, we conducted DFT geometry optimization of the MOF structures using the native PCN-521 crystal structure[30] (CCDC: DITJOH) as the starting model. We then incorporated H_3LCN and the field donors into the structure and located the minima of the potential energy surface. In HY, the installed field donor –H is measured to be 6.23 Å from the N atom in the nitrile based on DFT-optimized structures (Supplementary Fig. 35 and Supplementary Tables 8 and 9), positioning it beyond a range conducive for meaningful H-bond interactions with the nitrile. In Ph and DFPh variants, the *para* H in the –Ph moiety is closer to the N atom in the nitrile (2.45 Å and 2.29 Å, respectively). From these geometries, we generated electrostatic potential (ESP) maps for the interactions between the field donors and the nitrile to estimate the fields (Supplementary Fig. 36). The field calculations from ESP show that the –H in HY produces a negligible field of 0.5 MV cm^{-1} on the nitrile, while the –Ph and –3,5-difluoroPh produces a stabilizing field of –10 MV cm^{-1} and –12.6 MV cm^{-1}, respectively (Supplementary Table 10). The electric field exerted by the $-CF_3$ group is confirmed to be destabilizing and calculated to be +5.5 MV cm^{-1}. In Fig. 3d, we plot the electric field magnitudes of these interactions against the nitrile vibrational frequencies from the Raman measurements.

Overlaying the MOF data points (Raman shifts, DFT-calculated electric fields) with TPAN solvatochromism data points (infrared frequencies, AMOEBA-derived electric fields) reveals a unifying linear correlation with a $|\Delta\vec{\nu}|$ of 0.24 cm^{-1}/(MV cm^{-1}) and an intercept at 2,243.2 cm^{-1}. The good linearity ($r^2 = 0.97$) indicates that the averaged electric fields produced by bulk solvents and the oriented electric fields exerted by chemical groups installed in the MOF have the same physical foundation, manifesting the power of electric field, a unifying metric for quantifying diverse non-covalent interactions in MOFs and solutions (and proteins) with a common unit. Using the MOF as a platform, we built very low-field chemical environments (HY) approaching that in the gas phase and an unusual destabilizing environment (TFM) for the nitrile, systems unattainable by solvation or protein environments. The unifying linear correlation shown in Fig. 3d also showcases that classical polarizable force fields that use an extensive electrostatic description and quantum mechanically calculated ESP, two different computational methods, now converge into a precise prediction of electric fields. Using the new calibration curve, we add a top axis to Fig. 3a–c to map the readout of the observed nitrile vibrational frequency shifts to the magnitude of electric fields inside the different MOFs.

Anomalous blueshift in frequency due to H bonds formed by protic field donors

With the robust VSE established for aprotic environments, we set out to build and interrogate systems involving H bonds to the nitrile. We installed field donors bearing protic moieties, CPh, DCPh and AA, displaying vibrational frequencies of 2,243.4 cm^{-1}, 2,241.9 cm^{-1} and 2,253.4 cm^{-1}, respectively (Fig. 3e). DFT-based geometry optimization of these structures reveals conformational heterogeneity owing to single-bond rotations within these donors; however, most conformers contain direct H bonds to the nitrile with rather short heavy atom distances (<3 Å) and near head-on angles (>140°) (Supplementary Fig. 35 and Supplementary Tables 9 and 10). The Boltzmann-averaged ESP fields for CPh, DCPh and AA are calculated as –105.0, –123.2 and –96.2 MV cm^{-1} (Supplementary Table 10)—fields of magnitudes that are typically encountered in enzyme active sites and important for catalysis (from –70 MV cm^{-1} to –170 MV cm^{-1})[10,22,23]. In Fig. 3f we add the observed Raman frequencies and calculated fields for CPh, DCPh and AA onto the linear VSE plot from aprotic solvents and non-H-bond donors (Fig. 3d). We attribute the striking deviation from the VSE line to the H-bond blueshifts ($\Delta\bar{\nu}_{HB}$), which are 25.6, 28.6 and 33.5 cm^{-1} for CPh, DCPh and AA, respectively (Supplementary Tables 10 and 11). The $\Delta\bar{\nu}_{HB}$ in these MOF variants are consistent with predictions from a recent model developed by Kirsh and Kozuch that works on geometric descriptors of electrostatic interactions, with validation through theoretical and experimental data of nitriles embedded in PYP[16,17]. The vibrational Stark effect based on infrared intensities, high-resolution crystal structures and advanced molecular dynamics simulations allow for accurate predictions of $\Delta\bar{\nu}_{HB}$ based on H-bond distances (for example, N–O in C≡N···H–O) and H-bond angles (for example, C–N–O in C≡N···H–O) (Supplementary Text 4)[17]. When extrapolated to our MOF variants, where we build H bonds that are shorter and more head-on than those observed in the high-resolution structures of nitrile-substituted PYPs, we observe $\Delta\bar{\nu}_{HB}$ larger than protein variants. Thus, the MOF system acts as an excellent experimental platform for building and probing short and head-on H bonds.

We further sought to test whether a weak H bond can be built into the MOF by using –3,5-dinitrophenyl moiety as the field donor. It has a slightly acidic C–H group due to the strong electron-withdrawing nitro substituents, and the DNPh variant exhibits a vibrational frequency of 2,242.0 MV cm^{-1} (Fig. 3c). We calculated the ESP field for DNPh as –24.2 MV cm^{-1}, resulting in a $\Delta\bar{\nu}_{HB}$ of 5.6 cm^{-1} (Supplementary Table 11), lying at the smallest end of the $\Delta\bar{\nu}_{HB}$ spectrum, consistent with chemical intuition.

Unique solvation under nanoconfinement

We extended the use of the MOF platform to examine unique solvation environments confined in the MOF pore. The nitrile probe is located at the shared window between three octahedral cavities, each of which, with a size of 20.5 × 20.5 × 37.4 Å (ref. 30), can potentially be filled with ~10^2 DMSO molecules. After evacuation, we soaked nitrile-containing MOF crystals in DMSO and measured their Raman spectra. DMSO was selected due to its low vapour pressure and high boiling point, which reduced solvent evaporation during Raman measurements. Upon DMSO solvation, the nitrile in HY showed a redshift by 2.9 cm^{-1} with respect to the solvent-free HY (Fig. 4a), corresponding to a more stabilizing electric field by –12.0 MV cm^{-1} (Supplementary Table 12). Given that the nitrile of TPAN (or H_3LCN) in bulk DMSO experiences an averaged field of –27.4 MV cm^{-1}, the DMSO filled in the MOF pore constitutes a unique solvation environment that produces less than half of the electric field that bulk DMSO does. The solvation environment was also found to be field-donor dependent. The TFM variant displays a redshift by 5.7 cm^{-1} after DMSO solvation, corresponding to an electric field change of –23.5 MV cm^{-1} (Fig. 4b), while the Ph variant exhibits a redshift by only –1.3 cm^{-1}, corresponding to an electric field change of –5.4 MV cm^{-1} (Fig. 4c). This minimal stabilization can be explained by the bulky –Ph group near the nitrile, leaving little space for the solvent to form an effective solvation sphere.

To investigate how solvation perturbs H bonds, we soaked the AA variant in DMSO and observed a dramatic redshift of the nitrile frequency by 14.3 cm^{-1} (Fig. 4d), indicating disappearance of the large H-bond blueshift (33.5 cm^{-1}) characteristic of AA. Assuming no H bond remains, the vibration shift of DMSO-soaked AA can be treated using the purely electrostatic model, resulting in a more destabilizing electric field by 79.2 MV cm^{-1}, a big loss of the stabilizing field due to removal of the strong H bond. The electrostatic effect of solvation in the MOF variants are summarized in Fig. 4e. In addition to the above analysis

https://doi.org/10.1038/s41557-025-01916-7

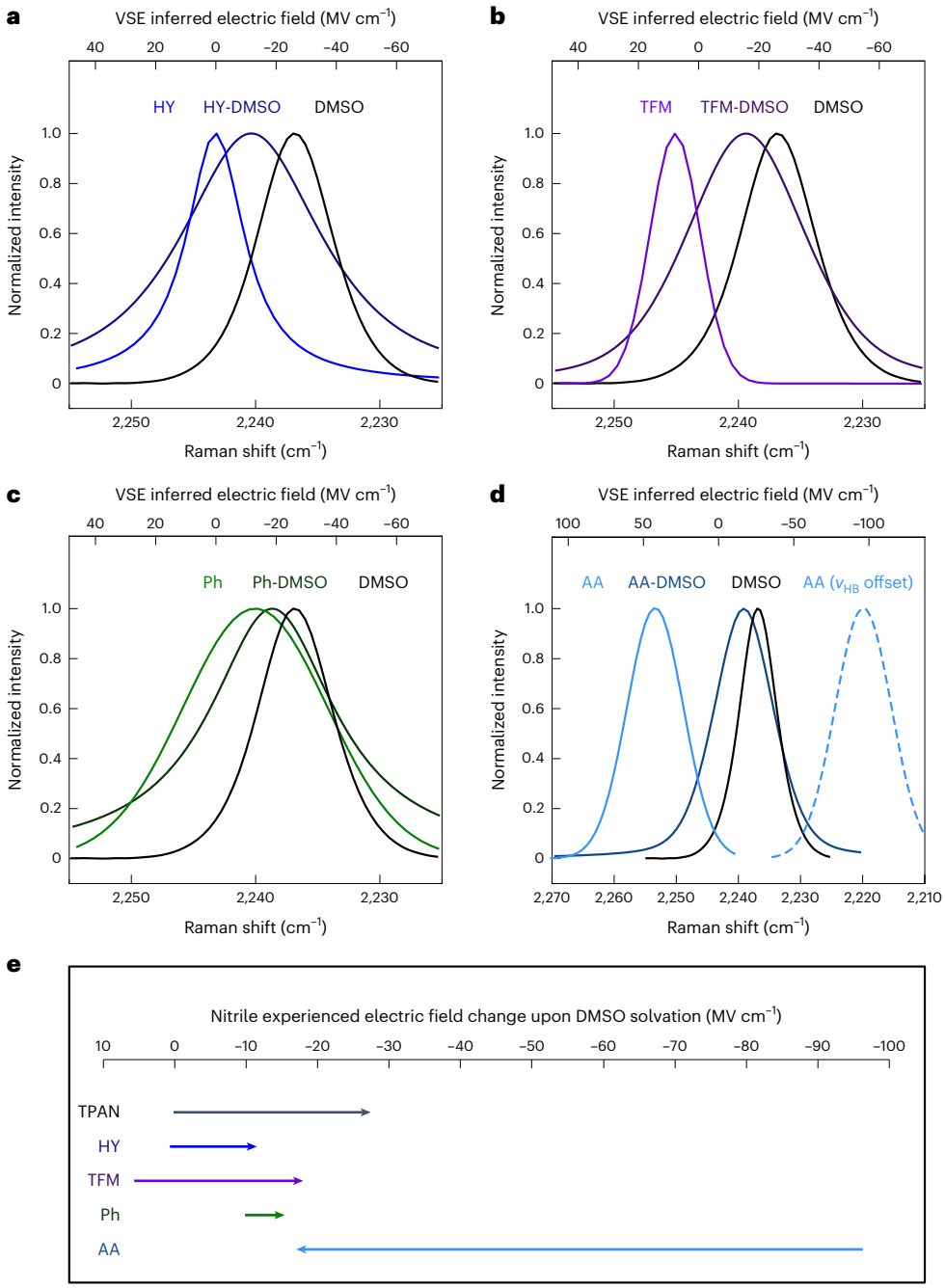

Fig. 4 | Spectroscopic observation and electrostatic quantification of solvation under nanoconfinement. a, Fitted Raman spectra for evacuated HY and the DMSO-solvated HY, overlaid with the infrared spectrum of TPAN in DMSO. **b**, Fitted Raman spectra for the TFM variant and the DMSO-solvated TFM variant, overlaid with the infrared spectrum of TPAN in DMSO. **c**, Fitted Raman spectra for the Ph variant and the DMSO-solvated Ph variant, overlaid with the infrared spectrum of TPAN in DMSO. **d**, Fitted Raman spectra for the AA variant and the DMSO-solvated AA variant, overlaid with the infrared spectrum of TPAN in DMSO. The dashed line plots a hypothetical AA spectrum as if there is no H-bond blueshift (33.5 cm^{-1}). **e**, Changes in the nitrile experienced electric field due to DMSO solvation. The start of the arrows represents the field in the evacuated MOF, while the end of the arrows represents a condition of DMSO-solvated MOF. The electric field for TPAN in DMSO was calculated using AMOEBA force fields. The electric fields for MOF variants in vacuum were calculated based on DFT. The lengths of the arrows, which represents the change in electric field magnitude upon DMSO solvation, was obtained from the observed frequency shifts and the corresponding VSE inferred electric fields shown in **a**–**d**.

of the change in field magnitude upon DMSO solvation (Fig. 4e, arrow length), the final total electric field (Fig. 4e, arrow end) provides a quantitative description of the solvent-filled MOF pore as a whole. The magnitude of electric fields produced by the DMSO-filled MOF pores sit in a narrow range from −12 to −18 MV cm^{-1}, regardless of the pre-installed electric field donors, manifesting the common effect of field screening by solvent. These fields are consistently smaller than that produced by the bulk DMSO solvation (−27.4 MV cm^{-1}), indicating that solvation under nanoconfinement provides unique chemical environments that are distinct themselves from solvation in bulk. Similar anomalous solvation was also observed for other solvents confined in the MOF nanopore (Supplementary Text 7 and Supplementary Fig. 37). Electric fields in confined environments may be related to the catalysis observed inside MOF pores and other supramolecular cages, and our

results indicate that to fully take advantage of the electric fields produced by the confined environment, one has to minimize the effect of field screening by the solvent, possibly by tailoring the pore size or installing functional groups to preclude solvent molecules or specifically organize solvent molecules.

Conclusions

We have shown that the PCN-521 MOF framework can be used as a general platform to create a series of non-covalent interactions using a modular molecular approach. The synthesized non-covalent interactions were interrogated by Raman spectroscopy and interpreted within the framework of the vibrational Stark effect giving the electric fields a donor exerts onto an acceptor. We found that the electric fields associated with non-covalent interactions are highly diverse, from being as destabilizing as +6 MV cm^{-1} (TFM) to being as stabilizing as −123 MV cm^{-1} (DCPh). The electric field provides an absolute, quantitative metric enabling broad comparisons across various chemical groups in terms of their electrostatic properties. Using the platform, we identified electric fields (HY) as weak as those in gas phase, positive fields (TFM) associated with destabilizing environment and H bonds (CPh, DCPh and AA) that are stronger than those in certain proteins. We further studied the non-covalent interactions involved in solvation by utilizing the microporous structure of the MOF to create solvent organizations that are inaccessible by the bulk. These results and analysis not only address fundamental questions about elementary interactions in chemistry, biology and material sciences, but also provide useful tools for molecular design and engineering, for example, the creation of novel catalysts using the principle of electrostatic catalysis.

Online content

Any methods, additional references, Nature Portfolio reporting summaries, source data, extended data, supplementary information, acknowledgements, peer review information; details of author contributions and competing interests; and statements of data and code availability are available at https://doi.org/10.1038/s41557-025-01916-7.

References

1. Furukawa, H., Cordova, K. E., O'Keeffe, M. & Yaghi, O. M. The chemistry and applications of metal–organic frameworks. *Science* **341**, 1230444 (2013).
2. Li, H., Eddaoudi, M., O'Keeffe, M. & Yaghi, O. M. Design and synthesis of an exceptionally stable and highly porous metal–organic framework. *Nature* **402**, 276–279 (1999).
3. Freund, R. et al. 25 years of reticular chemistry. *Angew. Chem. Int. Ed.* **60**, 23946–23974 (2021).
4. Wang, Y., Liu, Q., Zhang, Q., Peng, B. & Deng, H. X. Molecular vise approach to create metal-binding sites in MOFs and detection of biomarkers. *Angew. Chem. Int. Ed.* **57**, 7120–7125 (2018).
5. Yan, W. et al. Molecular vises for precisely positioning ligands near catalytic metal centers in metal–organic frameworks. *J. Am. Chem. Soc.* **142**, 16182–16187 (2020).
6. Chen, W. H. et al. Precise distance control and functionality adjustment of frustrated Lewis pairs in metal–organic frameworks. *J. Am. Chem. Soc.* **146**, 12215–12224 (2024).
7. Chattopadhyay, A. & Boxer, S. G. Vibrational Stark-effect spectroscopy. *J. Am. Chem. Soc.* **117**, 1449–1450 (1995).
8. Fried, S. D. & Boxer, S. G. Measuring electric fields and noncovalent interactions using the vibrational Stark effect. *Acc. Chem. Res.* **48**, 998–1006 (2015).
9. Park, E. S., Andrews, S. S., Hu, R. B. & Boxer, S. G. Vibrational stark spectroscopy in proteins: a probe and calibration for electrostatic fields. *J. Phys. Chem. B* **103**, 9813–9817 (1999).
10. Fried, S. D., Bagchi, S. & Boxer, S. G. Extreme electric fields power catalysis in the active site of ketosteroid isomerase. *Science* **346**, 1510–1514 (2014).
11. Fried, S. D., Bagchi, S. & Boxer, S. G. Measuring electrostatic fields in both hydrogen-bonding and non-hydrogen-bonding environments using carbonyl vibrational probes. *J. Am. Chem. Soc.* **135**, 11181–11192 (2013).
12. Suydam, I. T., Snow, C. D., Pande, V. S. & Boxer, S. G. Electric fields at the active site of an enzyme: direct comparison of experiment with theory. *Science* **313**, 200–204 (2006).
13. Slocum, J. D. & Webb, L. J. Measuring electric fields in biological matter using the vibrational Stark effect of nitrile probes. *Annu. Rev. Phys. Chem.* **69**, 253–271 (2018).
14. Fafarman, A. T. & Boxer, S. G. Nitrile bonds as infrared probes of electrostatics in ribonuclease S. *J. Phys. Chem. B* **114**, 13536–13544 (2010).
15. Yang, Y. Y., Feng, R. R. & Gai, F. 4-Cyanotryptophan as a sensitive fluorescence probe of local electric field of proteins. *J. Phys. Chem. B* **127**, 514–519 (2023).
16. Weaver, J. B., Kozuch, J., Kirsh, J. M. & Boxer, S. G. Nitrile infrared intensities characterize electric fields and hydrogen bonding in protic, aprotic, and protein environments. *J. Am. Chem. Soc.* **144**, 7562–7567 (2022).
17. Kirsh, J. M. & Kozuch, J. Hydrogen bond blueshifts in nitrile vibrational spectra are dictated by hydrogen bond geometry and dynamics. *JACS Au* **4**, 4844–4855 (2024).
18. Yang, Y. Y., Liu, J. S., Feng, R. R., Zhang, W. K. & Gai, F. C≡N stretching frequency as a convenient reporter of charge separation in molecular systems. *J. Phys. Chem. B* **127**, 6999–7003 (2023).
19. Du, J. J., Wang, H. M. & Wei, L. Bringing vibrational imaging to chemical biology with molecular probes. *ACS Chem. Biol.* **17**, 1621–1637 (2022).
20. Schneider, S. H., Kozuch, J. & Boxer, S. G. The interplay of electrostatics and chemical positioning in the evolution of antibiotic resistance in TEM β-lactamases. *ACS Cent. Sci* **7**, 1996–2008 (2021).
21. Ji, Z. et al. Protein electric fields enable faster and longer-lasting covalent inhibition of β-lactamases. *J. Am. Chem. Soc.* **144**, 20947–20954 (2022).
22. Ji, Z. & Boxer, S. G. β-Lactamases evolve against antibiotics by acquiring large active-site electric fields. *J. Am. Chem. Soc.* **144**, 22289–22294 (2022).
23. Zheng, C., Ji, Z., Mathews, I. I. & Boxer, S. G. Enhanced active-site electric field accelerates enzyme catalysis. *Nat. Chem.* **15**, 1715–1721 (2023).
24. Shrestha, R., Cardenas, A. E., Elber, R. & Webb, L. J. Measurement of the membrane dipole electric field in DMPC vesicles using vibrational shifts of *p*-cyanophenylalanine and molecular dynamics simulations. *J. Phys. Chem. B* **119**, 2869–2876 (2015).
25. Hu, W. H. & Webb, L. J. Direct measurement of the membrane dipole field in bicelles using vibrational Stark effect spectroscopy. *J. Phys. Chem. Lett.* **2**, 1925–1930 (2011).
26. Bagchi, S., Fried, S. D. & Boxer, S. G. A solvatochromic model calibrates nitriles' vibrational frequencies to electrostatic fields. *J. Am. Chem. Soc.* **134**, 10373–10376 (2012).
27. Zheng, C. et al. A two-directional vibrational probe reveals different electric field orientations in solution and an enzyme active site. *Nat. Chem.* **14**, 891–897 (2022).
28. Sarkar, S., Maitra, A., Banerjee, S., Thoi, V. S. & Dawlaty, J. M. Electric fields at metal–surfactant interfaces: a combined vibrational spectroscopy and capacitance study. *J. Phys. Chem. B* **124**, 1311–1321 (2020).
29. Delley, M. F., Nichols, E. M. & Mayer, J. M. Electrolyte cation effects on interfacial acidity and electric fields. *J. Phys. Chem. C* **126**, 8477–8488 (2022).

30. Zhang, M. W. et al. Symmetry-guided synthesis of highly porous metal–organic frameworks with fluorite topology. *Angew. Chem. Int. Ed.* **53**, 815–818 (2014).
31. Schneider, S. H. & Boxer, S. G. Vibrational Stark effects of carbonyl probes applied to reinterpret IR and Raman data for enzyme inhibitors in terms of electric fields at the active site. *J. Phys. Chem. B* **120**, 9672–9684 (2016).

Data availability

All data supporting the findings of this study are available in the Article and its Supplementary Information. Source data are provided with this paper.

Acknowledgements

This work was supported by the International Human Frontier Science Program Organization (no. RGP0047/2022 to S.W. and S.G.B.) and, in part, by NIH grant (no. GM118044 to S.G.B.). Part of this work was performed at the Stanford Nano Shared Facilities, supported by the National Science Foundation under award ECCS-2026822.We would also acknowledge the use of services from the Stanford Sherlock HPC facility. J.A. thanks the Ministerio de Ciencia e Innovación and the European Union–NextGenerationEU for a Juan de la Cierva Formación (no. FJC2021-048154-I to J.A.) research contract. F.P. and G.J.-O. thank MCIN/AEI (grant nos RYC2022-036457-I and EUR2023-143462 to F.P. and PID2021-125946OB-I00 and PDC2022-133725-C22 to G.J.-O.). We thank J. Kirsh, J. Kozuch, S. Fried and M. Asadi for discussions.

Author contributions

Z.J., S.W. and S.G.B. designed the research. Z.J. and S.M. performed the experiments and data analysis, including MOF synthesis, PXRD measurements, NMR spectroscopy, Raman spectroscopy and infrared spectroscopy. S.M., F.P. and G.J.-O. performed the computation. A.S. and J.A. synthesized the H_3LCN linker and supported the MOF synthesis. Z.J., S.M., J.A., S.W. and S.G.B discussed the results. Z.J., S.M., S.W. and S.G.B wrote the paper.

Competing interests

The authors declare no competing interests.

Additional information

Supplementary information The online version contains supplementary material available at https://doi.org/10.1038/s41557-025-01916-7.

Correspondence and requests for materials should be addressed to Zhe Ji, Stefan Wuttke or Steven G. Boxer.

Peer review information *Nature Chemistry* thanks the anonymous reviewers for their contribution to the peer review of this work.

nature chemistry

Supplementary information

https://doi.org/10.1038/s41557-025-01916-7

Electrostatic atlas of non-covalent interactions built into metal–organic frameworks

In the format provided by the authors and unedited

Table of Contents

Materials and Methods

1. Materials

All chemicals were purchased from commercial suppliers and used as received without further purification unless otherwise mentioned. 1,4-Dibromobenzene (99%, Acros Organics, 106-37-6), n-Butyllithium (1.6 M solution in hexane, Acros Organics, 109-72-8), trimethylsilyl cyanide (TMSCN, 98%, Acros Organics, 7677-24-9), 4-(Methoxycarbonyl)benzeneboronic acid (97%, Fluorochem, 99768-12-4), Dichlorobis(triphenylphosphine)palladium(II) (98%, Fluorochem, 13965-03-2), sodium hydroxide (NaOH, >98%, LABKEM, 1310-73-2), hydrochloric acid (HCl, LABKEM, 7647-01-0), ammonium chloride (NH_4Cl, 99%, LABKEM, 12125-02-9), magnesium sulfate hydrate (>99%, Carl Roth, 22189-08-8), indium(III) bromide (99.99%, Acros Organics, 13465-09-3), sodium hydrogen carbonate ($NaHCO_3$, LABKEM, >99%, 144-55-8), diethyl carbonate (99%, Acros Organics, 105-58-8), ethyl acetate (>99.8%, LABKEM, 141-78-6), dichloromethane (DCM, 99.8%, dried over molecular sieves, Acros Organics, 75-09-2), n-Hexane (>= 99%, Carl Roth, 110-54-3), tetrahydrofuran (THF 99.85%, < 0.0057 H_2O, freshly opened, Acros Organics, 109-99-9), methyl tert-butyl ether (MTBE, 99.9%, Acros Organics, 1634-04-4), Celite 545 (Diatomaceous earth) (Acros Organics, 68855-54-9), Zr(IV) Chloride (Thermo scientific, 98% anhydrous) and Hf (IV) Chloride (Aldrich).

2. Synthesis of H_3LCN

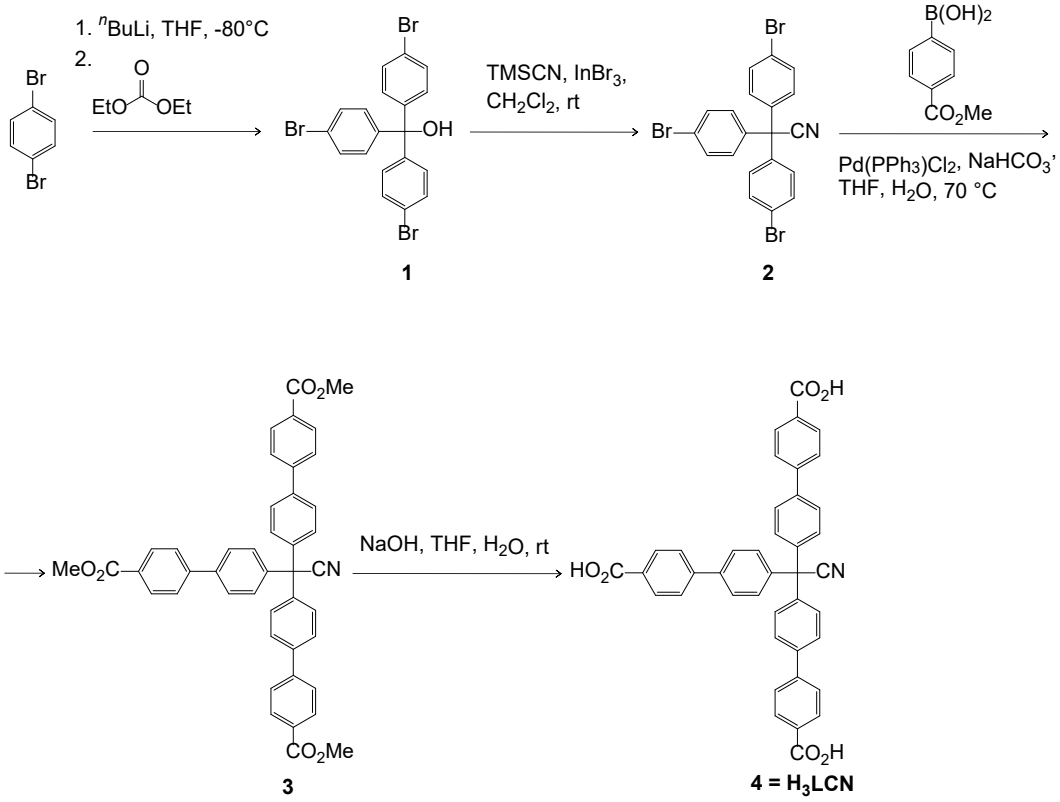

Scheme for the synthesis of H_3LCN (**4**)

Tris(4-bromophenyl) methanol (**1**)

Tris(4-bromophenyl) methanol (**1**) was synthesized accordingly to previously a reported procedure with slight modifications.[1] p-dibromobenzene (129.75 g, 550 mmol) and THF (1.0 L) were added to a flame-dried 3-neck 2 L round-bottom flask equipped with a stir bar, three-way vacuum inlet adapter, glass stopper, and septum. The solution was cooled to -80 °C and n-BuLi (200 mL, 500 mmol) was added dropwise. Separately, diethyl carbonate (15.1 mL, 125 mmol) was put in a flame-dried 300 mL round-bottom flask equipped with a stir bar, septum, and nitrogen inlet needle and cooled to -80 °C. After 3 hours stirring of the solution containing the lithiated species the diethyl carbonate solution was transferred to it through a cannula and in 30 minutes the solution was subsequently allowed to warm to room temperature (23 °C). After 20 h, the reaction mixture was quenched with saturated aqueous NH_4Cl (200 mL). The crude product was extracted with EtOAc (250 mL). The organic fractions were collected,

washed with water (2x100 mL), brine (100 mL), and dried over anhydrous $MgSO_4$. The crude solid was dry loaded onto SiO_2 and chromatographed using a gradient of hexanes to 25% EtOAc:hexanes (v/v) to yield 20.131g (32.4%) of **1** as a white solid. **1**: ^{1}H NMR (500 MHz, $CDCl_3$, 298 K): δ 7.47 (d, 6H), 7.14 (d, 6H), 2.71 (s, 1H) ppm. ^{13}C NMR (125 MHz, $CDCl_3$, 298 K) δ 144.88 (s, 3C), 131.36 (s, 6C), 129.48 (s, 6C), 121.99 (s, 3C), 81.13 (s, 1C) ppm.

Tris(4-bromophenyl) acetonitrile (**2**)

Tris(4-bromophenyl) acetonitrile (**2**) was synthesized accordingly to a previously reported procedure with slight modifications.[2] $InBr_3$ (893 mg, 2.52 mmol, 0.1 eq) was dissolved in 60 mL of anhydrous DCM in a flame-dried 250 ml Schlenk flask and cooled down to 0°C, then TMSCN (5.000g, 50.398 mmol, 2.0 eq) was added. Tris(4-bromophenyl) methanol (**1**) (12.524 g, 25.199 mmol, 1 eq) was dissolved in 40 mL of anhydrous DCM and added dropwise during 15 minutes to the reaction mixture and stirred for 1 h. The solvent was removed under reduced pressure. The residue was dissolved in DCM and absorbed onto Celite. The crude product was purified by flash column chromatography (SiO_2, DCM/Hex = 100:0→80:20). A colourless crystalline solid of **2** was obtained (11.704 g, 92%). **2**: ^{1}H NMR (500 MHz, $CDCl_3$): δ 7.51 (d, 6H), 7.06 (d, 6H) ppm; ^{13}C NMR (125 MHz, $CDCl_3$): δ 138.29 (s, 3C), 132.19 (s, 6C), 130.27 (s, 6C), 123.09 (s, 3C), 122.09 (s, 1C), 56.25 (s, 1C) ppm; HR-MS: $C_{20}H_{12}Br_3N^+$, calculated: 504.85 [M^+], observed: 504.8507 [M^+].

Tris-(4,4',4''-methoxycarbonylbiphenyl)-acetonitrile (3).

Tris-(4,4',4''-methoxycarbonylbiphenyl)-acetonitrile (**3**) was synthesized according to a previously reported procedure with slight modifications.[3] In a 500 ml round bottom flask, **3** (5.000 g, 9.881 mmol), 4-(methoxycarbonyl) phenyl-boronic acid (6.213 g, 34.523 mmol) and freshly distilled THF (100 mL) were added to form a colourless solution. Saturated aqueous $NaHCO_3$ solution (100 mL) was added, and the reactor degassed and filled with argon for three times.

Dichlorobis(triphenylphosphine)palladium (II) (346.76 mg, 0.494 mmol, 5 mol %) was added and the reaction mixture was heated to 75 °C and stirred for 20 hours. The reaction mixture was then separated, and the water layer washed 3 times with 200 ml of EtOAc. The organic

layers were recombined with the organic portion and washed 3 times with water, dried over $MgSO_4$, filtered and dried under vacuum. The residue was taken up in a minimum volume of DCM and adsorbed on 45 g of Celite. The crude product was purified by flash column chromatography (SiO_2, Pure DCM). Total yield of **3** is 3.527 g (53%). **3**: ^{1}H NMR (($CDCl_3$), 500 MHz) δ 8.14 (d, 6H), 7.68 (dd, 12H), 7.43 (d, 6H), 3.97 (s, 9H) ppm; ^{13}C NMR (125 MHz, $CDCl_3$): δ 166.84 (s, 3C), 144.31 (s, 3C), 140.14 (s, 3C), 139.76 (s, 3C), 130.26 (s, 6C), 129.44 (s, 3C), 129.39 (s, 6C), 127.72 (s, 6C), 127.06 (6C), 122.90 (s, 1C), 56.80 (s, 1C), 52.21 (s, 3C) ppm;. EI-MS: $C_{44}H_{33}NO_6^+$, calculated: 671.23 [M^+], observed: 670.89 [M^+].

Tris-(4,4',4''-carboxylbiphenyl)-acetonitrile (4)

Compound **4** (5.00 g, 7.45 mmol) was dissolved in freshly distilled THF (100 mL). To the colourless solution was added an aqueous solution of NaOH, prepared dissolving 7.450 g of NaOH pearls in 17 ml of water. The reaction mixture was stirred at room temperature for 20 hours. The reaction mixture was then acidified to pH 1 with 125 ml of 2M HCl. To the mixture 50 ml of MTBE were added to facilitate layer separation. The organic layer was separated and washed 3 times with water, then dried with $MgSO_4$, filtered and vacuum dried. The resulting white powder is the desired product **4** (3.742 g, 80%). **4**: ^{1}H NMR ((d_6 DMSO), 500 MHz) δ 13.01 (s, 3H), 8.02 (d, 6H), 7.87 (d, 6H), 7.83 (d, 6H), 7.37 (d, 6H) ppm; ^{13}C NMR (125 MHz, $CDCl_3$): δ 167.53 (s, 3C), 144.56 (s, 3C), 139.75 (s, 3C), 139.65 (s, 3C), 130.56 (s, 3C), 130.50 (s, 6C), 129.44 (s, 6C), 128.26 (s, 6C), 127.44 (6C), 123.08 (s, 1C), 56.78 (s, 1C) ppm.

3. Synthesis of MOFs

Synthesis of PCN-521 and PCN-523

PCN-521 was synthesized according to a reported method.[4] Into a 20 mL glass vial were added 10 mg of $ZrCl_4$, 12 mg of H_4L (L = 4',4'',4''',4''''-methanetetrayltetrabiphenyl-4-carboxylate), 1.7 mL of *N,N*-diethylformamide, and 0.2 mL of trifluoroacetic acid. The mixture was sonicated for 20 min to produce a uniform dispersion before incubated at 120℃ for 22 hours. The vial was allowed to slowly cool down to room temperature to yield colorless, octahedral crystals. For pore activation, the crystals were soaked in 20 mL of *N,N*-dimethylformamide (DMF) for 20 min. The vial was decanted and replenished with another fresh 20 mL DMF. The wash was repeated 4 times with DMF, 4 times with methanol, 4 times with acetone, 4 times with hexane, and one time with perfluoropentane. The crystals were evacuated at room temperature until the pressure reached 50 mTorr.

PCN-523 was also synthesized in a similar fashion with a few modifications. Into a 20 mL glass vial, 6 mg of $HfCl_4$, 5 mg of H_4L (L = 4',4'',4''',4''''-methanetetrayltetrabiphenyl-4-carboxylate), 0.9 mL of *N,N*-diethylformamide, and 0.1 mL of trifluoroacetic acid were added. The mixture was sonicated for 20 min to produce a uniform dispersion before incubated at 120 ℃ for 22 hours followed by slow cooling to room temperature to yield octahedral PCN-523 crystals.

Synthesis of the TFM variant

The TFM variant was synthesized the same way as PCN-521, except for adding 5 mg of H_3LCN into the reaction mixture. For PCN-523, 2.5 mg of H_3LCN was used.

Synthesis of HY and other variants

After washing the TFM PCN-521 (or -523) crystals with MeOH, the crystals were soaked into 20 mL of methanol solutions of the corresponding carboxylic acids (~0.1 M) for 2 hours. The vial was decanted before replenished with another fresh carboxylic acid solutions. The soaking was repeated twice before washing with methanol for 4 times. The above procedure was continued from the step of acetone washing until finishing the last step of evacuation.

MOF digestion for NMR measurements

2 mg of the MOF crystals were mixed with 580 µL d_6-DMSO and 20 µL HF (aq. 43%). The mixture was sonicated at 60℃ for 90 min. The obtained clear solution indicated the complete digestion of the crystals. Additional 20-50 µL of DMSO was added if the solution was not clear after sonication. The solution was measured by liquid ^{1}H-NMR.

4. Spectroscopic methods and data analysis

NMR Spectroscopy

NMR experiments for H_3LCN synthesis were carried out at 25 ºC on a Bruker AV500 spectrometer, equipped with a 5 mm z-gradient BBI probe, operating at 500 MHz and 125.77 MHz frequency for proton (^{1}H-NMR) and carbon (^{13}C-NMR) respectively. Data acquisition and processing was performed with TOPSPIN 2.1 software (Bruker). Pulse sequences were those standards of Bruker. Chemical shifts are referenced to the deuterated solvent residual signal ($CDCl_3$-d_1: δ 7.24 ppm, and DMSO-d_6: δ 2.50 ppm) and reported in ppm downfield.

For MOF digestion NMR experiments, ^{1}H-NMR spectra were recorded on a Varian VNMRS-400 MHz instrument and are reported in ppm using solvent as an internal standard (DMSO-d_6: δ 2.50 ppm). Because a considerable amount of HF (aq. 43%; 1.5% in final volume) was added to digest the crystals, baselining was performed manually using MestReNova 14.0 before peak integration. Phase correction (if necessary) was also performed.

NMR Data Analysis

Using NMR spectra for digested MOFs, these MOFs' chemical composition can be estimated. The doped H_3LCN can be quantified by subtracting the integrated area of the combined H_3LCN and H_4L proton peaks from that of the H_4L proton peaks alone (see peak assignment in Supplementary Figure 13). The carboxylate field donors can be quantified by integrating the area of their proton peaks, except the CF_3COO^- ligand in the TFM variant which has no protons. By doing this, ratios of H_4L: H_3LCN : Field donor were obtained and presented in Supplementary Table 1.

Based on the structure of PCN-521, the stochiometric ratio of Zr cluster to the organic linker is 1:2, that is $n_{ZrCluster} = 0.5\ (n_{H4L} + n_{H3LCN})$. Each Zr cluster can be maximally coordinated by 12 carboxylate ligands, among which 8 come from the linker making the backbone, being either H_4L or H_3LCN. The rest 4 coordinate sites can be taken by the field donors, the carboxylate modulator used for MOF synthesis, the decomposition products of DEF, water, or hydride ions. When calculating the occupancy of the field donor, not only we consider the defect site left by

H_3LCN, but also these 4 “bystander” sites which are far away from nitrile. Therefore, the occupancy of the field donor = $n_{FieldDonor}$ / (n_{H3LCN} + 4 $n_{ZrCluster}$). The data are presented in Supplementary Table 1.

FTIR Spectroscopy

The FTIR spectra of the H_3LCN and the TPAN solutions were measured using a Bruker Vertex 70 FTIR spectrometer equipped with a liquid nitrogen-cooled mercury cadmium telluride detector and under constant purging of the sample chamber with dry air, similarly to previous works.[14] 20 μL of the samples were loaded into a demountable cell composed of two CaF_2 optical windows (19.05 mm diameter, 3 mm thickness, Lambda Research Optics). The windows were separated by two Teflon spacers, one 25 μm thick and the other 50 μm to avoid fringes. Before FTIR measurement, a 5 min delay was applied to purge gaseous CO_2, and then 256 scans were acquired and averaged to obtain each transmission interferogram which were converted to absorbance spectra using a negative logarithmic value of the transmission data. Spectra were recorded in window of 4000−1000 cm^{-1} with 1 cm^{-1} resolution. Blank solvent spectra were recorded under the same condition and used as a reference for subtracting the background. Data collection and processing were performed using the software OPUS 5.0. Peak positions and the full width at half maximum (FWHM) were determined using CurveFit (combination of Lorentzian and Gaussian) in OPUS 5.0.

Raman Spectroscopy

To assess the vibrational frequency shifts of the nitriles embedded in the MOF crystals, we measured their Raman spectra. Nitriles exhibit relatively strong Raman intensities, and a small μm-sized laser spot in a confocal Raman microscope requires only <10 mg of MOF crystals. However, in addition to the lack of information on absolute concentrations, the Raman intensities are not a reliable way to evaluate the transition dipole moments, leading us to rely on frequency shifts to estimate fields in this study.

Raman spectra of MOF samples were collected using a Raman spectrometer (Horiba XploRA Confocal) at the Stanford Nano Shared Facility core. A 638 nm laser and a monochromator groove density grating of 1800 were found to be optimal in terms of signal-to-noise ratio for

measuring the nitrile stretch in the crystalline powder MOF samples. The confocal hole was typically set to 150 μm for all experiments. The instrument was calibrated using these settings on a piece of silicon wafer (Calibration peak at 521 cm^{-1} corresponding to Si) before each measurement. To maintain consistency between the frequencies reported by the Bruker Vertex 70 FTIR instrument and those obtained from the Raman microscope, we conducted tests to further calibrate the nitrile stretch of the linker molecule, ensuring no systematic frequency variation was observed between the two instruments. A 100x short working distance Olympus MPLan N objective (NA=0.9, 0.21 mm working distance) was used to collect backscattered light (spot size 451 nm at 638 nm). The laser power typically used was around 8 mW at the spot.

Freshly evacuated MOF samples with confirmed crystallinity (confirmed via PXRD measurements) were dispersed on a clean glass slide and positioned on the microscope stage. The laser was focused onto the sample by maximizing and optimizing the scattering intensity from the strong peaks corresponding to the C=O stretches around the 1600 cm^{-1} range emanating from the MOF backbone, at lower laser irradiances with the real time display (RTD) module of Labspec6 program, where acquisition was set to 1-2s. Longer scans (>100 s) were performed at maximum laser power (100%) from three technical replicates at different spots to minimize photodamage. To measure solvation under nanoconfinement in the MOF, only high-boiling-point solvents like DMSO with low vapor pressure were used, ensuring that evaporation would not occur during data acquisition. The averaged data and their fits are reported in Supplementary Figure 30.

For polarized Raman measurements, an incoming polarizer and an exit polarizer were used to measure polarized Raman spectra. For the PCN-521 crystals, a 638 nm laser with a 1800 lines/mm grating was employed to maintain consistency with the measurements of shifts presented in the paper. This setting provides higher signal to noise ratios for the MOF crystals. In this case, the nitrile stretch intensity was nearly zero in the scattering when the signal was collected perpendicular to the excitation for either laser or grating settings, which validated the polarization measurements. Data corresponding to the measurements for the are reported in Supplementary Figs. 21 and 22.

Powder X-Ray Diffraction

X-ray diffraction measurements were conducted using a PANalytical Empyrean X-ray diffractometer, employing a Cu (8.04 keV, 0.15406 nm) source X-ray tube and a scintillator detector at the Stanford Nano Shared Facility cores. Symmetrical 2θ-ω scans were performed using the mirror-parallel plate collimator module of the Empyrean instrument. For instrument alignment, a 1/32° divergence slit was utilized in the incident beam path alongside a 10 mm mask. During the diffraction experiments, the slit was adjusted to 1/16°, and the mask size was increased to 20 mm. A 0.02° Soller slit was employed for the incident optics. The parallel plate collimator (0.27°) was paired with a receiving slit, and a 0.125 mm programmable beam Ni attenuator was incorporated into the diffracting optics. Additionally, a 0.04° Soller slit was employed for the receiving optics. A brief 1° scan was initially conducted to align the instrument to 2θ=0°. Freshly evacuated samples were dispersed on a glass slide and compacted into a ~2cm x 2cm square. The z-height of the stage was adjusted using a focusing laser and a camera. Typically, scans ranging from 2θ 0-25 degrees were carried out for each sample. PXRD data is presented in Supplementary Figure 12.

5. Computational Details

a. Molecular Dynamics Simulations with Fixed-Charge Force Fields (GAFF) for Estimating Fields for Solvatochromic Calibrations

For calculating the solvent electric fields on H_3LCN and TPAN, fixed-charge MD simulations were carried out similarly to previous works.[6,14,15] The molecule of interest was optimized to the lowest energy conformation of the molecule using Density Functional Theory (DFT) in Gaussian 16 at the B3LYP/6-311++G(2d,2p) level.[16] The resultant structure was then used for parameterization through the Antechamber program of AmberTools16 based on GAFF (Generalized AMBER Force Field).[17,18] The force field parameters for organic solvents were taken from Caleman *et al*., and water was parameterized using the TIP3P model.[19, 20] All simulations were performed on GROMACS 2018.[21] A single solute molecule was placed in the center of a cubic solvation box that has a size of 40×40×40 $Å^3$ filled with solvent molecules. Under periodic boundary conditions, the system was first energy minimized until the maximum force is less than 1000 kJ/mol/nm (or ~20 kcal mol^{-1} $Å^{-1}$), followed by NVT and NPT equilibration runs (100 ps for each). MD production runs were performed as 10 ns trajectories with a 2 fs timestep, with a van der Waals cutoff of 10 Å (with analytical vdW correction), an electrostatics cutoff of 10 Å (using the particle mesh Ewald method), an SD (leap-frog stochastic dynamics) integrator, the Berendsen thermostat and the Parrinello-Rahman barostat.[22,23,24] LINCS algorithm was used for bond constraints.[25]

The electric field vectors on the relevant atoms (C and N) were obtained via dividing the electrostatic forces acting on these atoms by the corresponding atomic charges. To extract the solvent contributions to the electric fields, the MD frames obtained were recalculated with atomic charges on all solvent molecules zeroed out, providing the field contributions from the solute atoms themselves which were then subtracted from the electric field values obtained in the original production run. The electric field projections along the -C≡N directions are then evaluated using the following equation:

$$F_{\mathrm{CN}} = \frac{1}{2}\left(\vec{F}_{\mathrm{C}} \cdot \hat{r}_{\mathrm{CN}} + \vec{F}_{\mathrm{N}} \cdot \hat{r}_{\mathrm{CN}}\right)$$

where F_{CN} denotes the field projection along the C≡N bond, $\vec{F}_C$ and $\vec{F}_N$ are the electric fields acting on the C and N atoms, respectively, and $\hat{r}_{CN}$ refers to a unit vector along the direction of the -C≡N bond.

b. Molecular Dynamics Simulations with Polarizable Force Fields (AMOEBA) for Estimating Fields for Solvatochromic Calibrations

Polarizable molecular dynamics simulations were performed using GPU-accelerated Tinker9 software and the AMOEBA09 force field on the Stanford University Sherlock High Performance Computing Cluster. Tinker9, used here is built on the Tinker8 framework.[26-28] Parameters for TPAN and solvents were parameterized with Poltype2,[29,30] fitting multipoles to electrostatic potentials derived from MP2/6-311++G(2d,2p) calculations in Gaussian 16. Solvent parameters were compared to those used in our previous studies and solute parameters have been reported in the SI.[9] The solute was positioned in the center of a solvent-filled 40x40x40 $Å^3$ cubic box using the Packmol suite, under periodic boundary conditions.[31] The solute/solvent systems were energy minimized using the steepest descent method until the energy gradient was less than 0.5 kcal mol^{-1} $Å^{-1}$. This was followed by 50 ps of NPT equilibration at 300 K and 1 bar and 200 ps of NVT equilibration at 300 K. A 1 fs timestep was used with a Beeman integrator. Additional settings included the particle mesh Ewald method, analytical van der Waals correction, a Velocity-Verlet integrator, an Andersen thermostat, and a Berendsen barostat with a time constant of 1 ps during the NPT step. [22, 23, 32]

Three independent production runs were conducted over 5 ns with an induced dipole moment threshold of 10^{-5} D, a van der Waals cutoff of 12.0 Å, a Monte-Carlo barostat with an inverse friction of 1 ps, and "molecular" volume scaling. Conditions were like those used in the NPT equilibration step. Induced dipoles were extracted every 0.1 ps both in the presence and absence of the solvent (at similar atomic coordinates). The resulting difference provided the solvent-induced dipoles, which were then divided by the atomic polarizabilities to determine the electric field vectors for the C ($\vec{F}_C$) and N ($\vec{F}_N$) atoms. The average electric field projected along the -C≡N bond, $|\vec{F}|$, was calculated in a fashion as similar for MD where

$$F_{CN} = \frac{1}{2}(\hat{\mu}_{CN}.\vec{F}_C + \hat{\mu}_{CN}.\vec{F}_N)$$

The calculations were performed using scripts available in the public GitHub repository: https://github.com/KozuchLab/Publications/tree/main/oCNPhe_GROMACS_TINKER.

The comparative analysis of results from the run of TPAN with o-Tolunitrile reveals a significant difference in field strength measurements between AMOEBA and GAFF (AMBER). Field-field plots indicate that AMOEBA reports fields approximately 1.2 times higher on average than those reported by fixed-charged force-fields. This discrepancy highlights the influence of the multipole expansion inherent to polarizable force fields such as AMOEBA. The higher field values reported by AMOEBA suggest that its inclusion of explicit polarization effects results in higher stabilizing fields on the nitrile oscillator compared to the fixed-charge nature of GAFF. Therefore, the results convincingly demonstrate that the polarizable nature of AMOEBA can indeed yield higher fields, reflecting the importance of accounting for polarization in such systems.

c. DFT calculations of H3LCN and TPAN and in-silico Stark effect

The unconstrained geometry optimization of the TPAN model compound and the H_3LCN linker at the B3LYP/6-31G+(d) level of theory yields an expected sp^3 hybridized geometry around the carbon bearing the nitrile group (Supplementary Figure 28). However, the crystal structure of PCN-521 indicates a strained geometry around this carbon where the angles along the C-C-C bonds are strained by ~10° or more. (CCDC: DITJOH) To test whether the Stark tuning rate obtained from solvatochromic calibrations holds for this perturbed geometry expected in the MOF, we performed "*in-silico*" Stark measurements.[14] A homogeneous external and *in-silico* field was applied along a bond axis of the nitrile. We conducted this exercise on both the freely optimized TPAN molecule, and an optimized but strained TPAN based on MOF geometry seen for H_4L, where heavy atoms were frozen to constrain TPAN to a MOF geometry (excluding the nitrile). Once the geometries optimized and were confirmed with no imaginary frequencies, we reoriented the molecule to align its z-axis (along the nitrile) with the applied *in-silico* electric field. Under this scheme, the zero-field the difference in the absolute frequencies of both geometries was ~1cm^{-1}. Subsequently, we applied incremental electric fields of 2.5 MV/cm along this direction using the Gaussian keyword "Field" and allowed the system to reoptimize and we performed a frequency calculation and ensured no significant changes in the molecular geometry occurred with the optimization (Supplementary Figure 29). With this *in-silico* analysis we observed a perfect linear trend of the obtained frequencies with applied fields for both geometries. From this, we obtained *in-silico* Stark

tuning rates for the TPAN model compound in the strained MOF geometry compared to the free geometry. We noted that the strained geometry exhibited a minimally higher Stark tuning rate (0.36 cm^{-1}/MV/cm vs. 0.33 cm^{-1}/MV/cm) compared to the relaxed geometry. These numbers are very consistent with the Stark tuning rates we obtained from the solvatochromic calibrations of TPAN using AMOEBA fields.

d. Cluster DFT calculations of the MOF defect site

Subsequently, to simulate the defect site we carried out constrained cluster geometry optimizations using Gaussian 16 with the B3LYP hybrid functional, 6-31G(d) basis set, and double-zeta Los Alamos National Laboratory (LANL2DZ) effective core potential for Zr, along with ultrafine integration grids (Data in Supplementary Table 8).[34,35] Multiple conformations based on single bond rotations were considered for all starting structures. All stationary points were characterized by frequency analysis performed at the same level as the geometry optimizations, from which thermal corrections were obtained at 298.15 K and 1 atm using GoodVibes 3.2.[36] (Supplementary Table 8) The quasi-harmonic approximation reported by Grimme was used to correct vibrational entropy,[37] with entropic terms for frequencies below a cutoff value of 100 cm^{-1} obtained from the free-rotor approximation. The calculated nitrile - C≡N stretching frequencies were corrected using the corresponding scaling factor for the level of theory taken from the NIST Standard Reference Database (0.96, https://cccbdb.nist.gov/vibscalejust.asp). Gibbs free energies (ΔG) were used to assess the relative stabilities of conformers. Only conformers with a Boltzmann factor ($e^{-\frac{\Delta G}{RT}}$) at 298.15 K greater than or equal to 0.01 (energy differences below 2.5 kcal/mol) with respect to the absolute minimum are presented in Supplementary Table 8. Molecular models for monodentate carboxylic acid substitutions were built using the crystallographic coordinates of PCN-521 (CCDC: DITJOH), preserving part of the octahedral Zr cluster to which the monodentate carboxylic acid is coordinated. Cartesian coordinates of the terminal atoms were frozen to the crystallographic values. An example of a molecular model is shown in Supplementary Figure 36 (trifluoroacetic acid, TFM). Atoms shown as spheres were frozen in Supplementary Figure 36, while atoms shown as sticks were allowed to optimize. The Cartesian coordinates of the optimized geometries have been provided at the end of the supplementary text in this manuscript.

e. Estimating the changes in electric fields and quantifying H-Bond shifts using Electrostatic Potential (ESP) calculations

In all cases, the Gaussian keyword "prop=efg" was used to compute electrostatic properties of the optimized MOF cluster (Supplementary Figure 36). Typically, the field calculated from the electrostatic potential of the solute-solvent system includes the solute's own field. To isolate only the solvent-induced field on the solute, which is what we desire, two partitioning schemes can be considered.

In the first method, ESPs are calculated both with and without the solvent (or MOF environment in this case). The electric field exerted by the explicit solvent on the solute is determined by subtracting the field calculated for the solute alone (in the same geometry but without the solvent). This method is comparable to the way fields have been calculated from each snapshot in the MD trajectory on the nitrile of TPAN. This method, referred to as "**QM1**," was used by Wang *et al*. to calculate the protein-induced field in the active site of the enzyme ketosteroid isomerase.[10, 38] In a different method proposed by Saggu *et al*., a single-point calculation is performed where the solute is removed from the solvent, and the electrostatic potentials are calculated at the points where the vibrational probe of interest solute (the nitrile bond) would have been by using "ghost atoms." We denote this approach as "**QM2**". (Supplementary Figure 36) **QM2** was utilized to quantify the field in the non-covalent interactions in the direct measurements of electric fields in weak OH···π H-bonds.[39] Each method makes different assumptions: **QM1** assumes the solute's electronic structure is similar in and out of the solvent, allowing subtraction to yield the solvent-only field and **QM2** assumes the solvent's electronic structure is not significantly affected by the solute's presence or absence. In this work we estimated fields using a modified version of **QM2**, where we aim to isolate the field acting on the nitrile specifically from the field donor in the optimized geometry.[39] To achieve this, we freeze atoms in the geometry of the field donor from the cluster DFT calculations and then cap the alpha-carbon of the donor with a methyl group. This isolates the field donor's perturbation on the ghost atoms representing the nitrile moiety (see scheme presented in Supplementary Figure 36). Therefore, electric field along the nitrile bond length based on "ghost atom" approach is consequently represented as:[39]

$$F_{CN}(MV\ cm^{-1}) = \frac{[\varphi_C(a.u.) - \varphi_{C\_ref}(a.u.)] - [\varphi_N(a.u.) - \varphi_{N\_ref}(a.u.)]}{\frac{d_{C-N}(\text{Å})}{0.529(\text{Å}\ bohr^{-1})}} \cdot 5142.2\ (MV\ cm^{-1}\ a.u.^{-1})$$

where F_{CN} denotes the electric field, φ_{C} & φ_{N}represent the electrostatic potentials at carbon and nitrogen atoms respectively while $\varphi_{\mathrm{C\_ref}}$ & $\varphi_{\mathrm{N\_ref}}$ are reference potentials that are considered to be zero, and $\vec{d}_{\mathrm{CN}}$ is the bond length between carbon and nitrogen atoms. As presented in Supplementary Table 9, the value of $\vec{d}_{\mathrm{CN}}$ varies minimally. In Gaussian, the electrostatic potential (φ) is reported in atomic units (a.u.). In atomic units, the unit of electrostatic potential is Hartree per elementary charge (e), a conversion factor of 1 au ≡ 5.14225 GV cm^{-1} is consequently used for unit conversions.

In summary, the modified **QM2** method was used because it is better benchmarked for quantifying weak non-covalent interactions, which are discussed in this study.[39,40] Notably, the variability between the **QM1** and **QM2** methods in calculating the solvent-induced field on a solute arises from their treatment of polarizability. The **QM1** method assumes that the solute's electronic structure remains unchanged between solvated and unsolvated states, which can result in significant differences in the electrostatic potential map and, consequently, in the calculated solvent-induced field. In this treatment, the modified **QM2** method does have a few caveats and may lose some information about the polarization of the field donor due to the solute and the extended framework of the MOF. However, it successfully captures the field explicitly from the specific non-covalent interaction expected from the field donor alone on the nitrile. While **QM2** assumes that the solvent's electronic structure is not significantly polarized by the solute and the backbone, it is a more reasonable assumption than the solute's polarizability information being lost, although it still deviates from more accurate and benchmarked partition methods such as Subsystem Projected AO Decomposition (SPADE) and Absolutely Localized Molecular Orbitals (ALMO). While ALMO and SPADE could be employed as future directions, we have limited our approach here to the **QM2** method as proposed by Saggu.[39] A comprehensive comparison of these methods (QM1, QM2, ALMO, SPADE etc.) can be found in recent work by Fried et al., where each was tested for estimating the linear Stark tuning rate of deuterium-replaced transferable hydrides in model systems for nicotinamide-based cofactors such as NADH and NADPH.[40]

Supplementary Texts

Supplementary Text 1. **Electric fields associated with noncovalent interactions**

Chemical groups that participate in noncovalent interactions can be mostly represented as charges and dipoles interacting with each other through their produced electric fields. Using a typical hydrogen-bonded nitrile as an example, the proton uses its positive charge to impose an electric field onto the nitrile dipole. This electrostatic language applies to noncovalent interactions in general whether the field donor is a proton or an ion, a dipole or an induced dipole. Dependent on the field donor's potency for producing electric fields, the magnitude of the electric field experienced by a field acceptor can vary in a wide range, from almost 0 to as large as -100 MV/cm.

These values have been obtained based on the vibrational Stark effect, by which a field acceptor acts as a vibrational probe whose frequency encodes information about the local electric field projected onto the axis of the chemical bond. In the case of nitrile, the electric field magnitude inferred from the vibrational frequency shift corresponds to the field element along the C-N axis. Although the field must be heterogeneously distributed (e.g. the N atom experiences larger fields than C because the N is closer to the field donor), the routine is to use the mean value of the fields at the geometrical center of the bond, because the nitrile probe is calibrated based on the molecular dynamics and DFT simulations where the field is defined and calculated as the mean field with the same geometrical description, relevant to the dipolar picture.

Describing noncovalent interactions in terms of dipoles experiencing mean electric fields is especially valuable in understanding chemical reactivity in complex environments such as enzymes, which are often pre-organized to facilitate catalysis. A landmark study by Fried and Bagchi demonstrated this principle in the enzyme ketosteroid isomerase (KSI), revealing that exceptionally strong electric fields within the enzyme's active site play a critical role in catalysis.[15] Using the vibrational Stark effect, they directly measured these intense fields and showed that they are primarily generated by noncovalent interactions, particularly strong hydrogen bonds in the oxyanion hole at the enzyme active site. Their findings emphasized that these pre-organized electrostatic environments are a key driving force behind KSI's remarkable catalytic efficiency. By stabilizing the transition state, the enzyme's electric field effectively lowers the activation energy barrier ($\Delta G^{\ddagger}$). This effect can be quantitatively described by the

interaction energy term $-\boldsymbol{\mu}^{\ddagger}\cdot\boldsymbol{F}$, where $\boldsymbol{\mu}^{\ddagger}$ is the dipole moment of the transition state along the direction of the field (the reaction difference dipole), and $\boldsymbol{F}$ is the electric field. This interaction directly contributes to the observed acceleration of the isomerization reaction by several orders of magnitude. These insights underscore the crucial role of noncovalent interactions in catalysis and provide a quantitative framework for understanding their mechanistic contributions, motivating us to precisely design such unique interactions an quantify them using the molecular-vise approach available in design for the PCN-521 MOF scaffold.

Supplementary Text 2. Vibrational Stark effect

The Stark effect is a fundamental phenomenon in physics where the perturbations to molecular transitions (vibrational, electronic, etc.) are observed in the presence of electric fields.[5] Under this scheme, when molecules encounter electric fields, their vibrational spectra change (frequency shifts and intensity variations), highlighting the complex interactions between electric dipoles within the molecule and the interacting field. This effect, termed the vibrational Stark effect (VSE), observed in vibrational transitions with techniques like infrared and Raman spectroscopy, serves as a potent tool for investigating molecular environments and quantifying subtle alterations in non-covalent interactions within complex systems.[6]

Until now, a linear VSE has been observed in several systems and has been utilized in two primary ways. Firstly, as shifts to the peak vibrational frequency that scale linearly with the field experienced by an oscillator, governed by the following equation:

$$\bar{\nu}_{obs}(\mathrm{F}) = \bar{\nu}_0 - \Delta\vec{\mu} \cdot \vec{F}$$

where the observed frequency shift in an experiment $\bar{\nu}_{obs}$, is equal to a reference frequency ($\bar{\nu}_0$; ideally the gas-phase frequency) and a difference from $\Delta\vec{\mu} \cdot \vec{F}$, which is a dot product of the intrinsic molecular property termed as the Stark tuning rate ($\Delta\vec{\mu}$) and the field on the bond ($\vec{F}$) with the vibration of interest.

The other representation of the linear vibrational Stark effect can be derived from the intensity variation of vibrational spectra, where the transition dipole moment ($\bar{m}$) of the vibrational transition is altered with the field experienced on the oscillator, given by the following relationship,

$$\bar{m}_{obs}(\mathrm{F}) = \bar{m}_0 - \vec{F}.\underline{\mathbf{A}}$$

where $\bar{m}_{obs}$ is the observed transition dipole moment, $\bar{m}_0$ is the transition dipole moment of the vibrational transition in the gas phase or the absence of a field and and the field on the bond ($\vec{F}$) and its product with the tensor corresponding to the transition polarizability.[7,8] $\bar{m}_{obs}$ can be calculated by integrating the peak area of the vibrational transition at a known concentration of the analyte and the path length traversed by the incoming infrared radiation while interacting with the molecule of interest.[9]

Supplementary Text 3. Nitriles as probes for VSE

The first vibrational Stark spectra under an ***externally*** applied electric field were examined for simple nitriles (-C≡N).[8] Since then nitriles, commonly encountered in pharmaceuticals, have been incorporated as probes for quantifying fields with the VSE at different positions within proteins, nucleic acids, biological membrane components, and nonbiological systems. Nitrile infrared (IR) transitions are notably strong and occupy a clear region in the vibrational spectrum (~2200 cm^{-1}), unlike other vibrational probes of interest such as carbonyls (-C=O; ~1600 cm^{-1}). While this VSE has been extensively studied and characterized in different abovementioned condensed environments, this study is the first demonstration of the VSE within porous solids.

In this study, a nitrile vibrational probe installed on the defected linker in the MOF was used for investigating electric fields from protic and aprotic substituents within the MOF scaffold. By introducing nitrile probes through linker modification and ligand substitution of various functional groups in defined proximity to the probe, we achieve the first quantification of electrostatic effects on the vibrational probe inside the MOF.

To utilize the nitrile as a vibrational Stark probe for measuring electric fields in MOFs, a calibration of the nitrile's sensitivity to vibrational frequency shift or intensity (TDM) in response to electric fields is essential. The calibration is based on the linear vibrational Stark effect (VSE), i.e. $\bar{\nu}_{obs}(\mathrm{F}) = \bar{\nu}_0 - \Delta\vec{\mu} \cdot \vec{F}$, where we can estimate the $\bar{\nu}_0$ and $\Delta\vec{\mu}$ by a linear fit of $\bar{\nu}_{obs}$ of the nitrile in different solvents against the electric field projected on the nitrile. Across aprotic solvation environments, redshifts in the nitrile vibrational frequency are observed as solvent polarity increases, a phenomenon termed vibrational solvatochromism.[10]

Supplementary Text 4. Anomalous blue shifts ($\Delta\bar{\upsilon}_{\mathrm{HB}}$) of nitriles in protic environments

When it comes protic environments, interpreting nitrile frequency shifts under traditional linear vibrational Stark effect (VSE) framework presents challenges due to well-documented blueshift effects **($\Delta\bar{\upsilon}_{\mathrm{HB}}$)**.[9] Normally, one would expect a redshift (decrease in frequency) when a molecule forms a H-bond due to the stabilizing fields on the molecular vibration of interest. However, in the case of nitriles, this interaction leads to a blue shift, where the vibrational frequency increases. The quantity $\Delta\bar{\upsilon}_{\mathrm{HB}}$ is thus attributed to the unexpected increase in the vibrational frequency of a nitrile group (C≡N) when it forms a H-bond with a donor, such as water or other protic solvents. This difference in frequency from the expected value from the solvatochromic calibration and the experimentally observed frequency, challenges the conventional understanding of linear VSE for nitriles in protic environments and can be expressed as the following,

$$\Delta\bar{\upsilon}_{\mathrm{HB}} = \bar{\upsilon}_{\mathrm{Obs}} - \bar{\upsilon}_{\mathrm{Exp}}$$

Where $\Delta\bar{\upsilon}_{\mathrm{HB}}$ or the H-bond blue-shift is the difference between the experimentally observed vibrational frequency (ν_{obs}) and the expected frequency (ν_{exp}) from a calibration within the framework of VSE.

This complication undermines the direct quantitative use of nitrile frequency shifts as probes for local electric fields in protic environments. It is noted that transition dipole moment (TDM) values of the nitrile vibrational transition do offer linearity with the field in all environments but require precise measurement of nitrile concentration.[9] In the photoactive yellow protein, the known extinction coefficient of the p-coumaric acid chromophore provided a direct measurement of the nitrile concentration in the condensed phase, and measurements were performed using liquid samples on an FTIR. Therefore, TDM values, in combination with calibrations from AMOEBA field-frequency plots of solvatochromic analysis, faithfully reported the fields in protic environments.[11] This approach is not applicable for solid MOF samples in this study where vibrational signature detection of the nitrile is by Raman scattering. In the MOF, the concentration of the nitrile can only be estimated from digestion NMR, and Raman spectra do not faithfully report linear absorbances, from which vibrational TDMs can be accurately determined.

Despite the complications, geometric descriptors of H-bonding can offer valuable quantitaive electrostatic insights, as discussed in the text.[9,11] Models that describe the $\Delta\bar{\upsilon}_{\mathrm{HB}}$ in terms of the H-bond's geometry, specifically focusing on the distance and angle between the H-bond donor and the nitrile group have been discussed.[9,12] A recent model from Kirsh and Kozuch find multipolar effects and Pauli repulsion, as significant contributors to the $\Delta\bar{\upsilon}_{\mathrm{HB}}$.[13] The core of Kirsh and Kozuch's model focuses on predicting the $\Delta\bar{\upsilon}_{\mathrm{HB}}$ based on the geometry of the H-bond, as described by the following equation:

$$\Delta\bar{\upsilon}_{\mathrm{HB}} = \Delta\bar{\upsilon}_{\mathrm{HB},0}\left[f(d)_{Head-on} + f(d)_{Side-on}\left(cos(\theta - 180)\right)^{m}\right]$$

Where $\Delta\bar{\upsilon}_{\mathrm{HB},0}$is the blueshift at a reference distance d_0, d is the donor-nitrile distance, θ is the hydrogen bond angle, and the functions $f(d)_{Head-on}$ and $f(d)_{Side-on}$ describe how the blueshift varies with distance for different bond orientations, m is a parameter that adjusts the angular dependence of the shift, allowing for the proper modeling of the bond's orientation. Here, DFT calculations on o-tolunitrile (oTN) were used to investigate the electrostatic contributions to the $\Delta\bar{\upsilon}_{\mathrm{HB}}$ by simulating varying electric fields with a point charge model, showing that electrostatic interactions alone could explain the observed frequency shifts. When extended to the study of fluctuating hydrogen bonds in water or alcohols, the model incorporated motional narrowing effects to account for bond dynamics that can modulate the nitrile $\Delta\bar{\upsilon}_{\mathrm{HB}}$ in solution-phase systems. Validation of this approach with experimental data from protein studies, solvents, and MOF data described in this work (AA, CPh and DCPh variants) has shown that the model accurately predicts the blueshift in both rigid and fluctuating hydrogen bonds.

The mathematical framework proposed by Kirsh and Kozuch offers a robust means of understanding nitrile blueshifts, with minimal changes to bond parameters, based on purely electrostatic considerations – where larger blueshifts are quantitatively linked to stronger H-bonds. This framework significantly enhances the utility of nitriles as vibrational probes for studying molecular interactions, providing insights into hydrogen bonding in both solution and solid-state environments.

Supplementary Text 5. Polarized Raman Scattering

From polarized Raman scattering experiments of PCN-521 variants Ph and TFM (Supplementary Figs. 21 and 22), we observed that Raman scattering in these crystals are vertically polarized, regardless of the polarization of the incident light, leading to anomalous $I_{HV} > I_{HH}$. This is due to the strong birefringence exhibited by the MOF crystals, which are in the tetragonal I4/m space group. The fact that the MOF crystals by themselves can polarize light is further evidenced by the image of the crystals observed under a polarization microscope (Supplementary Figure 1). Depolarization ratios in addition to vibrational shifts can be informative to understand noncovalent interactions in this study but is an exercise rendered futile due to strong birefringence of these crystals. The current study therefore continues to focus on utilizing vibrational shifts, which are very sensitive to the electrostatic environment of the nitrile, to investigate the noncovalent interactions of interest.

Supplementary Text 6. Field- Frequency calibration of H_3LCN and TPAN for this study

For this study, we conducted a field-frequency calibration using triphenylacetonitrile (TPAN) as a model compound in aprotic solvents, because H_3LCN is insoluble in many non-polar aprotic solvents. As shown in Supplementary Figure 23, we plotted the frequency shifts against the electric field magnitudes of the solvent, calculated by molecular dynamics simulations using both fixed-charge and polarizable force fields. The consistent linear correlations (fixed-charge force fields gives slope ~0.17 and intercept ~2239.8, shown in Supplementary Figure 23) between H_3LCN and TPAN indicate that the additional benzoic acid moiety in H_3LCN minimally effect's the nitrile's vibrational behavior, thus providing a first pass in validating TPAN as a suitable model for nitrile probe calibration.

Furthermore, we performed *in-silico* Stark calculations as presented in the latter sections (Supplementary Figure 36) and note that under geometrical distortion the Stark tuning rate remains consistent addressing the transferability of this calibration into the MOF framework. This calibration allows for the translation of nitrile vibrational frequencies in MOFs for aprotic field donors into electric field magnitudes, enabling precise field measurements within these structures. By calibrating the nitrile probe's vibrational frequency with electric fields from MD simulations, we could accurately map its vibrational frequency to electric field magnitudes inside MOFs in aprotic environments. In protic environments, the deviation from this calibration provided us with a value for the $\Delta\bar{\upsilon}_{\mathrm{HB}}$.

Supplementary Text 7. Other solvation under nanoconfinement

To expand the scope of guest solvents in the MOF pore, we further examined the solvation effect of water and perfluoropolyether (PFPE) cryo-oil on noncovalent interactions. Both solvents have high boiling points, minimizing solvent evaporation during Raman spectroscopy measurements. The vibrational spectra of the nitrile in TFM and HY variants solvated in water and cryo-oil were examined (Supplementary Figure 37). In cryo-oil, redshifts were observed for both MOFs (-3.5 cm^{-1} for TFM and -3.0 cm^{-1} for HY), indicating a comparable electrostatic stabilization effect of the cryo-oil on the nitrile. In water, both TFM and HY MOFs exhibited small redshifts in the nitrile frequencies (-1.3 cm^{-1} and -2.1 cm^{-1}, respectively). Since hydrogen bonding with water typically leads to blueshifts for nitrile, these redshifts suggest that the water molecules surrounding the nitrile are arranged in a configuration distinct from that in bulk water. This results in large electric fields (redshift due to the Stark effect), yet with only a small H-bond blueshift.

Our results show that while perfluoropolyether (PFPE) cryo-oil stabilizes the nitrile in HY and TFM through electric field interactions, evidenced by redshifts similar to DMSO, the filling of water in the MOF pore unexpectedly caused the nitrile also to shift in the red direction compared to the evacuated MOF. This is in striking contrast to the well-known blue shift of nitrile vibrational frequencies in water (and in H-bonding solvents in general). This suggests that the abnormal arrangement of solvent molecules under MOF nanoconfinement is different from bulk solvent, and this might correlate with the unique properties of porous solids in guest uptake and catalysis.

To further explore the unique solvation under nanoconfinement, molecular dynamics studies to investigate solvent organization within the MOF pores are warranted. Understanding both bulk solvent behavior and unique solvent structuring under MOF confinement is a promising direction for future research.

Supplementary Figures

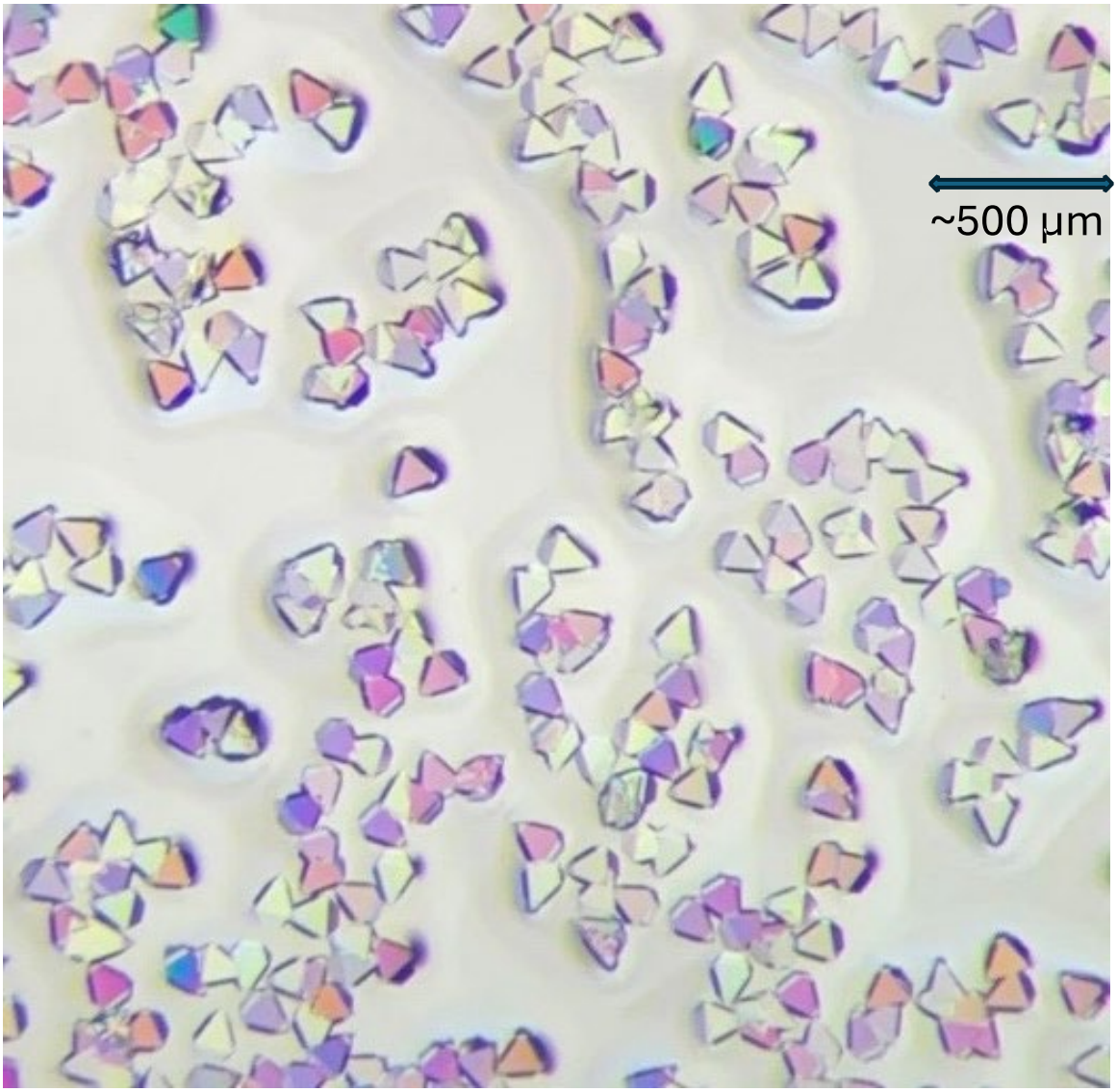

Supplementary Figure 1. Brightfield microscope image of native PCN-521 crystals obtained using cross polarizers. Birefringence is clearly noted across crystals presented in random orientations in the provided field of view.

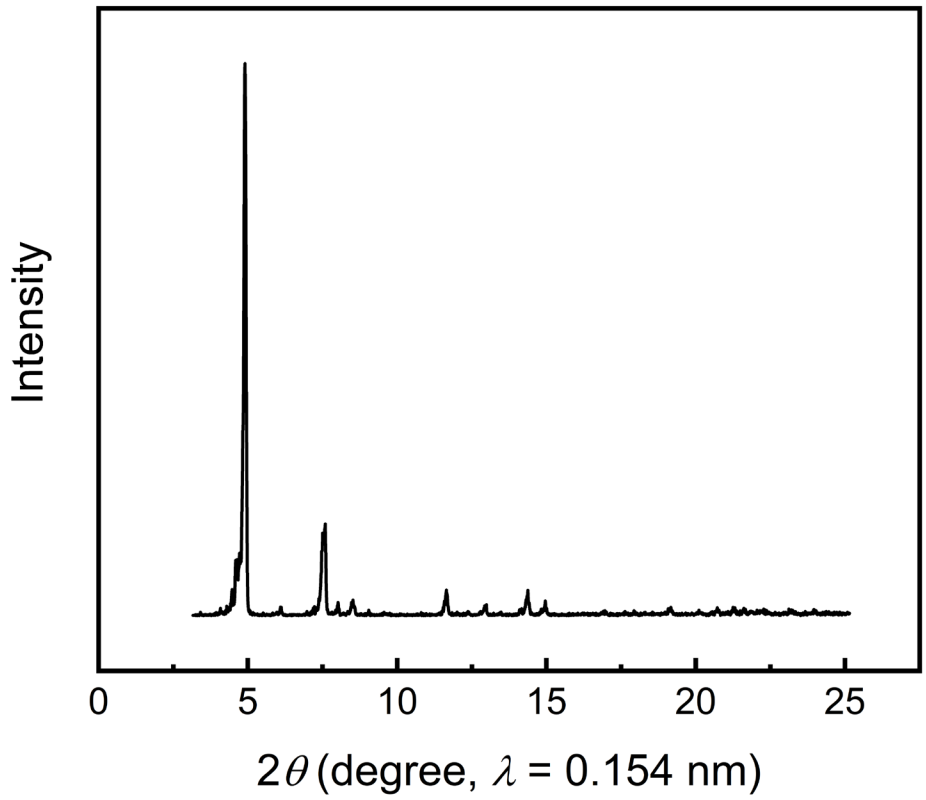

Supplementary Figure 2. PXRD pattern of native PCN-521.

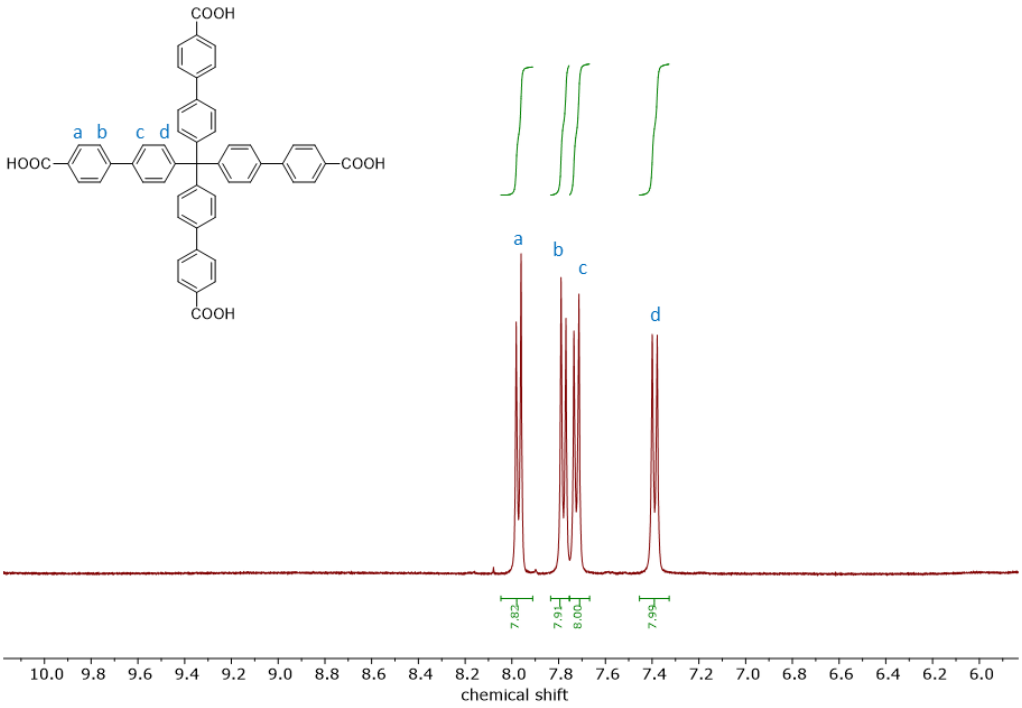

Supplementary Figure 3. ^{1}H NMR spectrum of the digested native PCN-521.

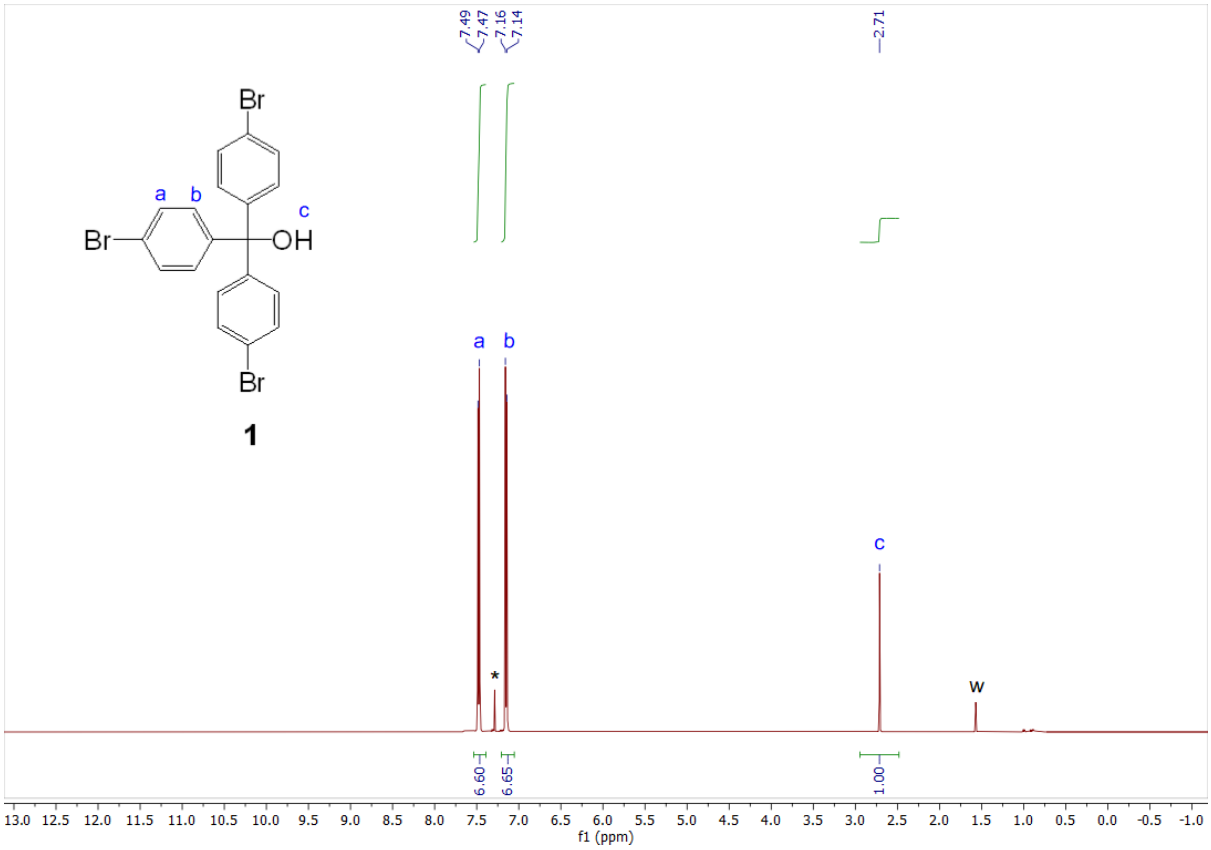

Supplementary Figure 4. ^{1}H NMR spectrum of compound tris(4-bromophenyl) methanol (**1**) in $CDCl_3$. * = residual $CHCl_3$; w = water.

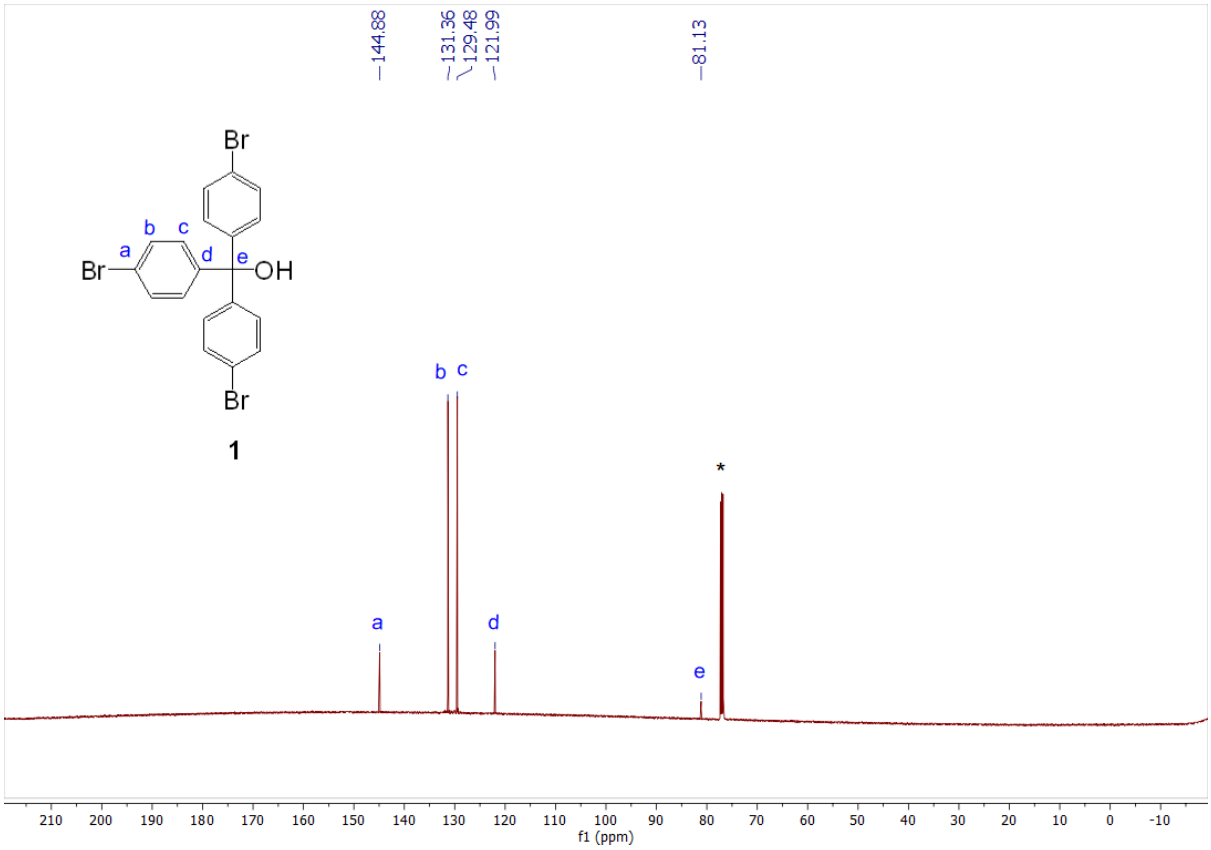

Supplementary Figure 5. ^{13}C NMR spectrum of compound tris(4-bromophenyl) methanol (**1**) in $CDCl_3$. * = $CDCl_3$.

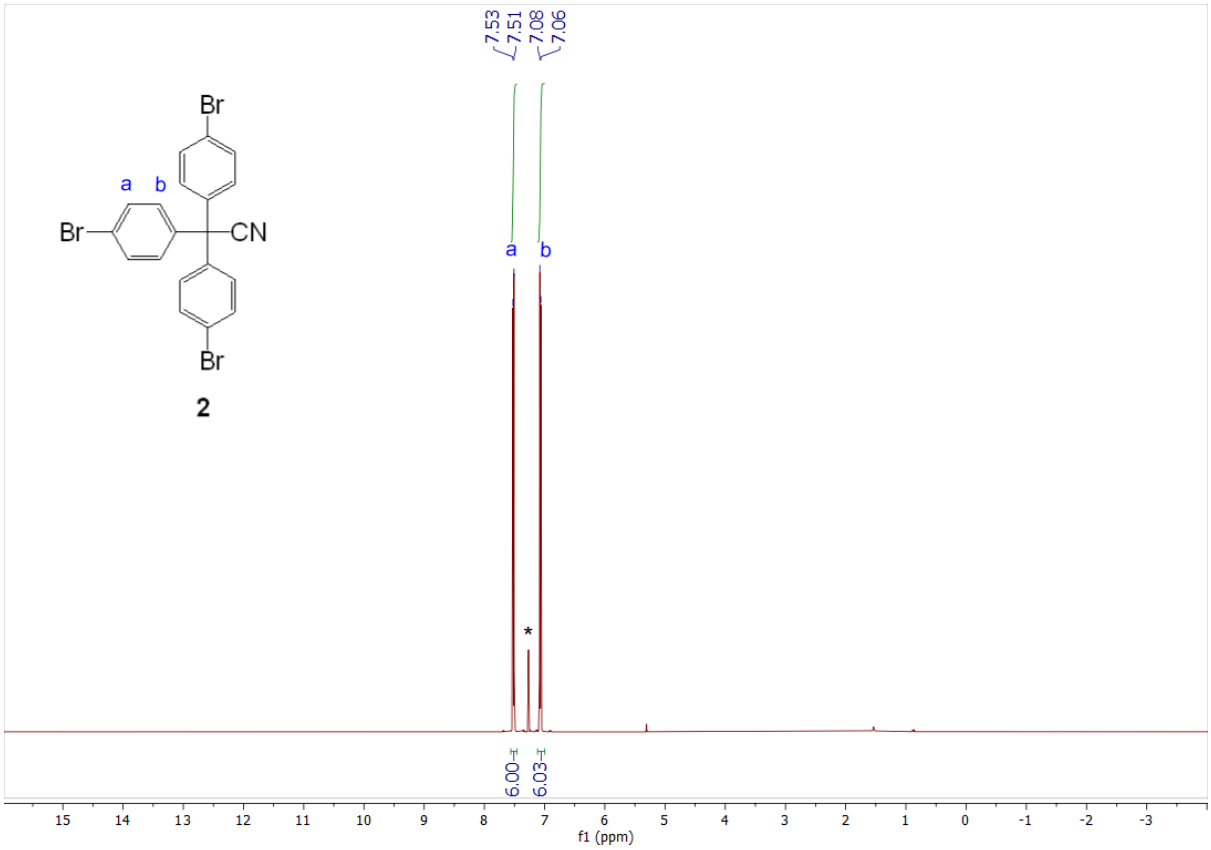

Supplementary Figure 6. ^{1}H NMR spectrum of compound tris(4-bromophenyl) acetonitrile (**2**) in $CDCl_3$. * = residual $CHCl_3$.

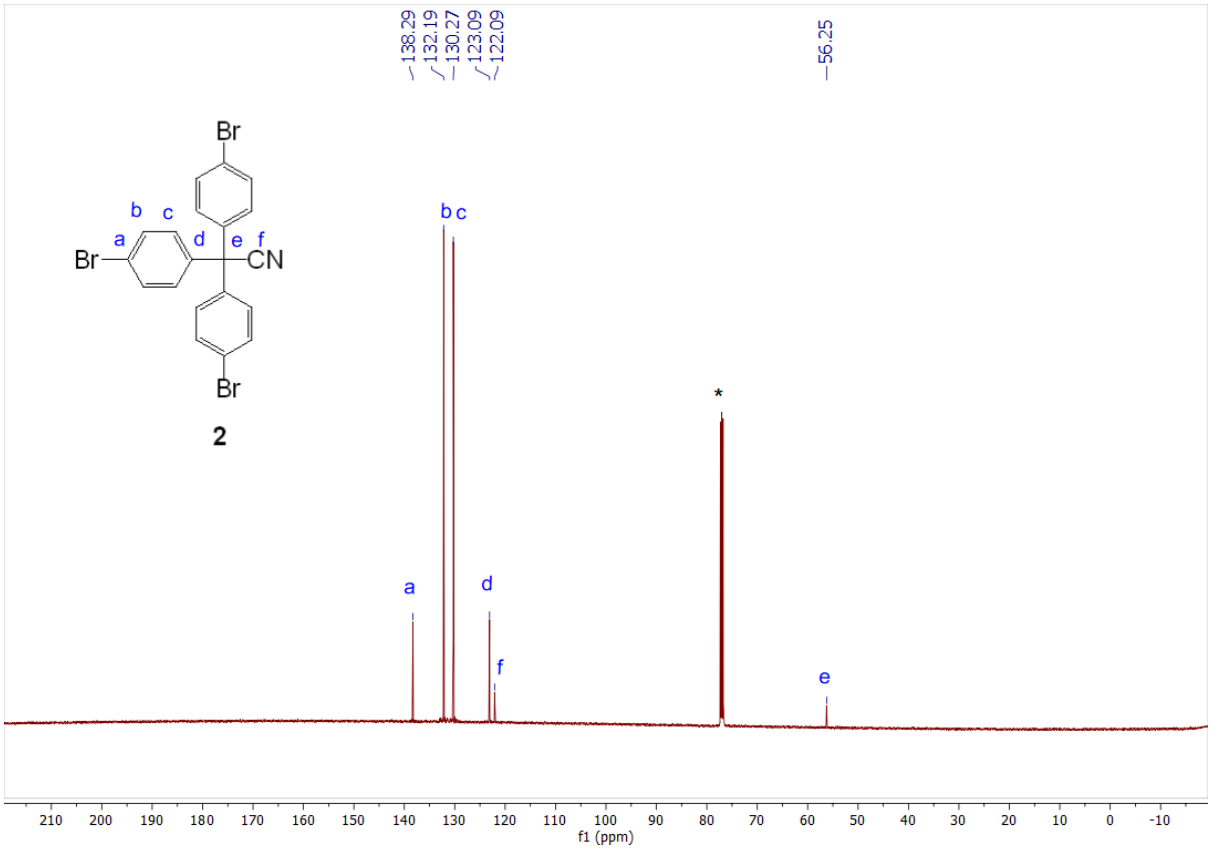

Supplementary Figure 7. ^{13}C NMR spectrum of compound tris(4-bromophenyl) acetonitrile (**2**) in $CDCl_3$. * = $CDCl_3$.

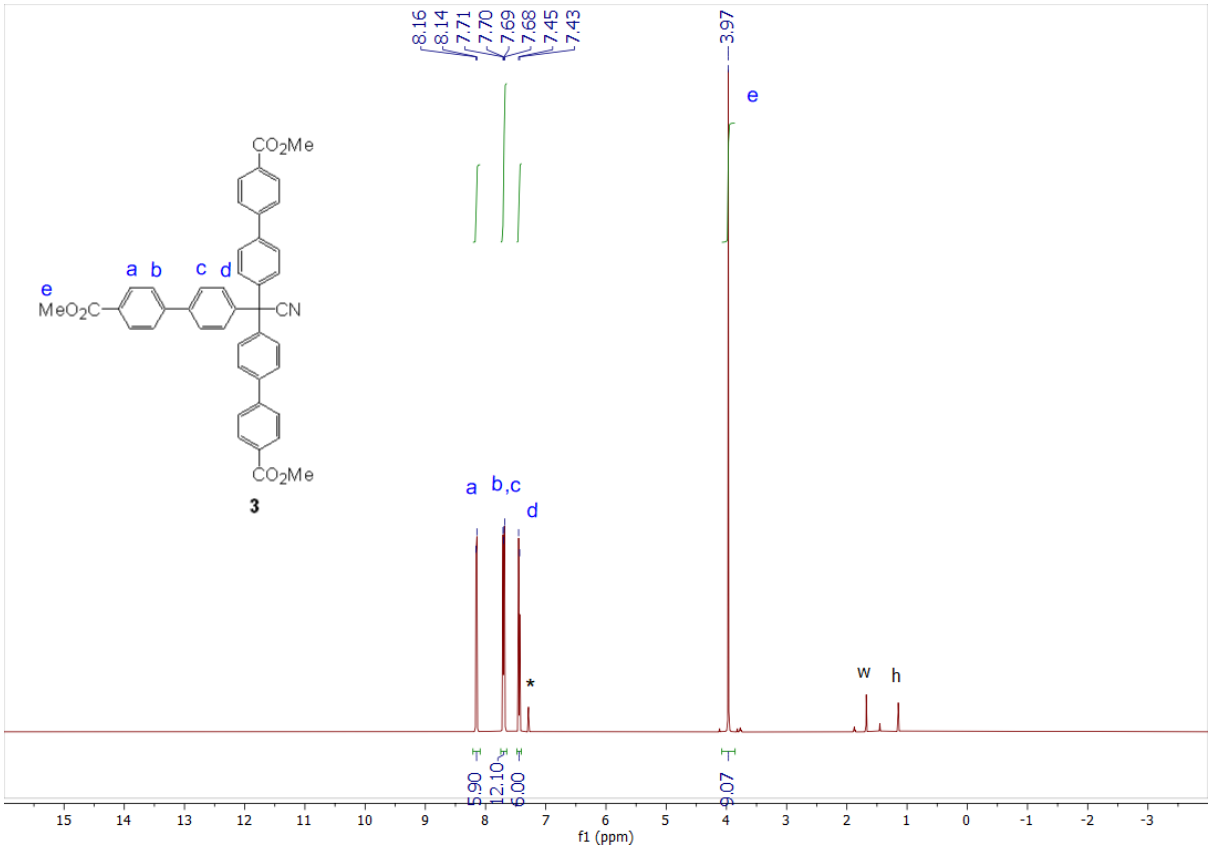

Supplementary Figure 8. ^{1}H NMR spectrum of tris-(4,4',4''-methoxycarbonylbiphenyl)-acetonitrile (**3**) in $CDCl_3$. * = residual $CHCl_3$; w = water; h = H-grease.

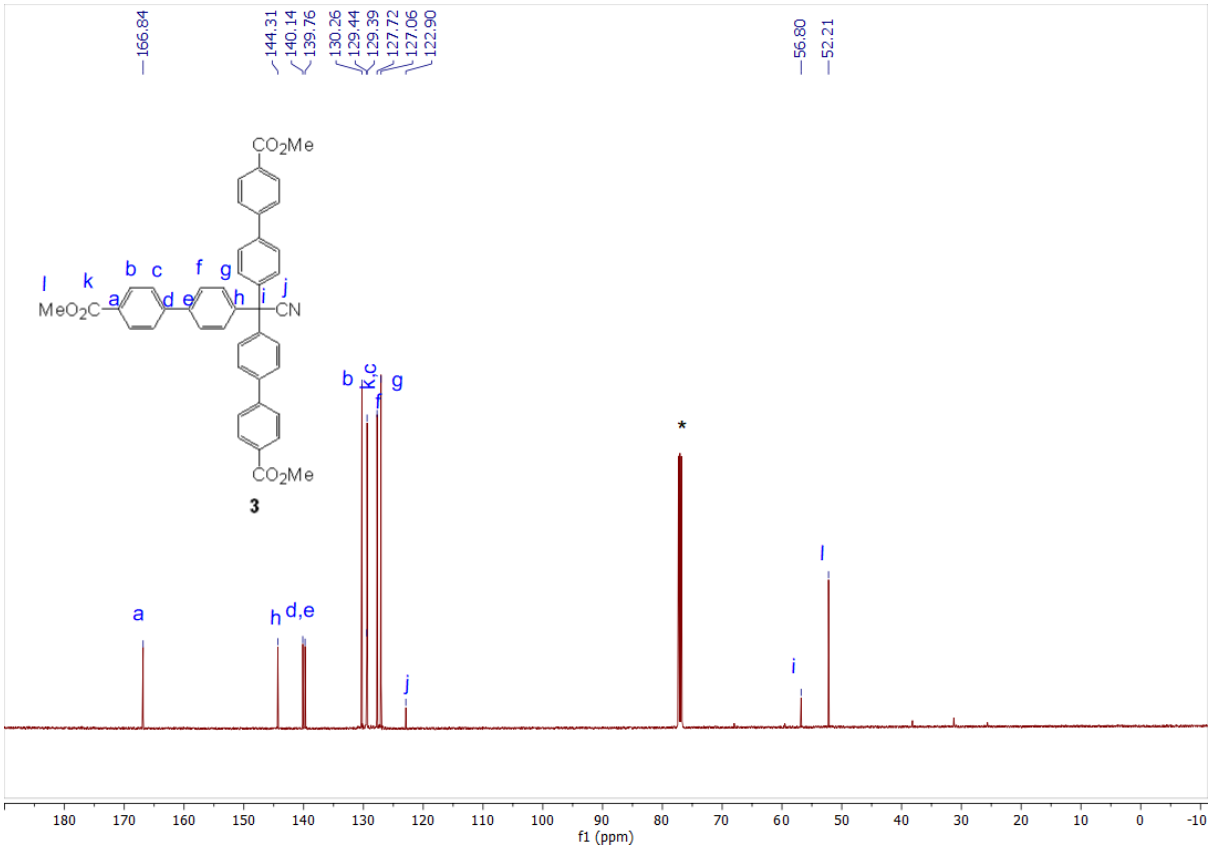

Supplementary Figure 9. ^{13}C NMR spectrum of tris-(4,4',4''-methoxycarbonylbiphenyl)-acetonitrile (**3**) in $CDCl_3$. * = $CDCl_3$.

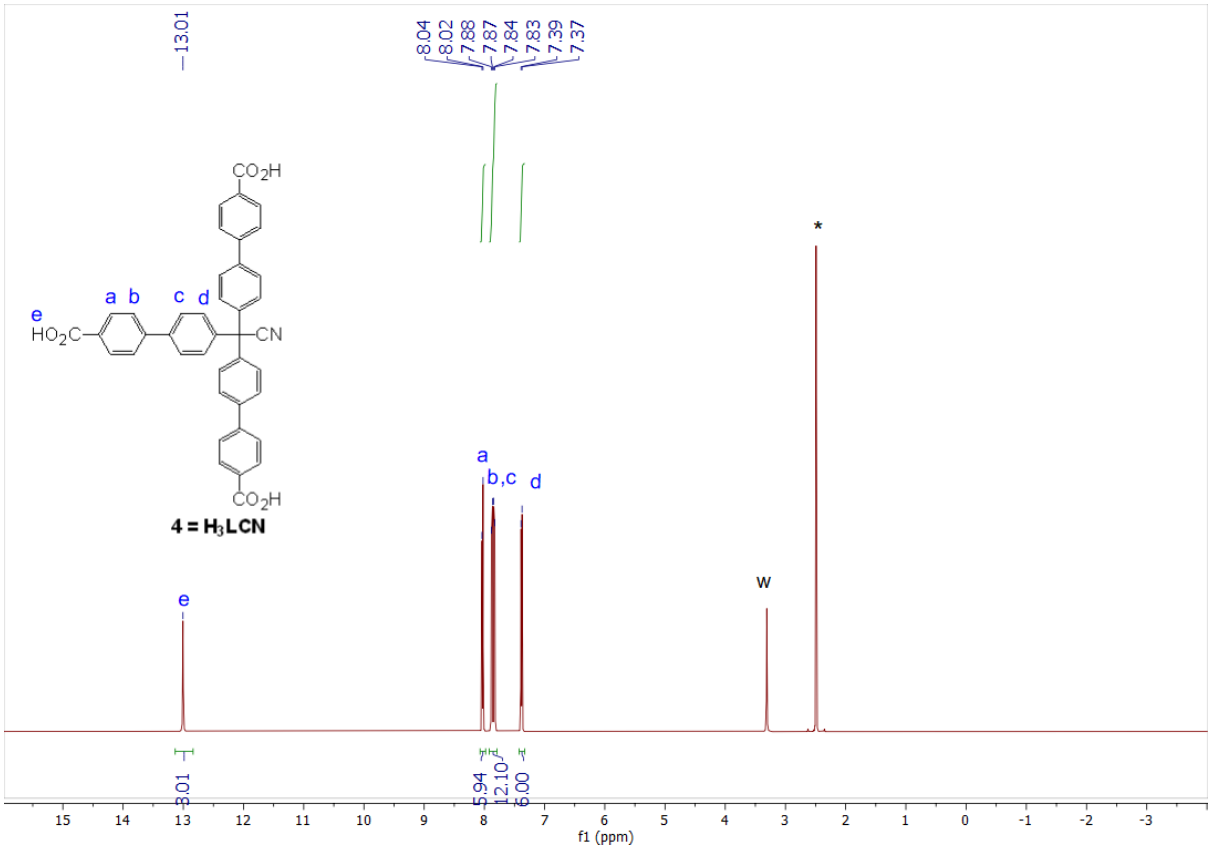

Supplementary Figure 10. ^{1}H NMR spectrum of tris-(4,4',4''-carboxylbiphenyl)-acetonitrile (**4**) in d_6 DMSO. * = residual DMSO; w = water.

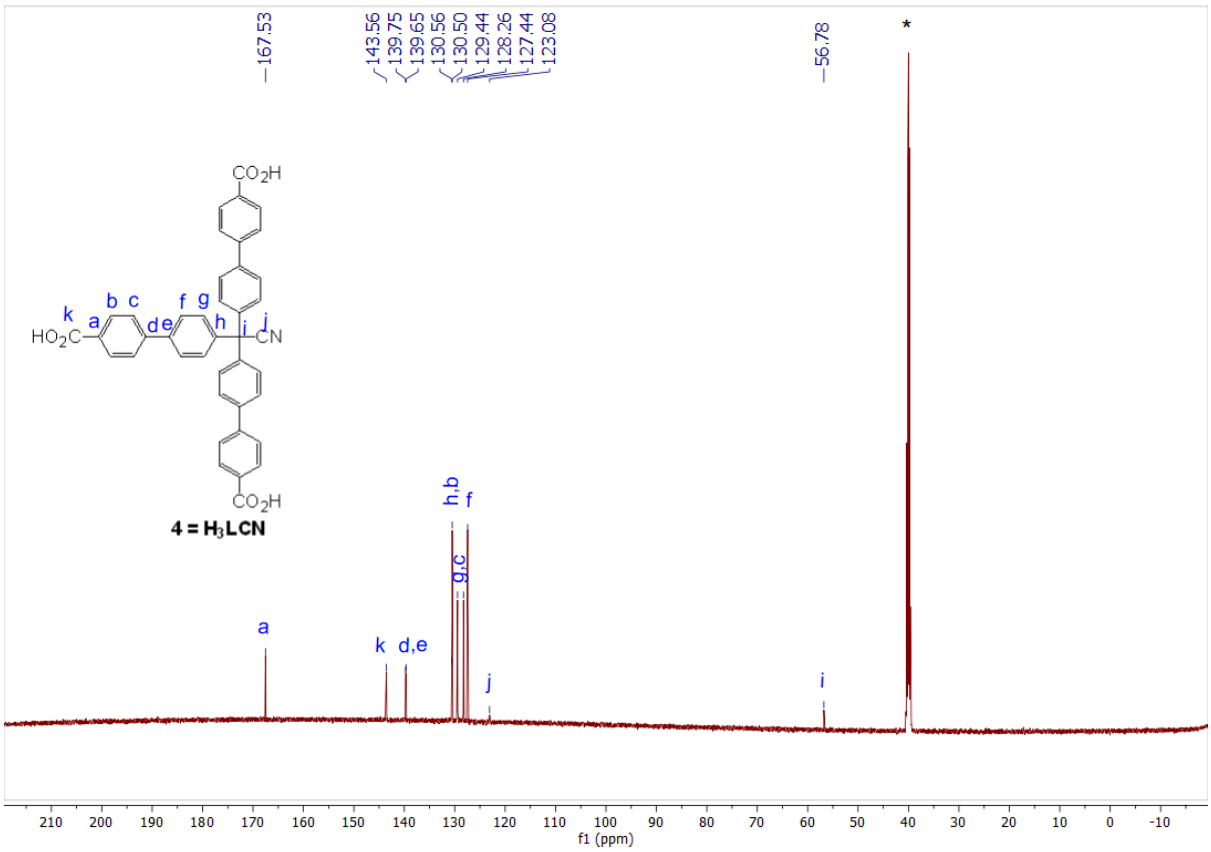

Supplementary Figure 11. ^{13}C NMR spectrum of tris-(4,4',4''-carboxylbiphenyl)-acetonitrile (**4**) in $CDCl_3$. * = $CDCl_3$.

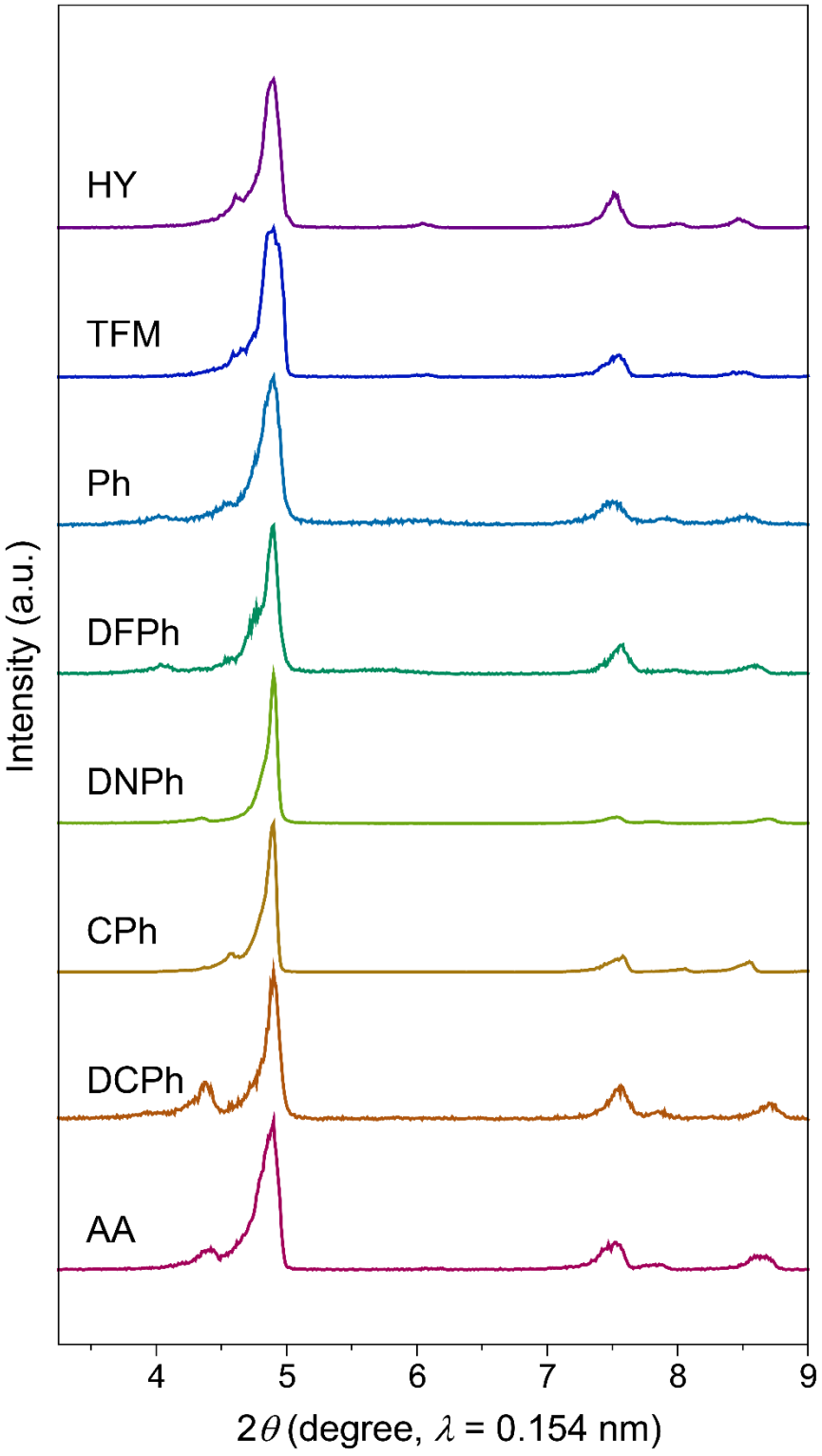

Supplementary Figure 12. PXRD patterns of PCN-521 samples.

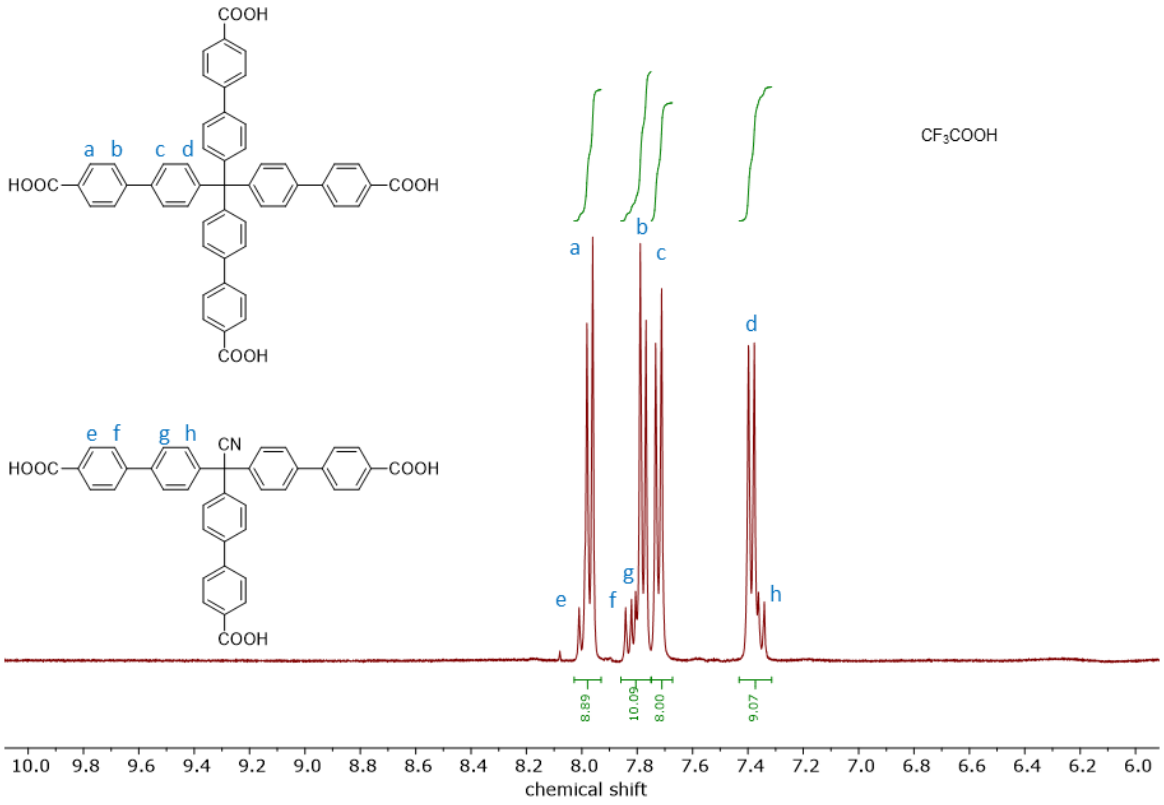

Supplementary Figure 13. ^{1}H NMR spectrum of digested TFM.

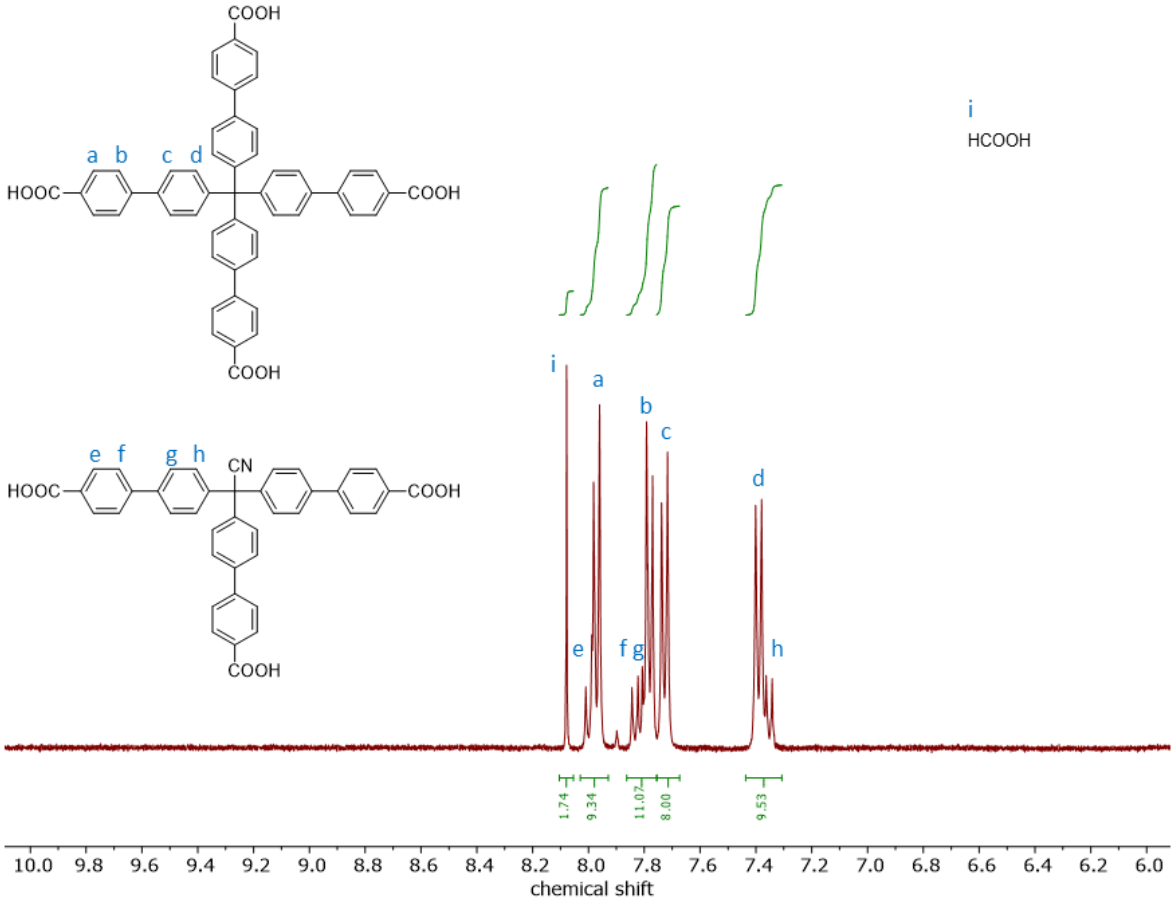

Supplementary Figure 14. ^{1}H NMR spectrum of digested HY. (H_4L : H_3LCN : formic acid = 1 : 0.25 : 1.74)

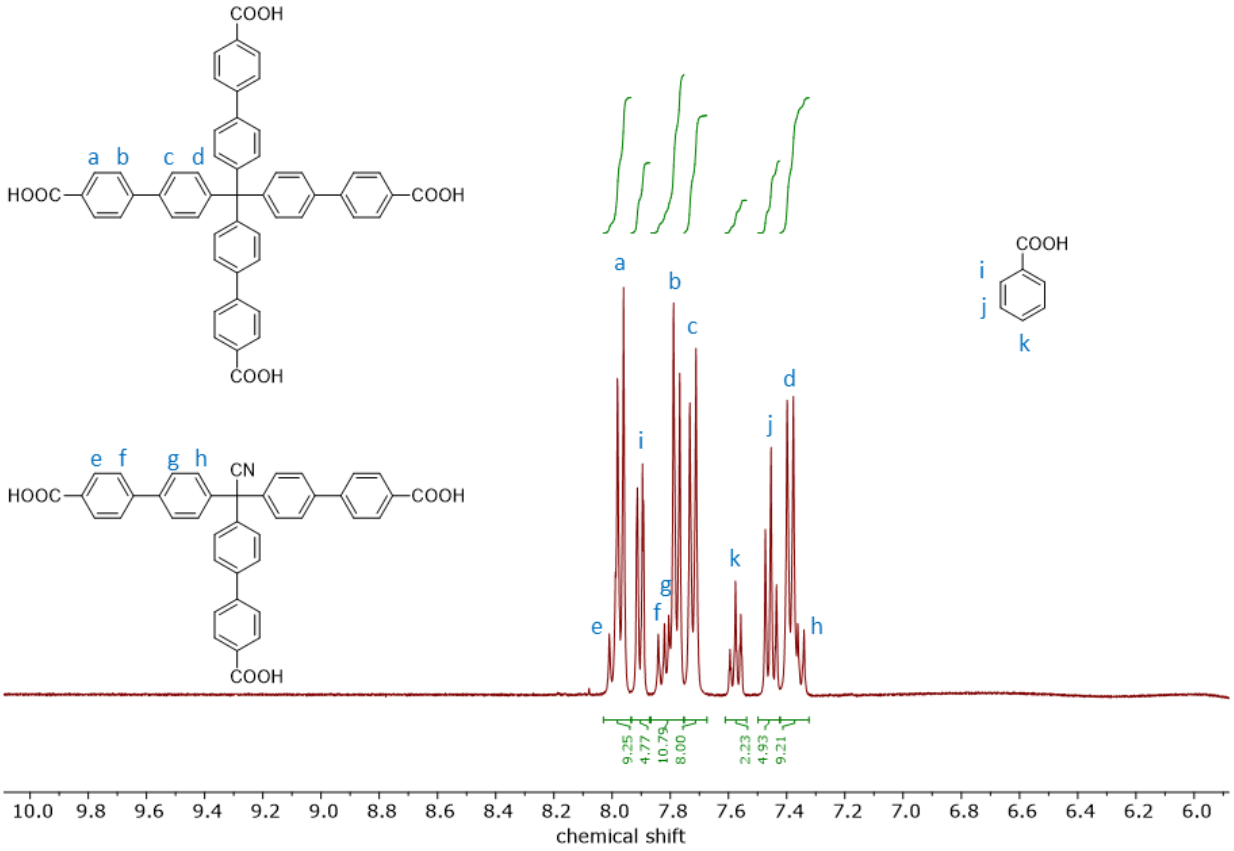

Supplementary Figure 15. ^{1}H NMR spectrum of digested Ph. (H_4L : H_3LCN : benzoic acid = 1 : 0.22 : 2.39)

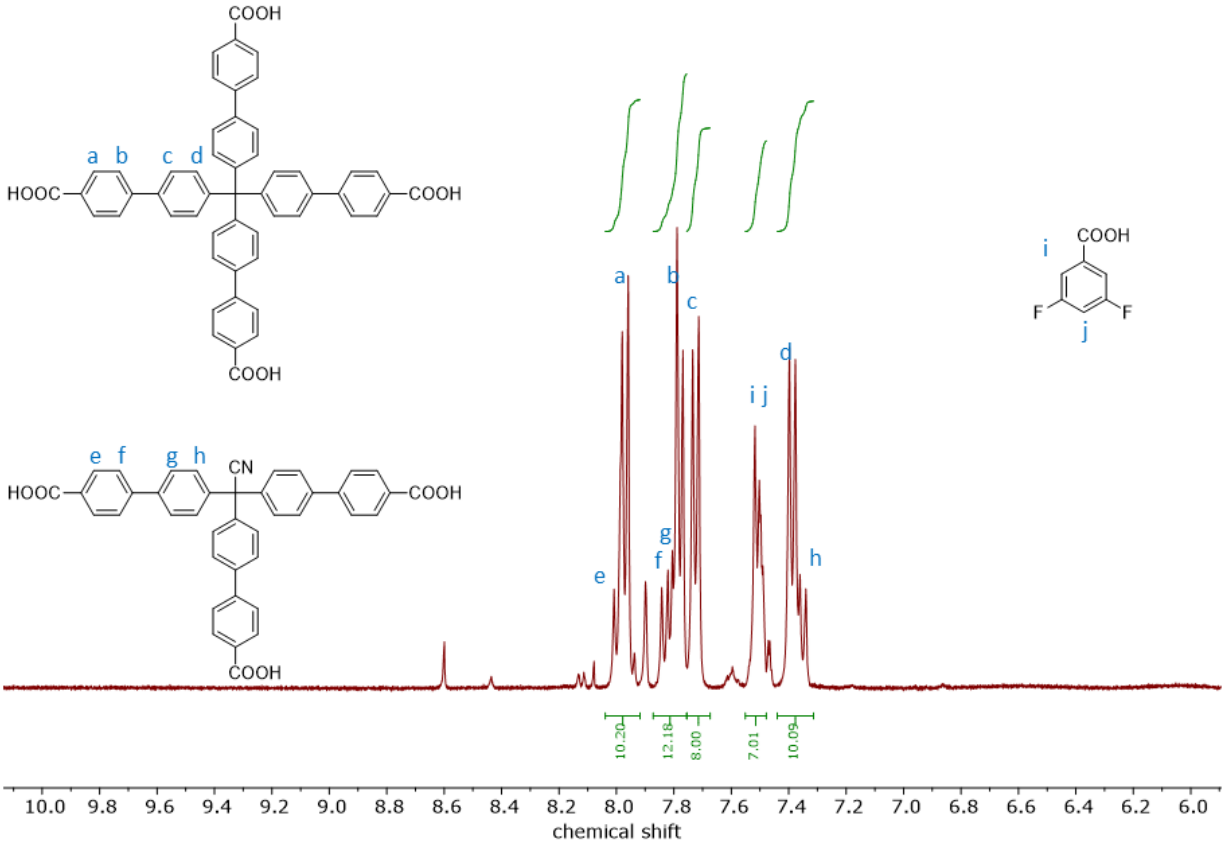

Supplementary Figure 16. ^{1}H NMR spectrum of digested DFPh. (H_4L : H_3LCN : 3,5-difluorobenzoic acid = 1 : 0.35 : 2.34)

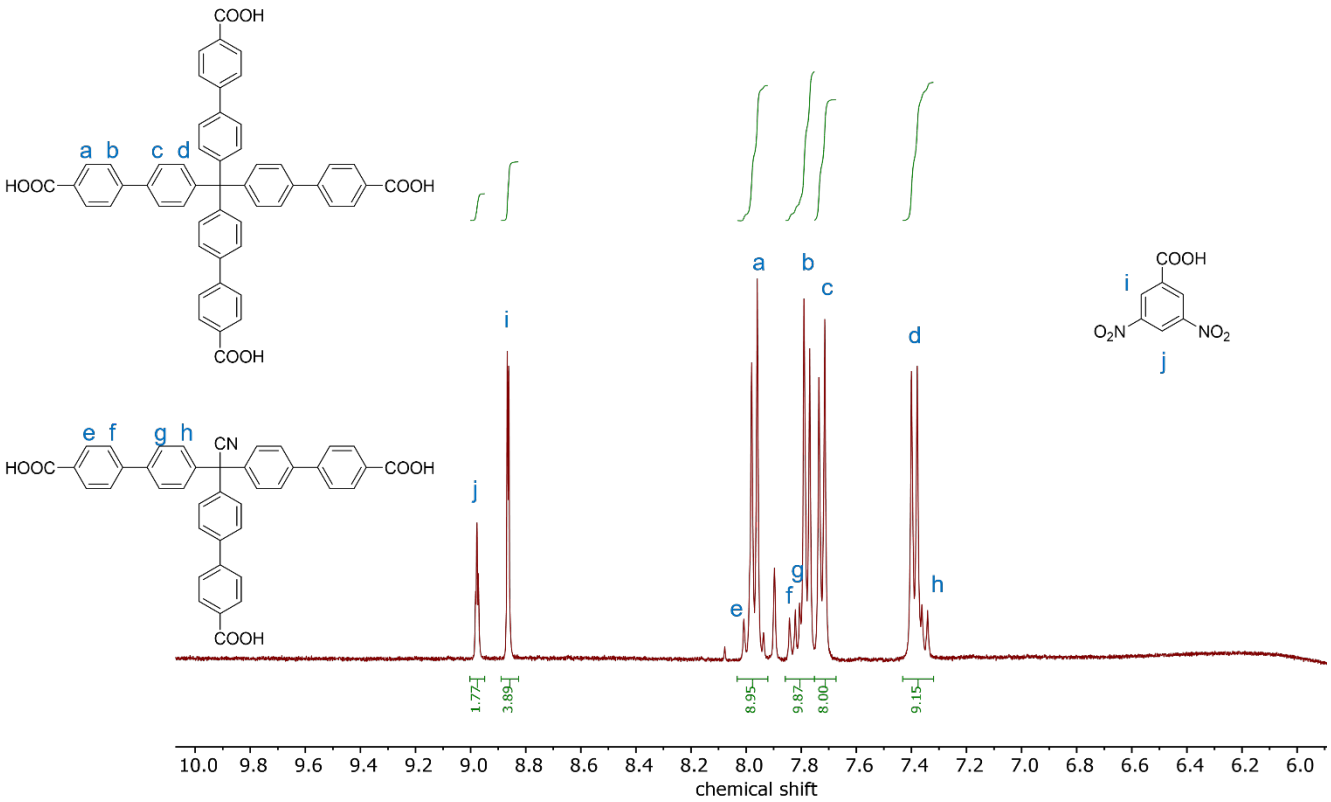

Supplementary Figure 17. ^{1}H NMR spectrum of digested DNPh. (H_4L : H_3LCN : 3,5-dinitrobenzoic acid = 1 : 0.17 : 1.89)

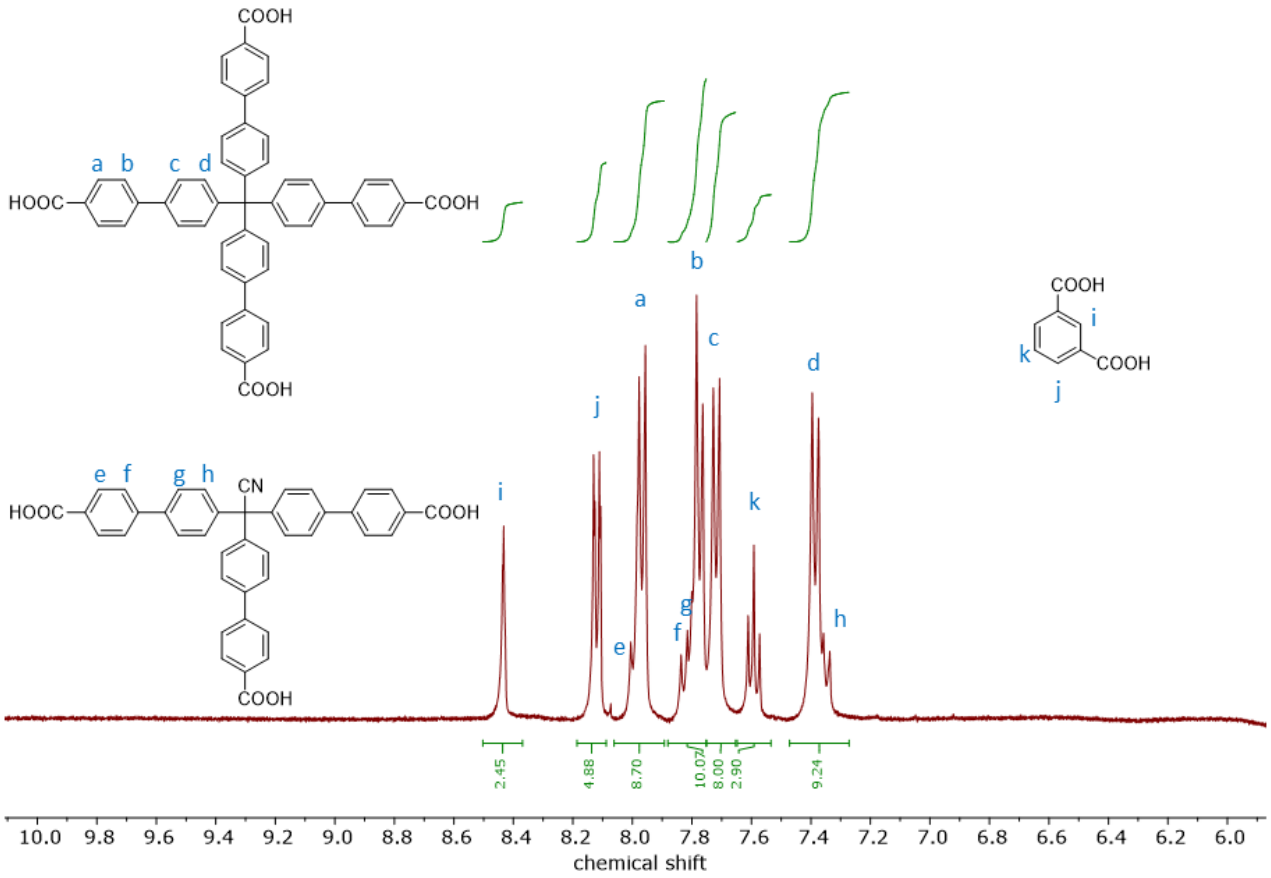

Supplementary Figure 18. ^{1}H NMR spectrum of digested CPh. (H_4L : H_3LCN : isophthalic acid = 1 : 0.17 : 2.56)

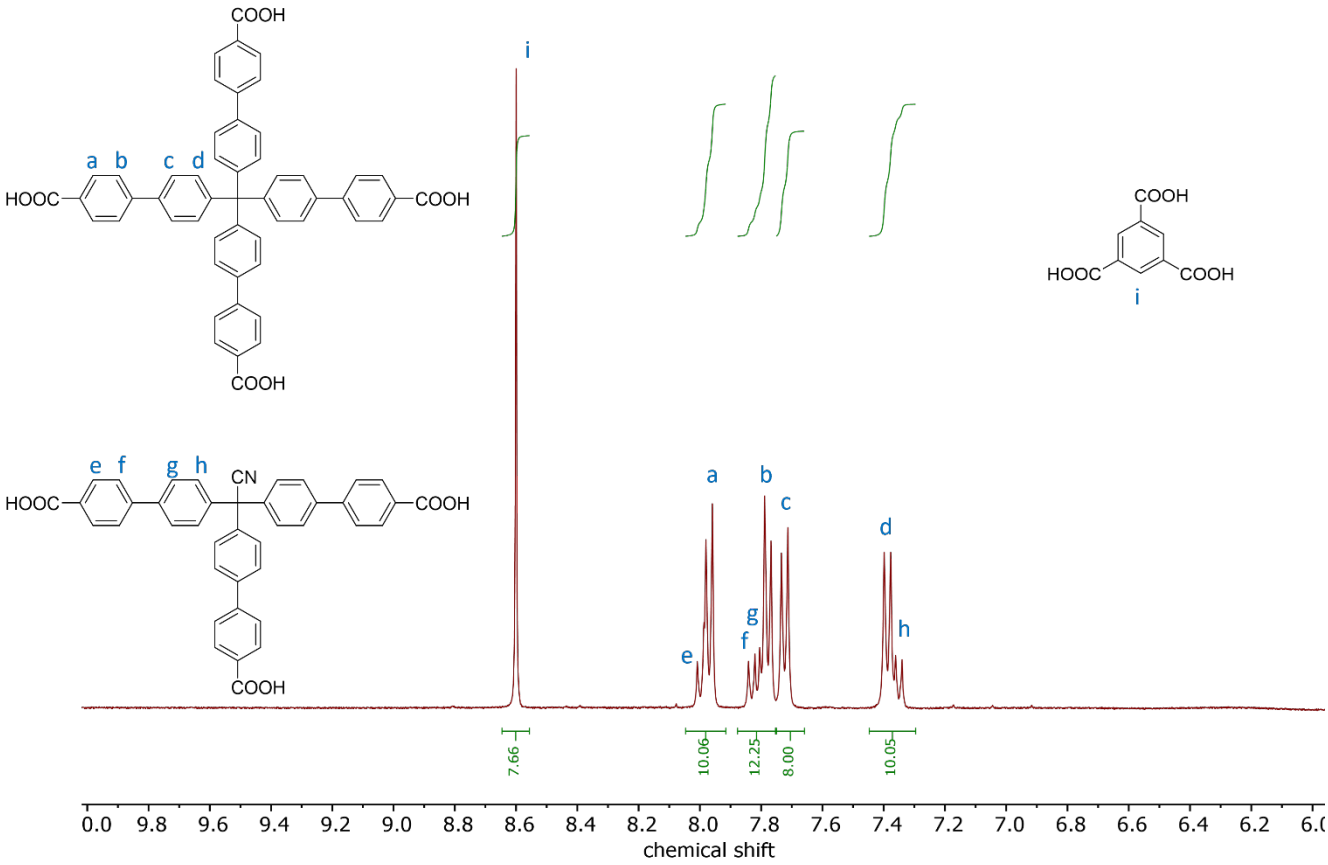

Supplementary Figure 19. ^{1}H NMR spectrum of digested DCPh. (H_4L : H_3LCN : trimesic acid = 1 : 0.35 : 2.55)

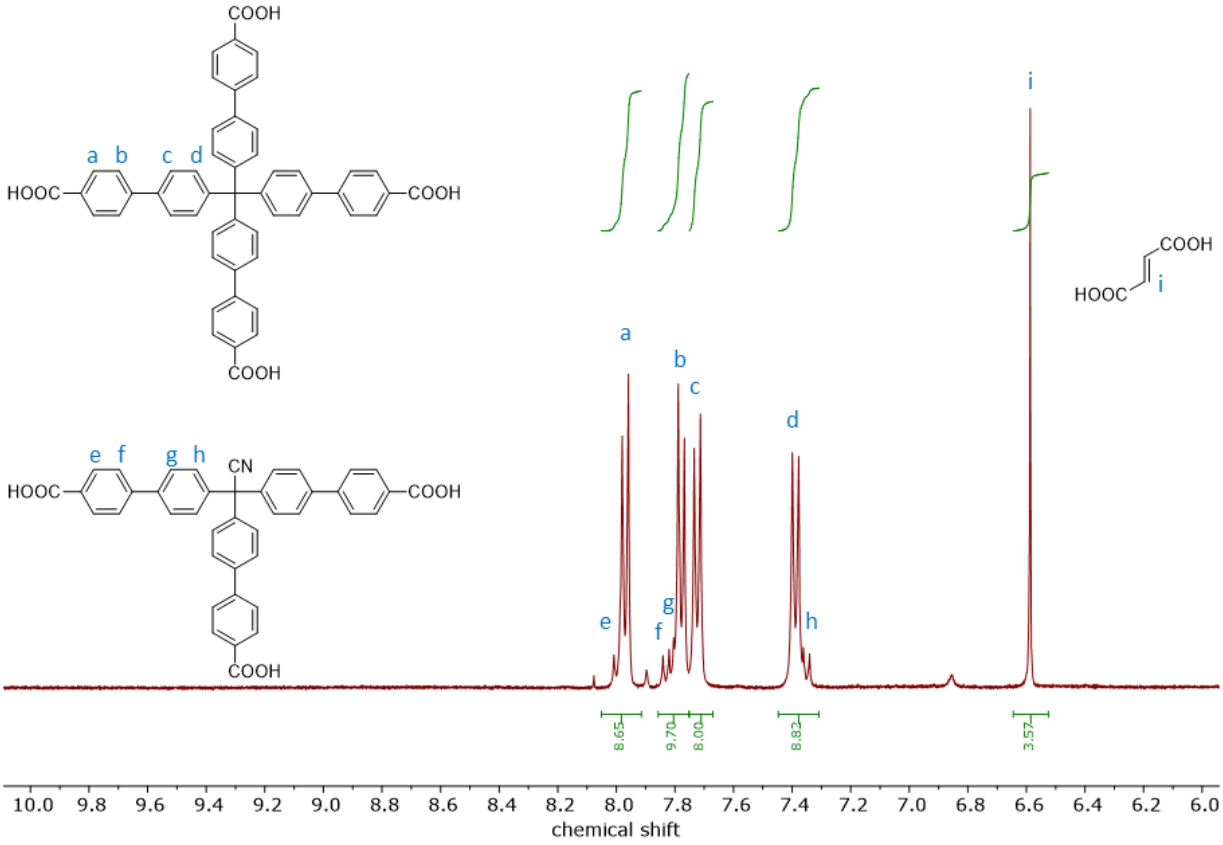

Supplementary Figure 20. ^{1}H NMR spectrum of digested AA. (H_4L : H_3LCN : fumaric acid = 1 : 0.13 : 1.78)

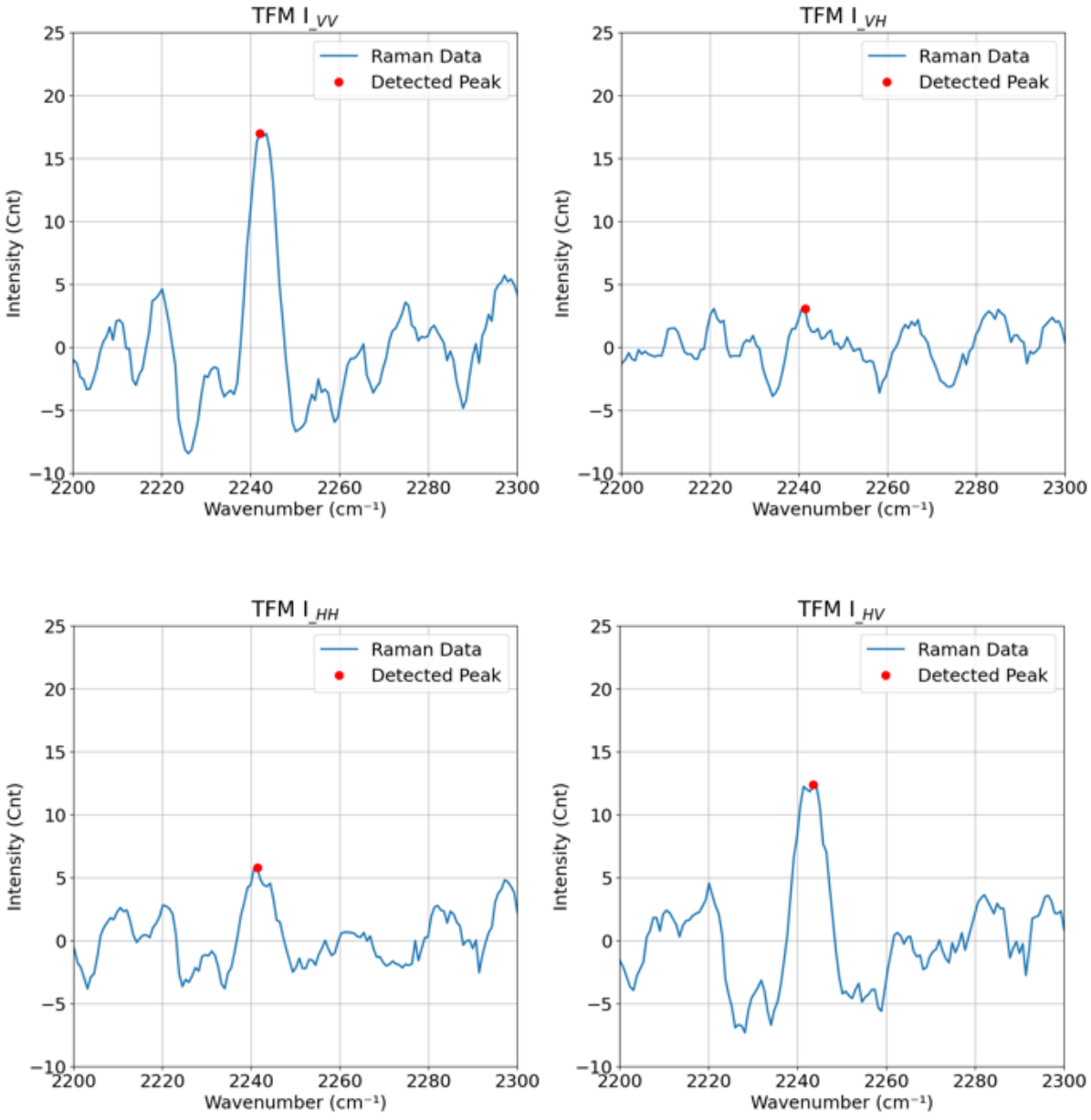

Supplementary Figure 21. Polarized Raman Scattering: Nitrile stretch of the TFM variant of PCN-521 in parallel and perpendicular polarization configurations. Raman scattering from PCN-521 is vertically polarized, regardless of incident polarization.

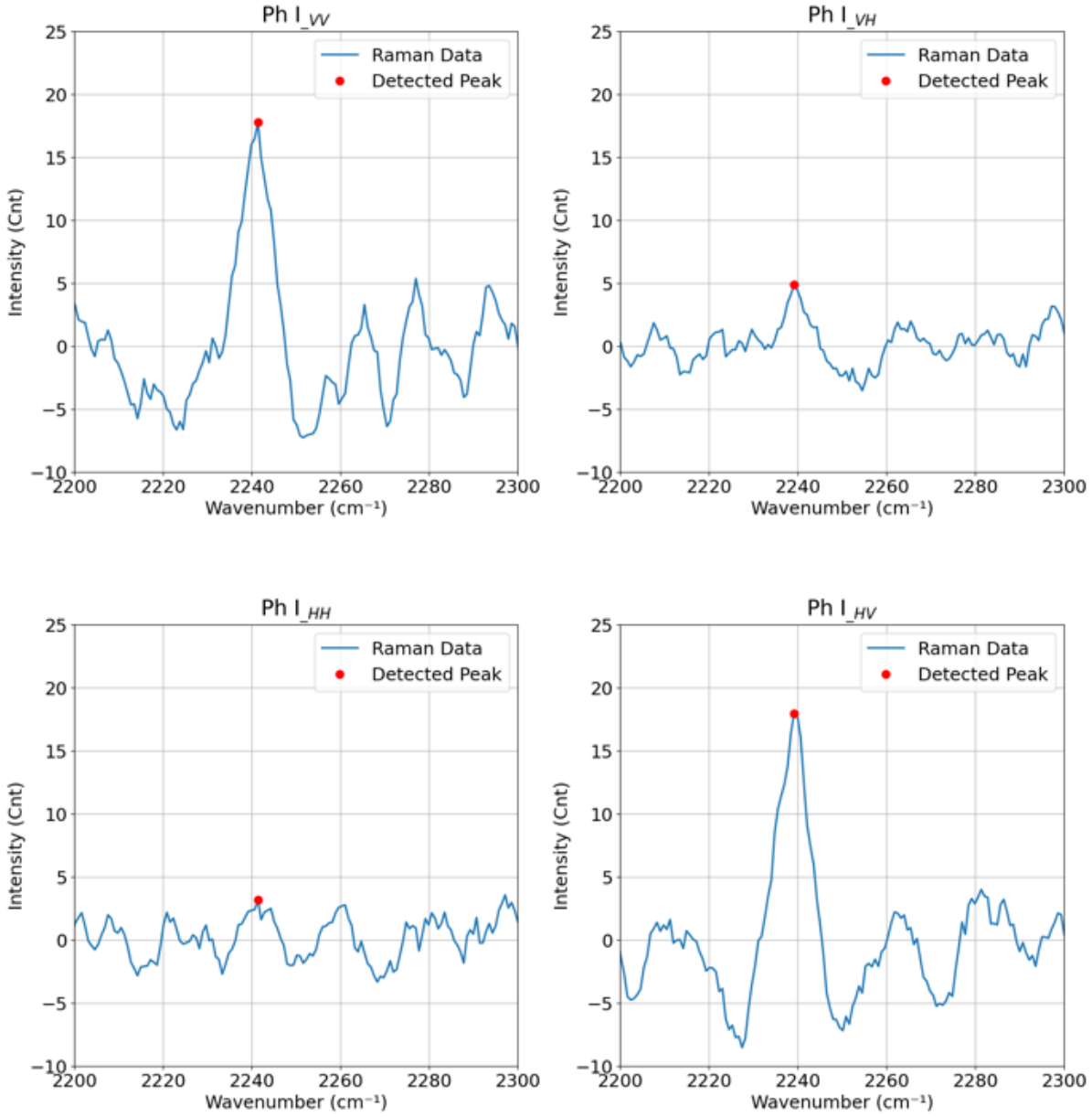

Supplementary Figure 22. Polarized Raman Scattering: Nitrile stretch of the Ph variant of PCN-521 in parallel and perpendicular polarization configurations. Raman scattering from PCN-521 is vertically polarized, regardless of incident polarization.

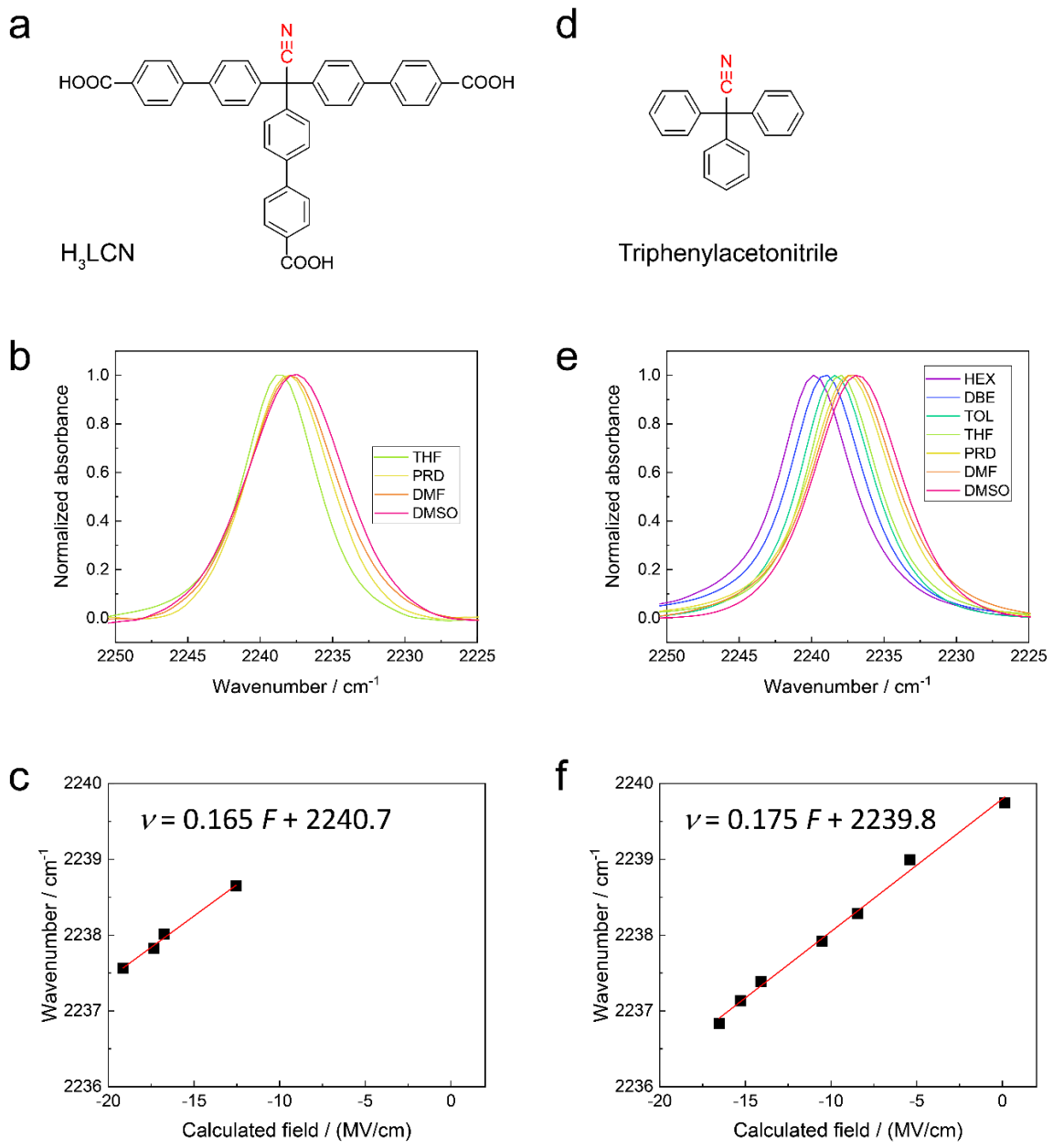

Supplementary Figure 23. Calibration of the vibrational Stark probe in aprotic solvents with GAFF (AMBER) fields. (a) Structure of H_3LCN. (b) FTIR absorbance spectra of H_3LCN in aprotic solvents of varying polarity. (c) Infrared frequencies of the nitrile in H_3LCN were plotted against the calculated mean electric fields based on MD simulations with fixed-charge GAFF (AMBER) forcefields. (d) Structure of the model compound triphenylacetonitrile (TPAN). (e) FTIR absorbance spectra of TPAN in solvents of varying polarity. (f) Infrared frequencies of the nitrile in TPAN were plotted against the calculated mean electric fields based on MD simulations with fixed-charge GAFF (AMBER) forcefields.

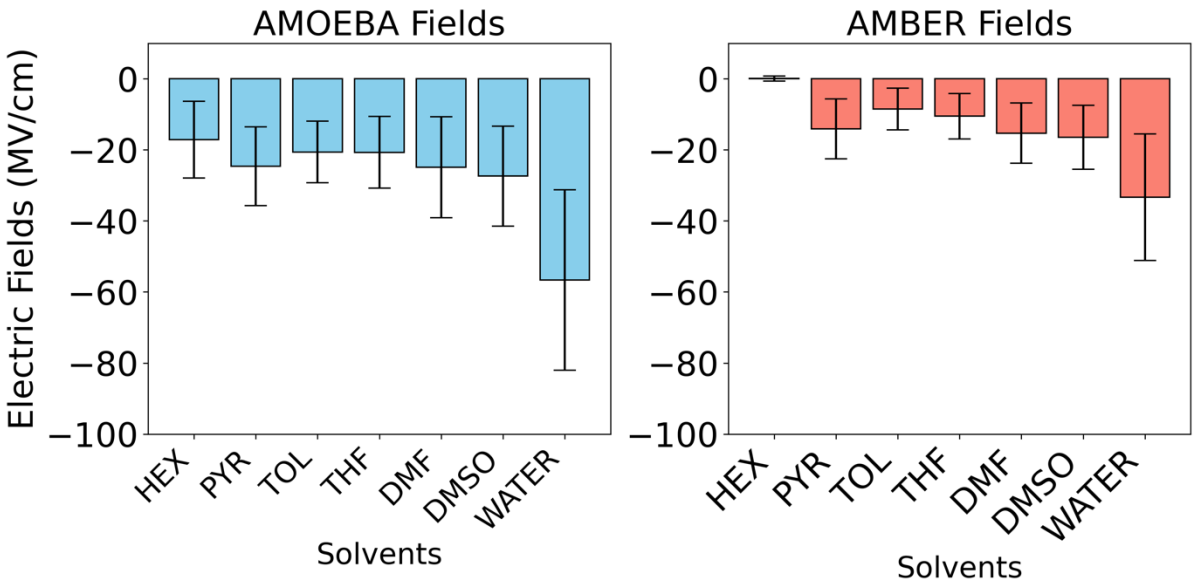

Supplementary Figure 24. Histograms comparing fields obtained for TPAN using polarizable AMOEBA and fixed-charge GAFF (AMBER) force fields. For AMBER fields, the statistics are based on 20,000 total frames from 4 independent MD runs, each run with 5,000 frames (Supplementary Data). The reported average and standard deviation are derived from the 20,000 total frames. For AMOEBA fields, the statistics are based on 2,100 total frames for 3 independent runs (hexane), 4,014 total frames from 4 independent runs (toluene), 3,014 total frames from 3 independent runs (THF), 2,995 total frames from 3 independent runs (pyridine), 3,968 total frames from 3 independent runs (DMF), 3,000 total frames from 3 independent runs (DMSO), and 3,000 total frames from 3 independent runs (water), respectively (Supplementary Data). The fields calculated from each independent run were fitted to a Gaussian function to obtain the mean and the standard deviation, which are then averaged between the runs and reported here. Cartesian coordinates and parameters of MD simulation can be found in Supplementary Information -> Cartesian coordinates and parameters of MD simulation.zip -> AMBER_H3LCN.gro, AMBER_H3LCN.top, AMBER_TPAN.gro, AMBER_TPAN.top, AMOEBA_TPAN.key, and AMOEBA_TPAN.xyz.

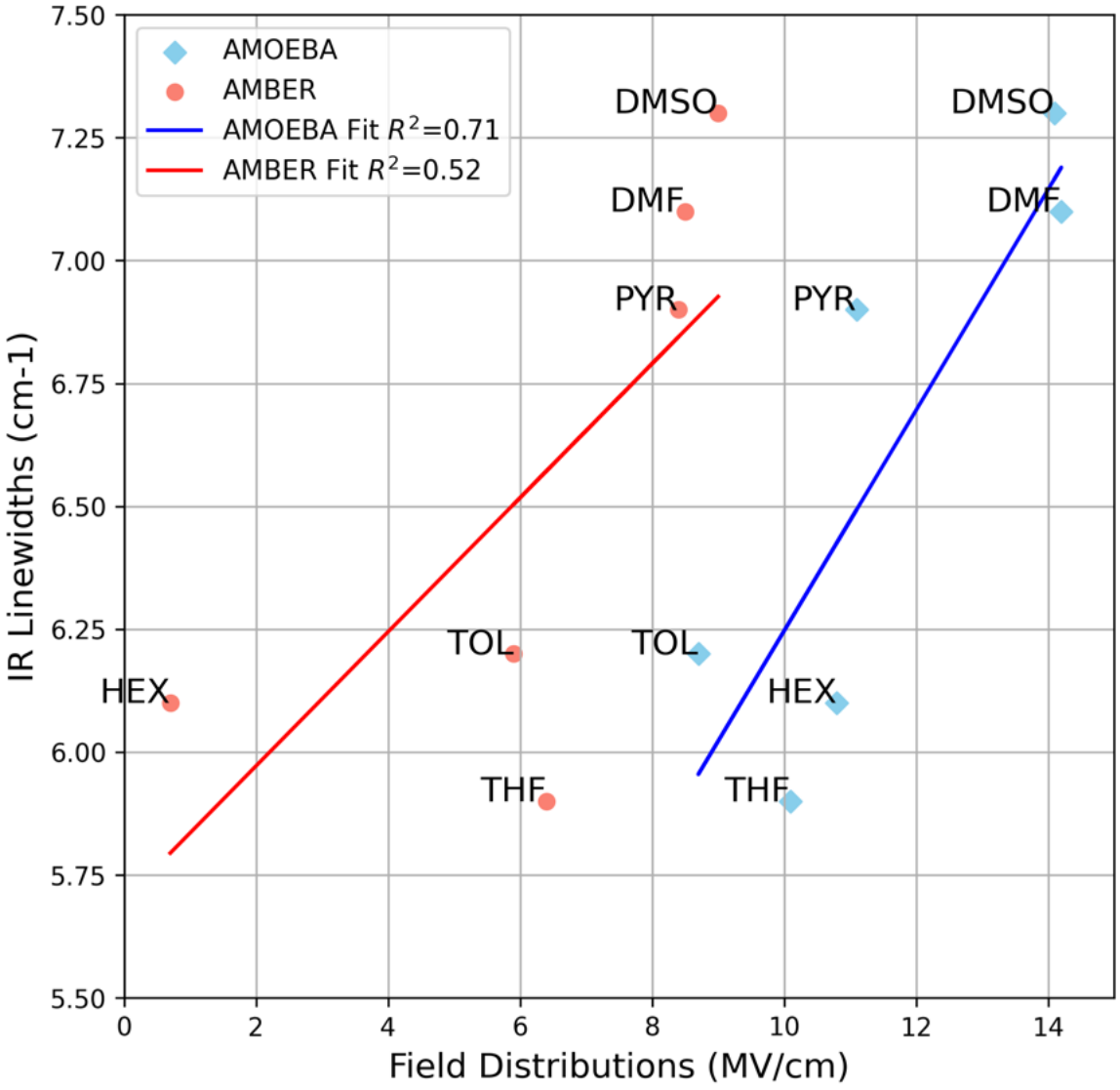

Supplementary Figure 25. Comparison of fields distributions obtained for TPAN using polarizable AMOEBA and fixed-charge GAFF (AMBER) force fields versus the IR linewidths observed in experiments. AMOEBA shows a better linear correlation between the field distributions and the observed IR linewidths indicating a better recapitulation of field distributions from MD simulations when mapped with inhomogeneous broadening of the nitrile peaks in the experiment.

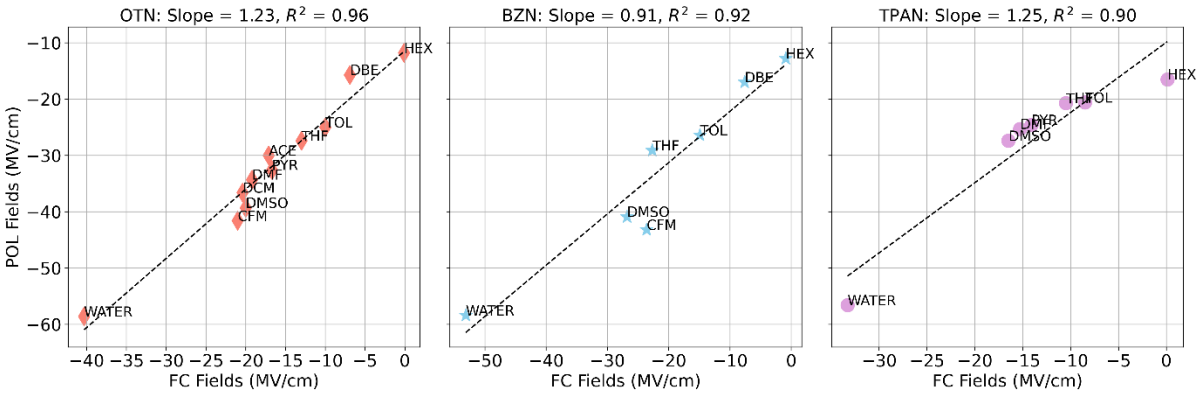

Supplementary Figure 26. Field vs. Field plots were obtained for o-Tolunitrile (OTN)[9], Benzonitrile (BZN)[9], and TPAN using polarizable AMOEBA (denoted POL) and fixed-charge GAFF (denoted FC) force fields. Linear correlations are observed between fields obtained from GAFF and AMOEBA, although higher fields are noted from AMOEBA. This is due to the inclusion of the multipole expansion in AMOEBA, which results in fields that are either nearly equal to or higher than those observed in GAFF simulations. For oTN and TPAN, AMOEBA fields lead to almost a 1.2-fold higher field than GAFF.

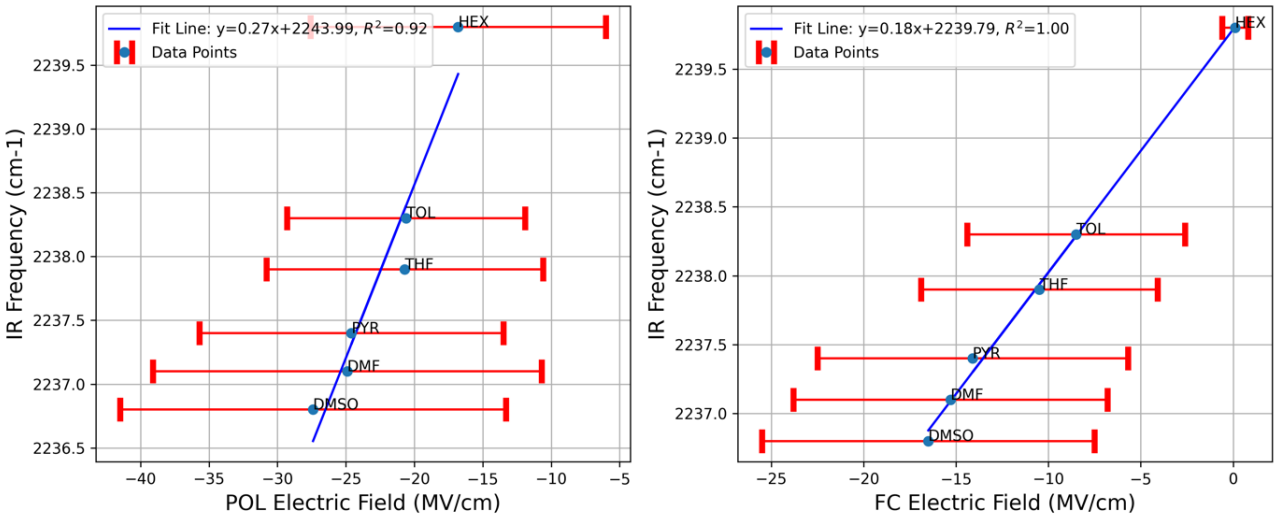

Supplementary Figure 27. Obtaining Stark tuning rates for TPAN using AMOEBA (POL) and GAFF (FC) forcefields using field – IR peak frequency linear correlation. The obtained fits for AMOEBA and GAFF are $\bar{\upsilon} = 0.28(\pm 0.04)\boldsymbol{F_{POL}} + 2244(\pm 1)$ and $\bar{\upsilon} = 0.18(\pm 0.01)\boldsymbol{F_{FC}} + 2240$ with R^2 values of 1 and 0.9 respectively. For the POL and FC electric fields, the statistics and the original data are the same as those used for Supplementary Figure 24.

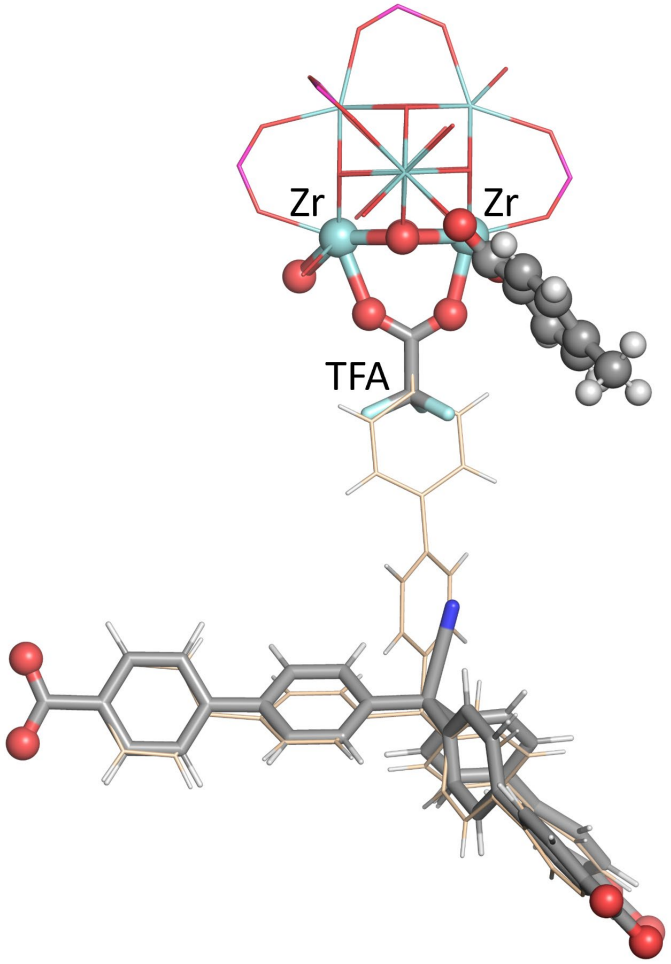

Supplementary Figure 28. Energy-minimized molecular cluster model (B3LYP with 6-31G(d) basis set for C, H, O and N atoms and LANL2DZ effective core potential for Zr) of the TFM-substituted system overlaid with the structure of PCN-521. The crystallographic structure of PCN-521 is depicted as brown lines, while the molecular model is represented by grey sticks and spheres. Spheres denote atoms held fixed to the crystallographic coordinates, whereas sticks represent atoms subjected to optimization. Noticeable geometric differences emerge when the strain imposed by the biphenyl group is removed, clearly indicating that the incorporation of a defective linker releases some extent of strain experienced by H_4L. Cartesian coordinates of the optimized structures can be found in Supplementary Information -> Cartesian coordinates of DFT calculation.zip -> TFM.txt.

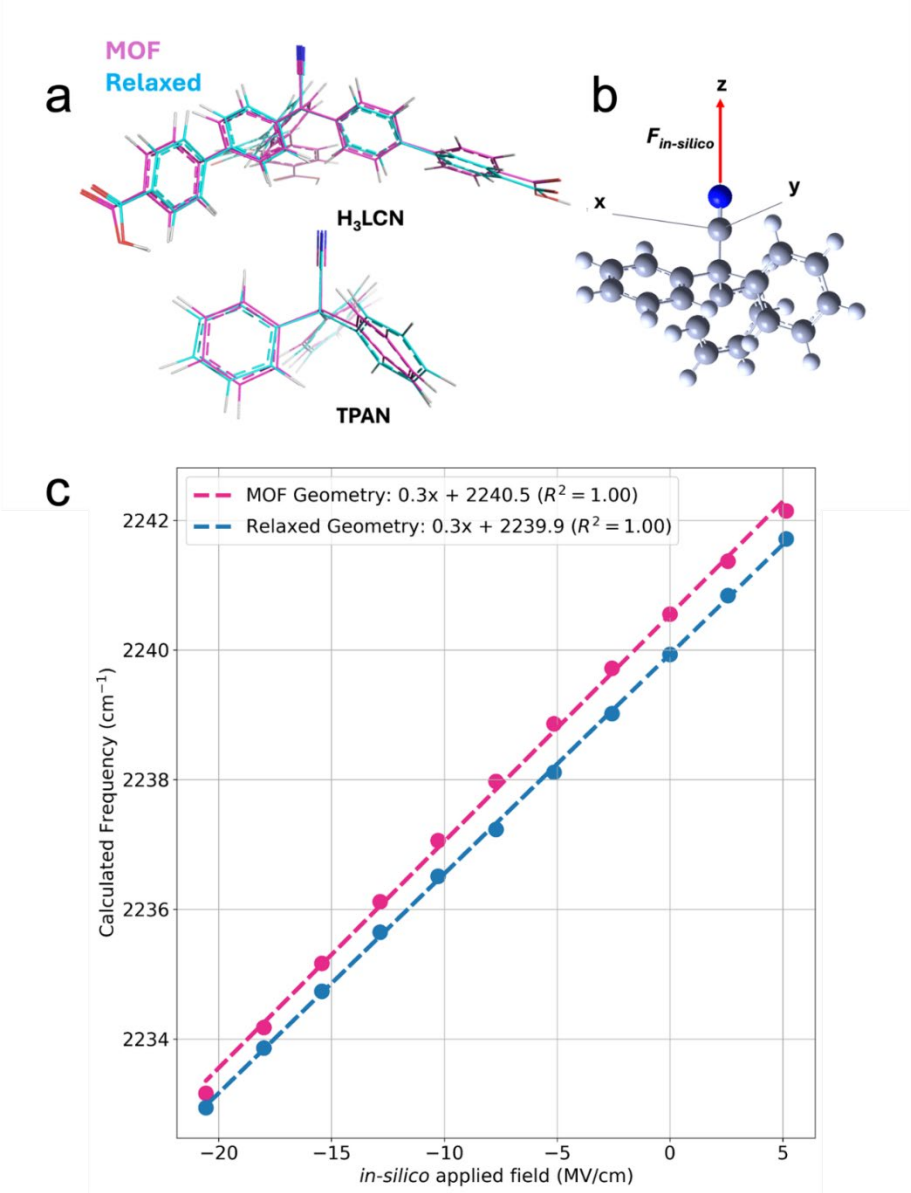

Supplementary Figure 29. DFT optimization and *in-silico* Stark of H_3LCN and TPAN. a. DFT-optimized structures of H_3LCN and the model compound TPAN in fixed and strained MOF like (Magenta) and free to relax (Cyan) geometries, performed at B3LYP 6-31+G(d) level. b. Schematic representing the application of an *in-silico* field along the nitrile. c. Field-frequency plot of the nitrile frequency after applying an *in-silico* field. DFT optimization (heavy atoms fixed) and frequency calculation were performed using B3LYP 6-31+G(d) level with the application of the in-silico field. (see Materials and Methods, Computational Details) Cartesian coordinates of the optimized structures can be found in Supplementary Information -> Cartesian coordinates of DFT calculation.zip -> H3LCN_Fixed.txt, H3LCN_Free.txt, TPAN_Fixed.txt, and TPAN_Free.txt.

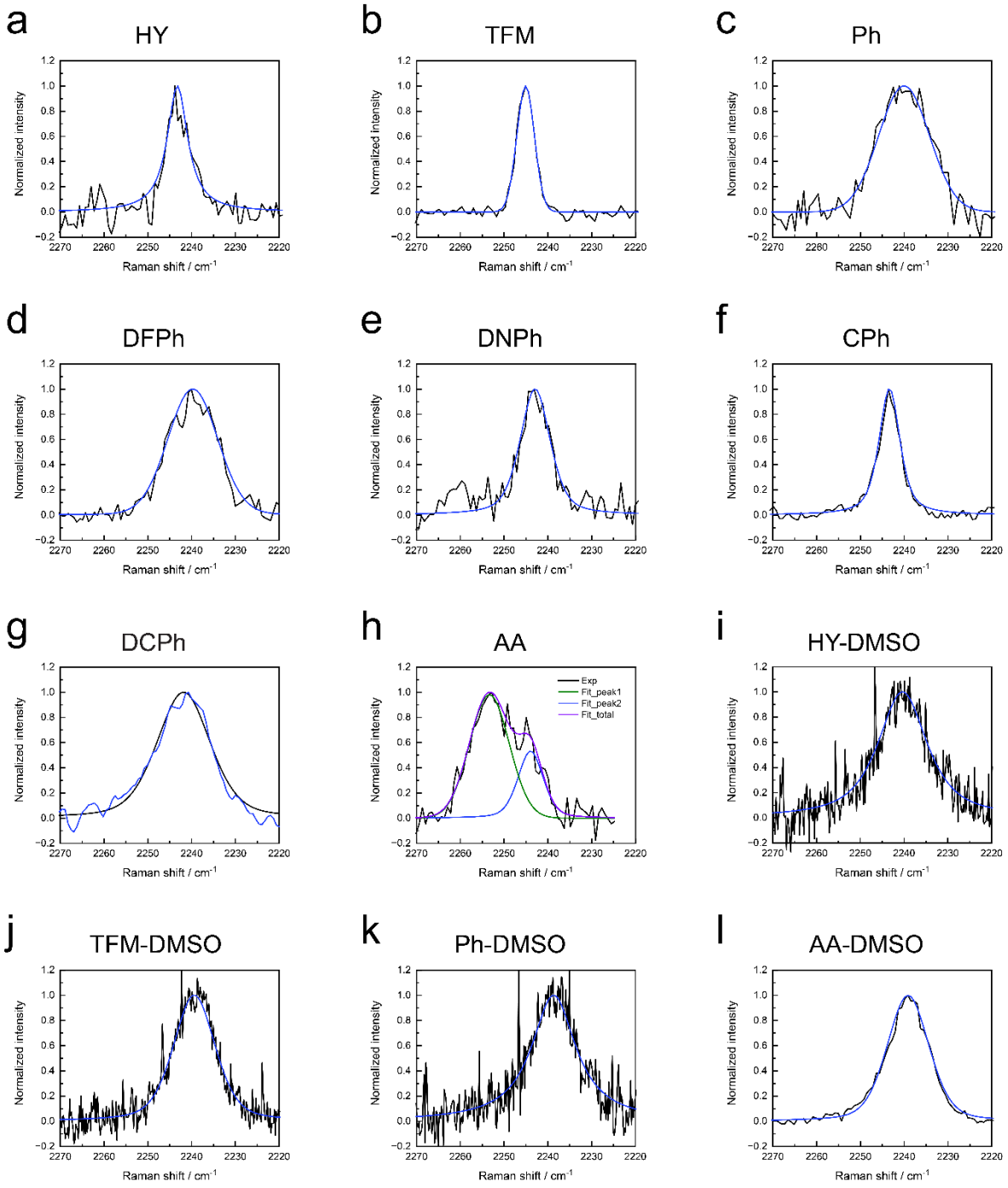

Supplementary Figure 30. Raw Raman spectra (average of triplicates) overlayed with the fitted Raman spectra for MOF samples. Only the fitted spectra are shown in the main text to remove clutter.

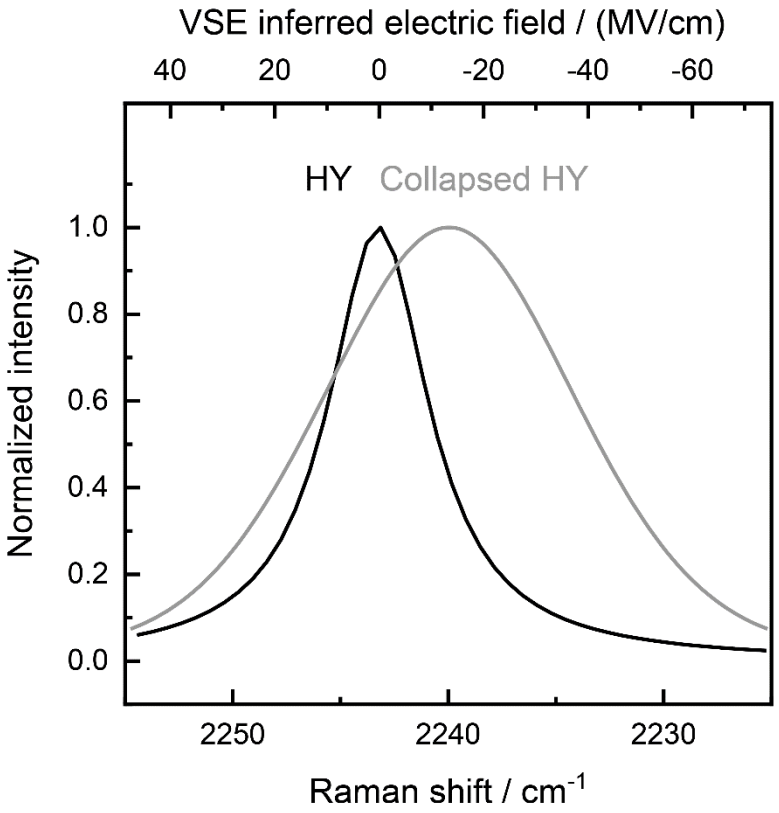

Supplementary Figure 31. Fitted Raman spectra of WT and a collapsed MOF sample. On collapse the nitrile peak of the sample red-shifts and broadens.

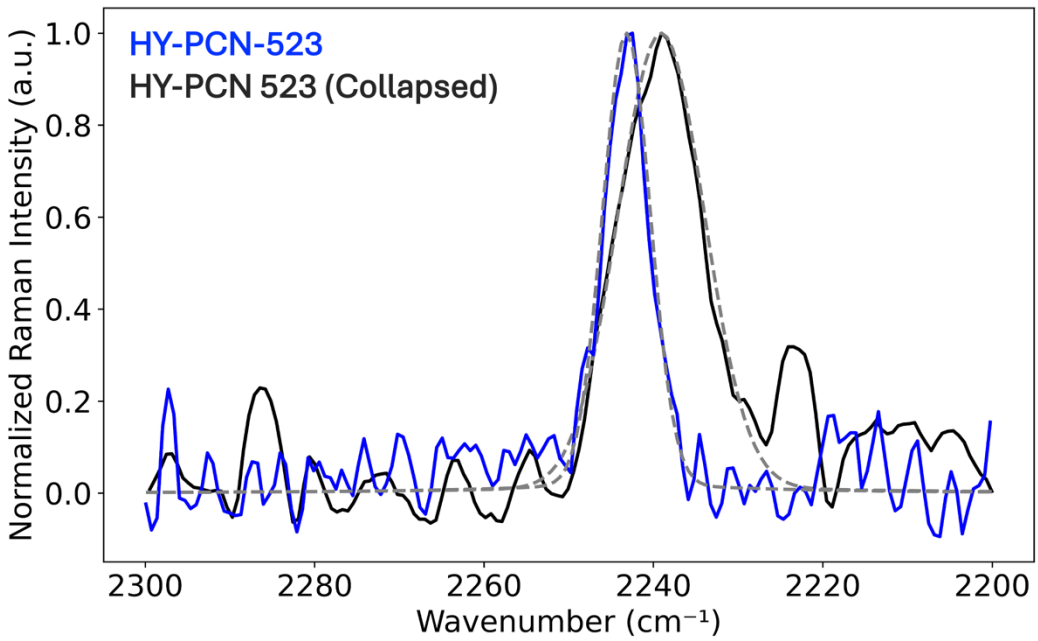

Supplementary Figure 32. Raman measurements on the HY and collapsed HY MOF scaffold PCN-523, where the Zr center of PCN-521 was substituted by Hf. PCN-521, which contains Zr, has pore dimensions of 20.5 Å × 20.5 Å × 37.4 Å. PCN-523, which contains Hf, has slightly altered pores with dimensions of 22.1 Å × 22.1 Å × 35.3 Å. Despite the changes in pore dimensions, the frequencies of the nitrile in the two MOFs are comparable (~2243.2 cm^{-1}) before and after collapse, consistent with what is reported in Supplementary Figure 31.

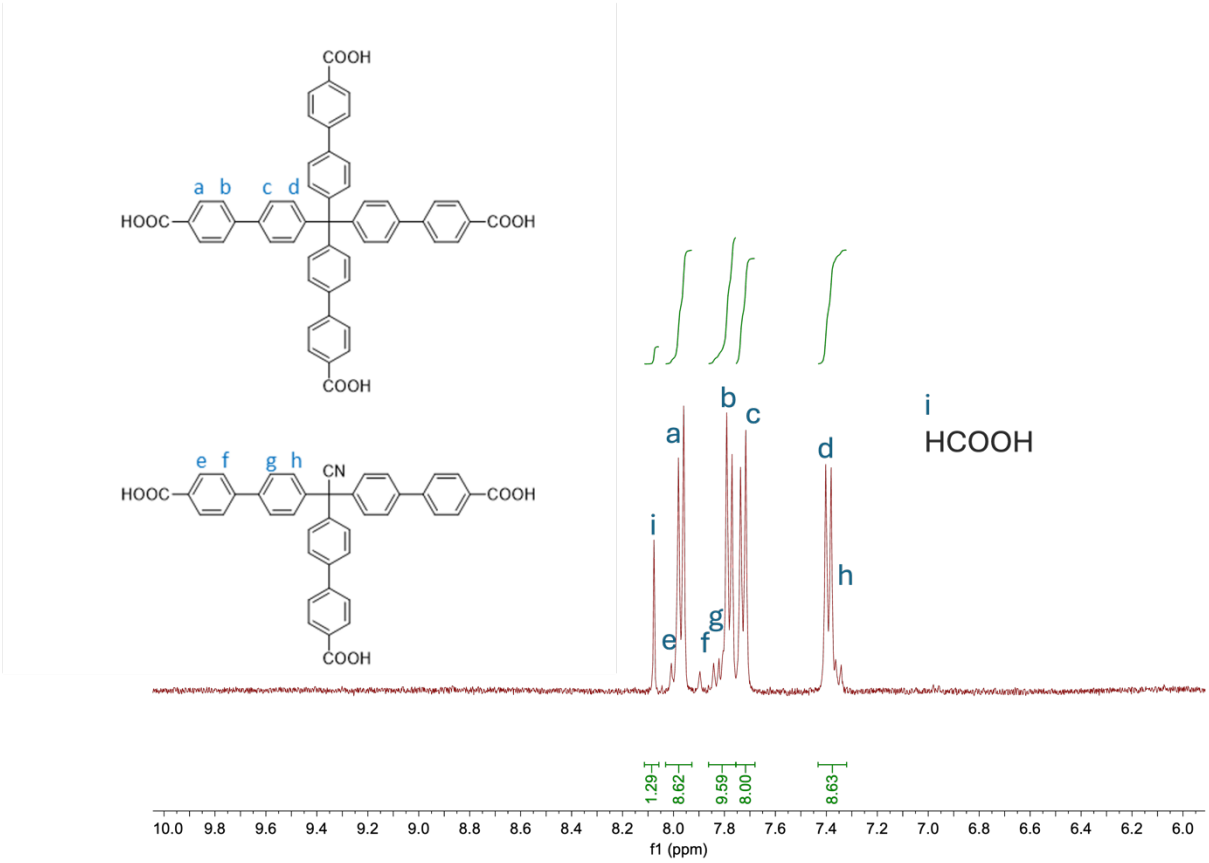

Supplementary Figure 33. ^{1}H Digestion NMR spectrum of the nitrile-substituted MOF scaffold PCN-523 (HY variant), where the Zr center of PCN-521 is substituted by Hf. Occupancy and substitution data is provided in Supplementary Table 1. (H_4L : H_3LCN : formic acid = 1 : 0.12 : 1.29)

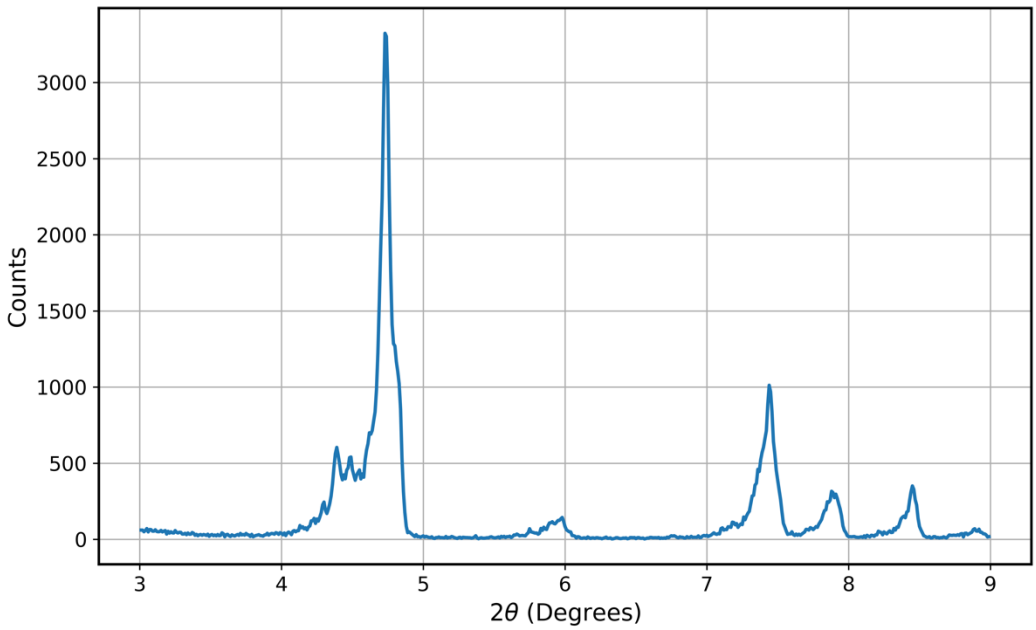

Supplementary Figure 34. PXRD measurements on the nitrile substituted MOF scaffold HY-PCN-523, where the Zr center of PCN-521 was substituted by Hf. The PXRD pattern for the defected PCN-523 crystals are near identical to the data presented for samples of PCN-521 in Supplementary Figs. 2 and 12.

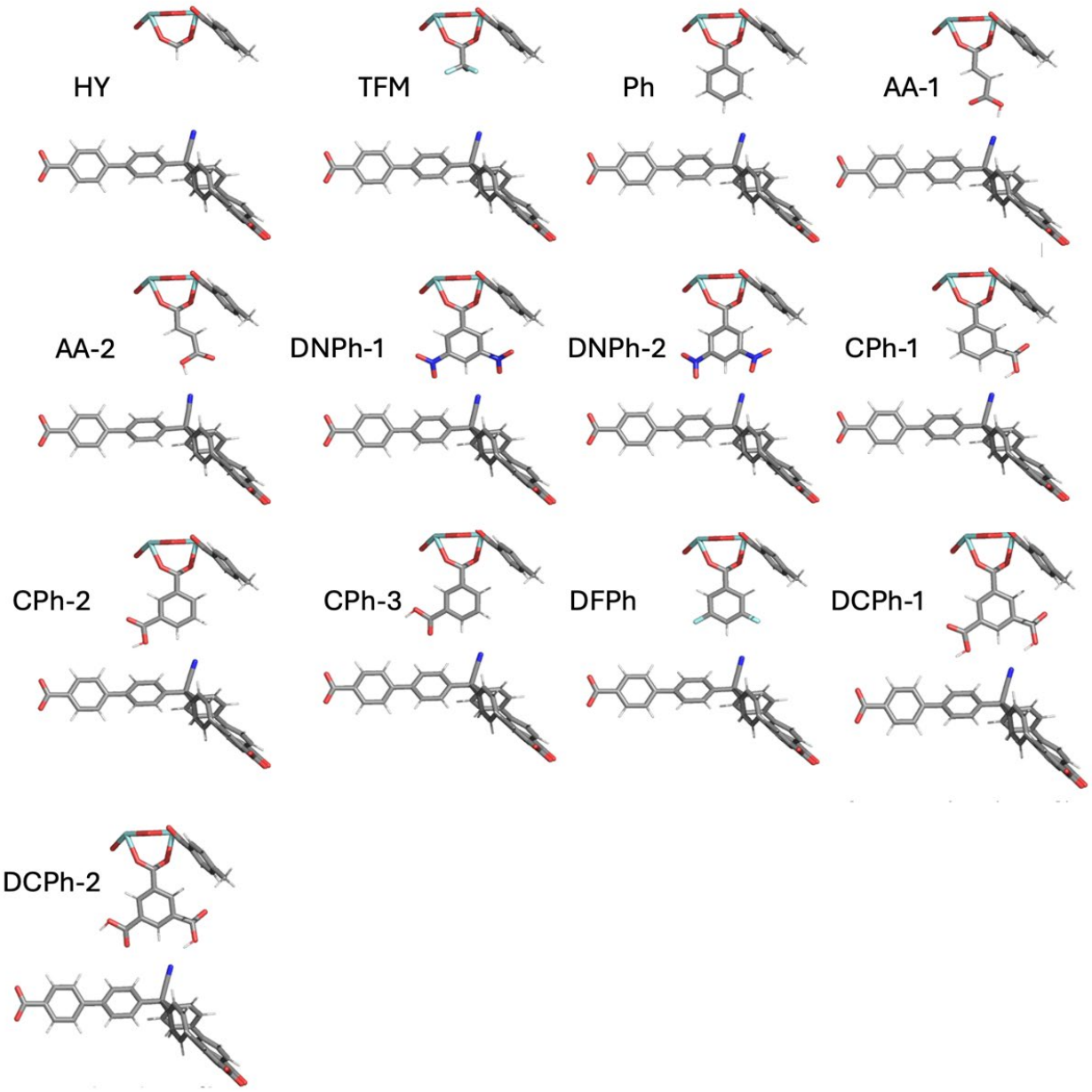

Supplementary Figure 35. Geometries for DFT optimized molecular models of variants (B3LYP with 6-31G(d) basis set for C, H, O and N atoms and LANL2DZ effective core potential for Zr). Cartesian coordinates of the optimized structures can be found in Supplementary Information -> Cartesian coordinates of DFT calculation.zip -> the corresponding text files.

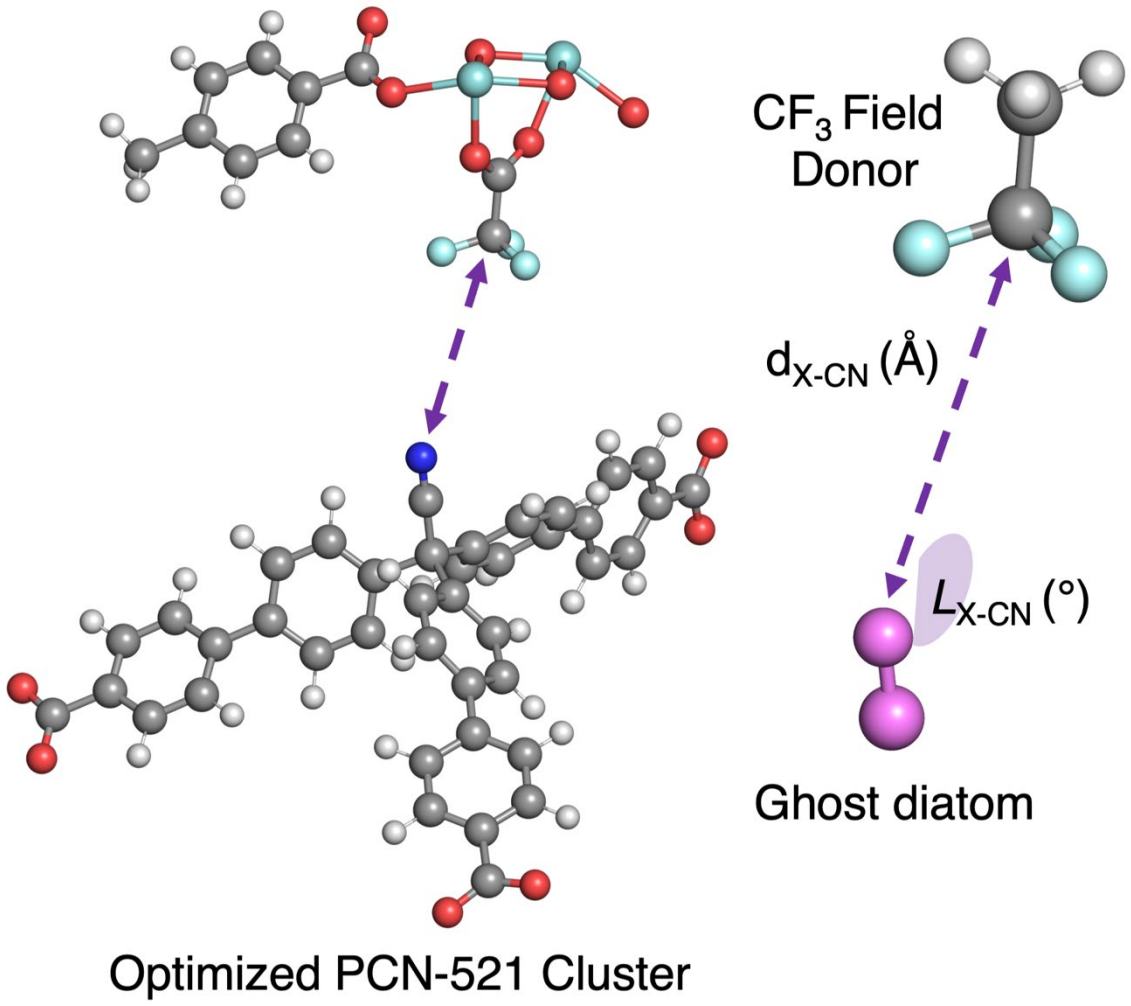

Supplementary Figure 36. Schematic representation of calculating fields using electrostatic potential maps. We calculate fields using electrostatic potential maps based on the methods outlined by the **QM2** method (Saggu et al.) [39] for estimating fields acting on the nitrile. Initially, we employ the geometries of the field donor and the nitrile probe from optimized cluster calculations presented in Supplementary Figure 35. Next, we cap the alpha carbon with a methyl group, conduct a geometry optimization of only the methyl group (other atoms frozen) at B3LYP/6-31+G(d), replace the H_3LCN nitrile with a ghost diatom and consequently perform a single-point calculation to generate the electrostatic potential map. This map allows us to isolate the fields acting on the nitrile ghost atom acceptor, represented as a drop in potential across the bond length.

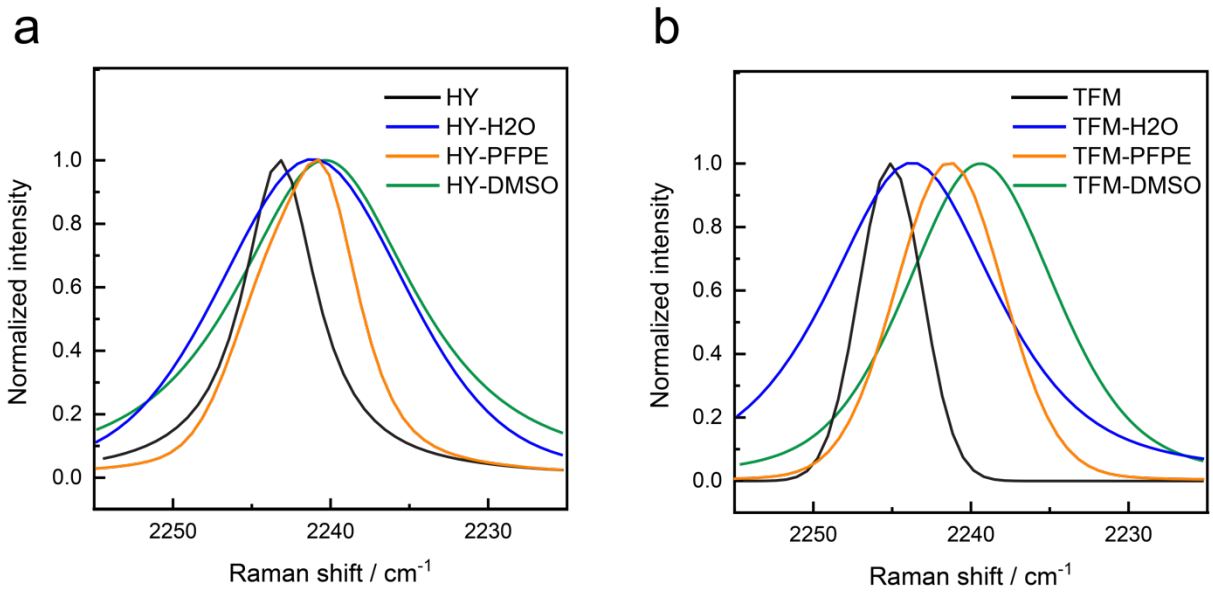

Supplementary Figure 37. Spectroscopic observation of solvation under nanoconfinement. (a) Fitted Raman spectra for evacuated HY, the H_2O solvated HY, the PFPE solvated HY, and the DMSO solvated HY. **(b)** Fitted Raman spectra for evacuated TFM, the H_2O solvated TFM, the PFPE solvated TFM, and the DMSO solvated TFM.

Supplementary Tables

Supplementary Table 1. Composition of PCN-521 (and HY-PCN 523) variants determined by digestion NMR. (Supplementary Figs. 3, 13-20, 33)

Variants	H_4L	H_3LCN	Field donor	Zr cluster	Open metal site[a]	Field donor occupancy[b]
HY	1	0.25	1.74	0.62	2.74	0.64
TFM	1	0.17	–	0.58	2.51	–
Ph	1	0.22	2.39	0.61	2.66	0.90
DFPh	1	0.35	2.34	0.68	3.06	0.76
DNPh	1	0.17	1.89	0.58	2.50	0.76
CPh	1	0.17	2.56	0.58	2.50	1.02
DCPh	1	0.35	2.55	0.67	3.04	0.84
AA	1	0.13	1.78	0.57	2.40	0.74
HY (PCN-523)	1	0.12	1.29	0.55	2.32	0.56

[a] Number of open metal sites = Number of Zr cluster × 4 + Number of H_3LCN.

[b] Field donor occupancy = Number of field donor / Number of Open metal site.

Supplementary Table 2. Solvent electric fields projected on the nitrile in TPAN based on fixed-charge MD simulations using the GAFF (AMBER) forcefield.

Solvent	Field Average (MV/cm)[a]	Field Standard Deviation (MV/cm)
Hexanes	0.1	0.7
Dibutylether	-5.5	4.6
Toluene	-8.5	6.0
THF	-10.5	6.4
Pyridine	-14.1	8.4
N,N'-dimethylformamide	-15.4	8.5
DMSO	-16.4	9.0
Water	-33.3	17.8

[a] Statistics are based on 20,000 total frames from 4 independent MD runs, each run with 5,000 frames (Supplementary Data). The reported average and standard deviation are derived from the 20,000 total frames.

Supplementary Table 3. Solvent electric fields projected on the nitrile in TPAN based on polarizable MD simulations using the AMOEBA forcefield.

Solvent	Field Average (MV/cm)[a]	Field Standard Deviation (MV/cm)
Hexanes	-17.1	10.8
Toluene	-20.6	8.7
THF	-20.7	10.1
Pyridine	-24.6	11.1
N,N'-dimethylformamide	-24.9	14.2
DMSO	-27.4	14.1
Water	-56.6	25.4

[a] Statistics are based on 2,100 total frames for 3 independent runs (hexane), 4,014 total frames from 4 independent runs (toluene), 3,014 total frames from 3 independent runs (THF), 2,995 total frames from 3 independent runs (pyridine), 3,968 total frames from 3 independent runs (DMF), 3,000 total frames from 3 independent runs (DMSO), and 3,000 total frames from 3 independent runs (water), respectively (Supplementary Data). The fields calculated from each independent run were fitted to a Gaussian function to obtain the mean and the standard deviation, which are then averaged between the runs and reported here.

Supplementary Table 4. FTIR data analysis of TPAN solutions. (Supplementary Figure 23)

Solvent	Position (cm^{-1})	FWHM (cm^{-1})	Lorentzian (%)
Hexanes	2239.7	6.1	68
Dibutylether	2239.0	6.2	64
Toluene	2238.3	6.2	37
THF	2237.9	5.9	55
Pyridine	2237.4	6.9	41
N,N'-dimethylformamide	2237.1	7.1	39
DMSO	2236.8	7.3	16

Supplementary Table 5. Solvent electric fields projected on the nitrile in H_3LCN based on fixed charge MD simulations using the GAFF (AMBER) forcefield. The statistics are based on 20,000 total frames from 4 independent MD runs, each run with 5,000 frames.

Solvent	Field Average (MV/cm)	Field Standard Deviation (MV/cm)
THF	-12.5	6.6
pyridine	-16.7	8.7
N,N'-dimethylformamide	-17.3	8.7
DMSO	-19.1	9.1
water	-33.2	17.8

Supplementary Table 6. FTIR data analysis of H_3LCN solutions. (Supplementary Figure 23)

Solvent	Position (cm^{-1})	FWHM (cm^{-1})	Lorentzian (%)
THF	2238.6	6.2	22
pyridine	2238.0	6.8	7
N,N'-dimethylformamide	2237.8	7.4	11
DMSO	2237.6	8.0	0

Supplementary Table 7. Vibrational frequencies of the nitrile in PCN-521 variants measured by Raman spectroscopy. (Supplementary Figure 30)

Variants	Position (cm^{-1})	FWHM (cm^{-1})	Lorentzian (%)
HY	2243.2	5.6	100
TFM	2245.1	4.8	0
Ph	2240.0	13.7	0
DFPh	2239.7	13.4	7
DNPh	2242.9	8.1	47
CPh	2243.4	5.7	62
DCPh	2241.9	14.4	36
AA	2244.0	6.8	32
	2253.4	10.7	0
HY-DMSO	2240.3	13.5	81
TFM-DMSO	2239.4	11.3	40
Ph-DMSO	2238.7	12.3	100
AA-DMSO	2239.1	11.2	30

Supplementary Table 8. Summary of cluster DFT calculations for the MOF defect site. Energies, entropies, frequencies of the lowest energy calculated structures from DFT (B3LYP with 6-31G(d) basis set for C, H, O and N atoms and LANL2DZ effective core potential for Zr) are presented. (Supplementary Figure 35)

Structure	E_{elec} (hartree)[a]	ZPE (hartree)	H (hartree)	T·S (hartree)	T·qh-S (hartree)[b]	G (hartree)	qh-G (hartree)[b]	Lowest freq. (cm^{-1})	# of imag freq.	Boltzmann weight	CN str. freq. (cm^{-1})[c]
HY	–3050.473877	0.511148	–3049.926806	0.107351	0.099660	–3050.034156	–3050.026466	20.6	0	1.00	2244
TFM	–3387.499878	0.514461	–3386.945175	0.118437	0.108418	–3387.063613	–3387.053594	8.6	0	1.00	2245
Ph	–3281.542299	0.588370	–3280.912725	0.118738	0.109253	–3281.031462	–3281.021978	20.2	0	1.00	2243
AA_1	–3316.460658	0.557386	–3315.862081	0.118697	0.109530	–3315.980778	–3315.971612	21.2	0	0.61	2261
AA_2	–3316.459779	0.557091	–3315.861403	0.119038	0.109775	–3315.980441	–3315.971177	19.5	0	0.39	2254
DNPh_1	–3690.526932	0.592339	–3689.887925	0.132049	0.120389	–3690.019974	–3690.008314	13.0	0	0.91	2243
DNPh_2	–3690.524834	0.592589	–3689.885567	0.132571	0.120596	–3690.018138	–3690.006163	12.2	0	0.09	2247
CPh_1	–3470.114772	0.603060	–3469.467769	0.124993	0.114748	–3469.592762	–3469.582517	12.0	0	0.90	2257
CPh_2	–3470.111029	0.602359	–3469.464418	0.126314	0.115442	–3469.590732	–3469.579860	14.0	0	0.03	2245
CPh_3	–3470.111318	0.602532	–3469.464631	0.125380	0.115000	–3469.590011	–3469.579631	17.9	0	0.04	2243
DFPh	–3480.004165	0.572619	–3479.388494	0.123411	0.113053	-3479.511904	-3479.501547	17.9	0	1.00	2248
DCPh_1	–3658.683830	0.616914	–3658.019930	0.131918	0.120678	–3658.151848	–3658.140609	11.1	0	0.63	2359
DCPh_2	–3658.683642	0.617005	–3658.019720	0.131288	0.120375	–3658.151008	–3658.140095	13.6	0	0.37	2357

[a] 1 hartree = 627.509 kcal mol^{-1}. Thermal corrections at 298.15 K.

[b] qh: quasi-harmonic approximation.

[c] Scaled frequencies (factor = 0.96; NIST Database).

Supplementary Table 9. Distance and angle data from DFT optimized structures presented in Supplementary Figure 35. The pictorial representation of the distances and angles are presented in Supplementary Figure 36.

Variant*	**$d_{C(Zr)-C(H3LCN)}$, Å**	**Field donor heavy atom CN-(X)**	**Angle $_{CN-X}$,°**	**d_{CN-X}, Å**	**d_{CN-H}, Å**	**Predicted frequency shift due to H-bond $\Delta\bar{\upsilon}_{HB\text{-}Model}$ (Kirsh and Kozuch)[13] cm^{-1}**
HY	9.77	CN-**C**	155.61	7.31	6.23	
TFM	9.78	CN-**C**	163.56	5.81	-	
Ph	9.80	CN-**C**	125.06	3.34	2.45	
DNPh_1	9.78	CN-**C**	140.31	3.36	2.57	
DNPh_2	9.80	CN-**C**	143.37	3.24	2.34	
DFPh	9.85	CN-**C**	142.95	3.26	2.29	
AA_1	9.77	CN-**O**	172.94	2.83	1.84	32.8
AA_2	9.77	CN-**O**	161.30	2.87	1.88	30.2
CPh_1	9.88	CN-**C**	147.83	2.80	2.38	-
		CN-**O**	144.46	3.32	1.85	31.4
CPh_2	9.81	CN-**C**	137.65	3.29	2.34	-
CPh_3	9.77	CN-**C**	134.99	3.35	2.48	-
DCPh_1	9.86	CN-**O**	150.08	2.80	1.86	31.8
		CN-**C**	141.99	3.29	2.32	
DCPh_2	9.84	CN-**O**	148.52	2.77	1.83	32.9
		CN-**C**	140.63	3.35	2.49	

* Variants of the format “Variant_n” (e.g. DNPh_2) are indicative of different major conformers as listed in Supplementary Table 8 and presented in Supplementary Figure 35.

Supplementary Table 10. Estimation of fields using DFT based ESP calculations.

Variant	φ_C (a.u)	φ_N (a.u)	d_{C-N}, Å	EF (MV/cm)
HY	-0.00069	-0.000795	1.162	0.5
TFM	-0.003867	-0.005096	1.162	5.5
Ph	0.002105	0.004348	1.162	-10.0
DNPh_1	-0.002681	0.002667	1.162	-23.7
DNPh_2	-0.003498	0.003046	1.161	-29.0
DFPh	0.000511	0.003344	1.161	-12.6
AA_1	0.007075	0.029493	1.159	-99.5
AA_2	0.009998	-0.010573	1.160	-91.2
CPh_1	0.020336	0.046267	1.159	-115.0
CPh_2	0.002404	0.006614	1.161	-18.6
CPh_3	-0.00311	0.001931	1.162	-22.3
DCPh_1	0.020005	0.047027	1.159	-119.9
DCPh_2	0.013493	0.042543	1.159	-128.9

Supplementary Table 11. Frequency shift due to H-bond.

	F_{ESP}	$\bar{\upsilon}_{Obs}$	$\bar{\upsilon}_{Exp}$	$\Delta\bar{\upsilon}_{HB}$	$\Delta\bar{\upsilon}_{HB\text{-model}}$
Variants	Calculated electric fields using ESP	Observed Raman shift	Expected frequency based on F_{ESP} [a]	Frequency shift due to H-bond [b]	Predicted frequency shift due to H-bond (Kirsh and Kozuch)[13]
	MV/cm	cm^{-1}	cm^{-1}	cm^{-1}	cm^{-1}
HY	0.5	2243.2	2243.3	–	–
TFM	5.5	2245.1	2244.5	–	–
Ph	-10.0	2240.0	2240.8	–	–
DFPh	-12.6	2239.7	2240.1	–	–
DNPh	-24.2 [c]	2242.9	2237.3	5.6	–
CPh	-105.0 [c]	2243.4	2217.8	25.6	28.2 [c]
DCPh	-123.2 [c]	2241.9	2213.3	28.6	32.2 [c]
AA	-96.2 [c]	2253.4	2219.9	33.5	31.8 [c]

[a] Calculated based on the linear vibrational Stark effect, $\bar{\upsilon}_{exp}$= 0.24 F_{ESP} + 2243.2.

[b] $\Delta\bar{\upsilon}_{HB} = \bar{\upsilon}_{Obs} - \bar{\upsilon}_{Exp}$.

[c] Conformationally averaged with Boltzmann weights in Supplementary Table 8.

Supplementary Table 12. Frequency shift due to solvation of the MOF cavity.

	$\bar{\upsilon}_{Vac}$	$\bar{\upsilon}_{Sol}$	$\Delta\bar{\upsilon}_{Sol}$	$\Delta\bar{\upsilon}_{\mathrm{HB}}$	ΔF_{sol}	$\Delta F_{sol} + F_{\mathrm{ESP}}$
Variants	Observed Raman shift of evacuated MOF	Observed Raman shift of DMSO solvated MOF	Frequency shift due to DMSO solvation		Electric field change due to DMSO solvation[a]	Nitrile experienced total electric field
	cm^{-1}	cm^{-1}	cm^{-1}	cm^{-1}	MV/cm	MV/cm
HY	2243.2	2240.3	-2.9	–	-12.0	-11.5
TFM	2245.1	2239.4	-5.7	–	-23.5	-18.0
Ph	2240.0	2238.7	-1.3	–	-5.4	-15.4
AA	2253.4	2239.1	-14.3	33.5	79.2	-17.0

[a] Calculated based on the linear vibrational Stark effect, $\Delta F_{sol} = (\Delta\nu_{\mathrm{sol}} + \Delta\bar{\upsilon}_{\mathrm{HB}}) / 0.24$.

References

1. Bunck, D. N. & Dichtel, W. R. Internal functionalization of three-dimensional covalent organic frameworks. *Angew. Chemie - Int. Ed.* **51**, 1885–1889 (2012).

2. Nösel, P. *et al.* Oxidative gold catalysis meets photochemistry - Synthesis of benzo[a]fluorenones from diynes. *Adv. Synth. Catal.* **356**, 3755–3760 (2014).

3. Nikitin, K., Lestini, E., Lazzari, M., Altobello, S. & Fitzmaurice, D. A tripodal [2]rotaxane on the surface of gold. *Langmuir* **23**, 12147–12153 (2007).

4. Zhang, M. *et al.* Symmetry-guided synthesis of highly porous metal-organic frameworks with fluorite topology. *Angew. Chemie - Int. Ed.* **53**, 815–818 (2014).

5. Boxer, S. G. Stark realities. *J. Phys. Chem. B* **113**, 2972–2983 (2009).

6. Fried, S. D. & Boxer, S. G. Measuring electric fields and noncovalent interactions using the vibrational stark effect. *Acc. Chem. Res.* **48**, 998–1006 (2015).

7. Hush, N. S. & Reimers, J. R. Vibrational Stark spectroscopy. 1. Basic theory and application to the CO stretch. *J. Phys. Chem.* **99**, 15798–15805 (1995).

8. Andrews, S. S. & Boxer, S. G. Vibrational Stark effects of nitriles II. Physical origins of Stark effects from experiment and perturbation models. *J. Phys. Chem. A* **106**, 469–477 (2002).

9. Weaver, J. B., Kozuch, J., Kirsh, J. M. & Boxer, S. G. Nitrile Infrared Intensities Characterize Electric Fields and Hydrogen Bonding in Protic, Aprotic, and Protein Environments. *J. Am. Chem. Soc.* **144**, 7562–7567 (2022).

10. Fried, S. D., Wang, L. P., Boxer, S. G., Ren, P. & Pande, V. S. Calculations of the electric fields in liquid solutions. *J. Phys. Chem. B* **117**, 16236–16248 (2013).

11. Kirsh, J. M., Weaver, J. B., Boxer, S. G. & Kozuch, J. Critical Evaluation of Polarizable and Nonpolarizable Force Fields for Proteins Using Experimentally Derived Nitrile Electric Fields. *J. Am. Chem. Soc.* **146**, 6983–6991 (2024).

12. Oh, K. I. *et al.* Nitrile and thiocyanate IR probes: Molecular dynamics simulation studies. *J. Chem. Phys.* **128**, 154504 (2008).

13. Kirsh, J. M., & Kozuch, J. Hydrogen Bond Blueshifts in Nitrile Vibrational Spectra Are Dictated by Hydrogen Bond Geometry and Dynamics. *JACS Au*, **4**, 4844–4855 (2024).

14. Zheng, C. *et al.* A two-directional vibrational probe reveals different electric field orientations in solution and an enzyme active site. *Nat. Chem.* **14**, 891–897 (2022).

15. Fried, S. D., Bagchi, S. & Boxer, S. G. Extreme electric fields power catalysis in the active site of ketosteroid isomerase. *Science (80-.).* **346**, 1510–1514 (2014).

16. Frisch, M. J. *et al.* G16_C01. Gaussian 16, Revision C.01, Gaussian, Inc., Wallin (2016).

17. Case, D. A. *et al.* AmberTools. *J. Chem. Inf. Model.* **63**, 6183–6191 (2023).

18. Wang, J., Wolf, R. M., Caldwell, J. W., Kollman, P. A. & Case, D. A. Development and testing of a general Amber force field. *J. Comput. Chem.* **25**, 1157–1174 (2004).

19. Caleman, C. *et al.* Force Field Benchmark of Organic Liquids: Density, Enthalpy of

Vaporization, Heat Capacities, Surface Tension, Isothermal Compressibility, Volumetric Expansion Coefficient, and Dielectric Constant. *J. Chem. Theory Comput.* **8**, 61–74 (2012).

20. Jorgensen, W. L., Chandrasekhar, J., Madura, J. D., Impey, R. W. & Klein, M. L. Comparison of simple potential functions for simulating liquid water. *J. Chem. Phys.* **79**, 926–935 (1983).

21. Hess, B., Kutzner, C., van der Spoel, D. & Lindahl, E. GROMACS 4: Algorithms for Highly Efficient, Load-Balanced, and Scalable Molecular Simulation. *J. Chem. Theory Comput.* **4**, 435–447 (2008).

22. Essmann, U. *et al.* A smooth particle mesh Ewald method. *J. Chem. Phys.* **103**, 8577–8593 (1995).

23. Berendsen, H. J. C., Postma, J. P. M., Van Gunsteren, W. F., Dinola, A. & Haak, J. R. Molecular dynamics with coupling to an external bath. *J. Chem. Phys.* **81**, 3684–3690 (1984).

24. Parrinello, M. & Rahman, A. Polymorphic transitions in single crystals: A new molecular dynamics method. *J. Appl. Phys.* **52**, 7182–7190 (1981).

25. Hess, B., Bekker, H., Berendsen, H. J. C. & Fraaije, J. G. E. M. LINCS: A linear constraint solver for molecular simulations. *J. Comput. Chem.* **18**, 1463–1472 (1997).

26. Rackers, J. A. *et al.* Tinker 8: Software Tools for Molecular Design. *J. Chem. Theory Comput.* **14**, 5273–5289 (2018).

27. Ren, P., Wu, C. & Ponder, J. W. Polarizable atomic multipole-based molecular

mechanics for organic molecules. *J. Chem. Theory Comput.* **7**, 3143–3161 (2011).

28. Wang, Z. Polarizable Force Field Development, and Applications to Conformational Sampling and Free Energy Calculations. (2018).

29. Walker, B., Liu, C., Wait, E. & Ren, P. Automation of AMOEBA polarizable force field for small molecules: Poltype 2. *J. Comput. Chem.* **43**, 1530–1542 (2022).

30. Wu, J. C., Chattree, G. & Ren, P. Automation of AMOEBA polarizable force field parameterization for small molecules. *Theor. Chem. Acc.* **131**, 1–11 (2012).

31. Martínez, L., Andrade, R., Birgin, E. G. & Martínez, J. M. PACKMOL: A package for building initial configurations for molecular dynamics simulations. *J. Comput. Chem.* **30**, 2157–2164 (2009).

32. Leimkuhler, B. J., Reich, S. & Skeel, R. D. Integration Methods for Molecular Dynamics. in (eds. Mesirov, J. P., Schulten, K. & Sumners, D. W.) 161–185 (Springer New York, 1996). doi:10.1007/978-1-4612-4066-2_10.

33. Dalosto, S. D., Vanderkooi, J. M. & Sharp, K. A. Vibrational Stark Effects on Carbonyl, Nitrile, and Nitrosyl Compounds Including Heme Ligands, CO, CN, and NO, Studied with Density Functional Theory. *J. Phys. Chem. B* **108**, 6450–6457 (2004).

34. Stephens, P. J., Devlin, F. J., Chabalowski, C. F. & Frisch, M. J. Ab Initio Calculation of Vibrational Absorption and Circular Dichroism Spectra Using Density Functional Force Fields. *J. Phys. Chem.* **98**, 11623–11627 (1994).

35. Hay, P. J. & Wadt, W. R. Ab initio effective core potentials for molecular calculations.

Potentials for K to Au including the outermost core orbitals. *J. Chem. Phys.* **82**, 299–310 (1985).

36. Luchini, G., Alegre-Requena, J. V, Funes-Ardoiz, I. & Paton, R. S. GoodVibes: automated thermochemistry for heterogeneous computational chemistry data [version 1; peer review: 2 approved with reservations]. *F1000Research* **9**, (2020).

37. Grimme, S. Supramolecular Binding Thermodynamics by Dispersion-Corrected Density Functional Theory. *Chem. – A Eur. J.* **18**, 9955–9964 (2012).

38. Wang, L., Fried, S. D. & Markland, T. E. Proton Network Flexibility Enables Robustness and Large Electric Fields in the Ketosteroid Isomerase Active Site. *J. Phys. Chem. B* **121**, 9807–9815 (2017).

39. Saggu, M., Levinson, N. M. & Boxer, S. G. Experimental quantification of electrostatics in X-H···φ hydrogen bonds. *J. Am. Chem. Soc.* **134**, 18986–18997 (2012).

40. Fried, S. D. E., Mukherjee, S., Mao, Y., & Boxer, S. G. Environment- and Conformation-Induced Frequency Shifts of C–D Vibrational Stark Probes in NAD(P)H Cofactors. *J. Phys. Chem. Lett.*, **15**, 10826–10834 (2024).